3D-Printed Drug-loaded Intravesical Inserts – Development, Manufacturing and Biopharmaceutical Performance

Inaugural-Dissertation

zur Erlangung des Doktorgrades

der Mathematisch-Naturwissenschaftlichen Fakultät

der Heinrich-Heine-Universität Düsseldorf

vorgelegt von

Jhinuk Rahman-Yildir (geb. Rahman)

aus Köln

Düsseldorf, September 2022

aus dem Institut für Pharmazeutische Technologie und Biopharmazie
der Heinrich-Heine-Universität Düsseldorf

Gedruckt mit der Genehmigung der
Mathematisch-Naturwissenschaftlichen Fakultät der
Heinrich-Heine-Universität Düsseldorf

Berichterstatter:

1. Prof. Dr. Jörg Breitkreutz
2. Prof. Dr. Anne Seidlitz

Tag der mündlichen Prüfung: 09.11.2022

To my parents

Table of contents

List of abbreviations

3DP	Three-dimensional printing
API	Active pharmaceutical ingredient
BCS	Biopharmaceutics classification system
CAD	Computer-aided design
CCD	Central composite design
CYP	Cytochrome P450
DBS	Dibutyl sebacate
DDD	Drug delivery device
DoE	Design of experiments
DSC	Differential scanning calorimetry
EA	Ethyl acetate
EVA	Ethylene vinyl acetate copolymer
f_2	Similarity factor
FDA	Food and drug administration
FDM	Fused deposition modeling
FT-IR	Fourier transformed infrared spectroscopy
HCT	Hydrochlorothiazide
HPLC	High performance liquid chromatography
HPMC	Hydroxypropyl methylcellulose/ Hypromellose
IPC	In process control
KP	Korsmeyer-Peppas
LC-HCl	Lidocaine hydrochloride monohydrate
LiRIS	Lidocaine-releasing intravesical system
LVE	Linear viscoelastic
MDT	Mean dissolution time
ME	Micro-extrusion
OAB	Overactive bladder
PAM	Pressure-assisted microsyringe
PCL	Poly(ε-caprolactone)
PCL-PEG	Poly(ε-caprolactone)-polyethylene glycol copolymer
PDLLA	Poly(D,L-lactide)
PEG	Polyethylene glycol/ Macrogol

Ph. Eur.	European Pharmacopoeia
PLA	Polylactic acid
PLGA	Poly(D,L-lactide-co-glycolide)
PLCL	Poly(L-lactide-co-ε-caprolactone)
P_r	Printability index
P_{score}	Printability score
RSD	Relative standard deviation
SA/V	Surface area to volume
S/ Sd	Standard deviation (absolute)
SEM	Scanning electron microscopy
SLA	Stereolithography
STL	Stereolithography file
TA	Texture analyser
T_g	Glass transition temperature
THF	Tetrahydrofuran
TrCl	Trospium chloride
USP	United States Pharmacopoeia
UV	Ultraviolet
VA	Vinyl acetate
XRPD	X-ray powder diffraction
YM	Young's modulus
µCT	X-ray micro-computed tomography

Publications

Parts of this thesis have already been published in peer-reviewed journals or presented at international conferences. The contents were partially linguistically adapted, shortened, or extended to include a more comprehensive overview.

Original publications

1. Jhinuk Rahman, Julian Quodbach
   Versatility on demand – The case for semi-solid micro-extrusion in pharmaceutics
   Advanced Drug Delivery Reviews, Volume 172, 2021, pages 104-126
   DOI: 10.1016/j.addr.2021.02.013

   Evaluation of authorship

Author	Idea [%]	Study design [%]	Experimental [%]	Evaluation [%]	Manuscript [%]
J. Rahman	50	50	-	50	50
J. Quodbach	50	50	-	50	50

   JR and JQ were equally responsible for the idea, study design, literature curation and evaluation as well as writing and revising of the manuscript.

2. Jhinuk Rahman-Yildir, Björn Fischer, Jörg Breitkreutz
   Development of sustained-release drug-loaded intravesical inserts via semi-solid micro-extrusion 3D-printing for bladder targeting
   International Journal of Pharmaceutics, Volume 622, 2022, 121849
   DOI: 10.1016/j.ijpharm.2022.121849

   Evaluation of authorship

Author	Idea [%]	Study design [%]	Experimental [%]	Evaluation [%]	Manuscript [%]
J. Rahman-Yildir	90	80	80	90	80
B. Fischer	-	10	20	10	10
J. Breitkreutz	10	10	-	-	10

   JR developed the idea in cooperation with JB and was responsible for investigation, formal analysis, evaluation and writing of the manuscript. BF performed the confocal Raman-measurements as well as corresponding data interpretation and image analysis of the Raman images and was involved in writing and editing of the respective sections in the manuscript. JB supervised the work and revised and edited the manuscript.

3. Jhinuk Rahman-Yildir, Raphael Wiedey, Jörg Breitkreutz
   Comparative dissolution studies of 3D-printed inserts in a novel biopharmaceutical bladder model
   International Journal of Pharmaceutics, Volume 624, 2022, 121984
   DOI: 10.1016/j.ijpharm.2022.121984

   Evaluation of authorship

Author	Idea [%]	Study design [%]	Experimental [%]	Evaluation [%]	Manuscript [%]
J. Rahman-Yildir	70	90	90	100	80
R. Wiedey	20	-	10	-	10
J. Breitkreutz	10	10	-	-	10

   JR developed the idea in cooperation with RW and JB, and was responsible for most of the experimental work and writing of the manuscript. RW contributed to the development of the study design and was responsible for engineering and programming of the electronics and reviewed and edited the manuscript. JB supervised the work and revised and edited the manuscript.

4. Ilias El Aita, Jhinuk Rahman, Jörg Breitkreutz, Julian Quodbach *(not used in this thesis)*
   3D-Printing with precise layer-wise dose adjustments for paediatric use via pressure-assisted microsyringe printing
   European Journal of Pharmaceutics and Biopharmaceutics, Volume 157, 2020, pages 59-65
   DOI: 10.1016/j.ejpb.2020.09.012

   Evaluation of authorship

Author	Idea [%]	Study design [%]	Experimental [%]	Evaluation [%]	Manuscript [%]
I. El Aita	70	70	80	70	60
J. Rahman	10	10	20	20	20
J. Breitkreutz	10	10	-	-	10
J. Quodbach	10	10	-	10	10

   IEA was responsible for the idea and study design as well as for the execution of the experimental work. Data evaluation and writing of the manuscript was performed by IEA. JR was involved in the execution of the experimental work, data evaluation and writing of the manuscript. JB and JQ were responsible for the idea and the study design as well as for the revision of the manuscript.

Contributions to conferences

1. Ilias El Aita, Jhinuk Rahman, Jörg Breitkreutz, Julian Quodbach
   Printing Paediatric Dosage Forms Precisely: Layer by Layer (oral presentation Ilias El Aita)
   10th European Paediatric Formulation Initiative, London, September 2018

2. Jhinuk Rahman, Jörg Breitkreutz
   Development of Novel Intravesical Inserts via 3D-Printing (poster presentation)
   3rd European Conference on Pharmaceutics, Bologna, Italy, March 25-26, 2019

3. Jhinuk Rahman, Jörg Breitkreutz
   Development of sustained release intravesical inserts via 3D-printing (oral presentation)
   13th PSSRC Annual Meeting, Düsseldorf, Germany, September 12, 2019

4. Jhinuk Rahman, Raphael Wiedey, Jörg Breitkreutz
   Dissolution Studies with 3D-printed Intravesical Inserts in Novel Biopharmaceutical Bladder Model (poster presentation)
   12th PBP World Meeting, online conference, May 11-14, 2021

1 Introduction

1.1 The urinary bladder as target for pharmaceutical treatment

The main function of the human urinary bladder is to store urine produced by the kidneys and release it under voluntary control. It is a muscular hollow organ that is located extraperitoneally inside the pelvic cavity and varies in size depending on gender, age and its filing level. The two ureters descending from the kidneys thereby convey urine at a rate of approximately 40-60 mL per hour into the bladder (Cima et al., 2014; Vaupel et al., 2015). The accumulated urine is voided again via the urethra during micturition. The urethra is a 5 (female) to 20 (male) cm long tube with a diameter of 6-8 mm, which connects the bladder neck to the exterior (Lippert et al., 2010; Mahadevan, 2019). At its upper end the sympathetically innervated internal sphincter muscle closes the entrance to the bladder. Distally, the external sphincter closes off the urethra, which is innervated by motor axons. When filling up, the bladder can expand to more than 15 times is original size assuming an ovoid shape (Korossis et al., 2006; Mahadevan, 2019). On average, it has a capacity of up to 600-1000 mL although the urge to void already begins after approximately 200-300 mL of filling volume (Lippert et al., 2010; Vaupel et al., 2015; Wyndaele, 1998). The voiding process is regulated by the peripheral and central nervous system and triggered by stimulation of tension receptors in the bladder wall after a certain threshold volume is reached (Giglio and Tobin, 2009). With increasing volume, afferent impulses are sent with higher frequency to the brain, where they are processed in the pontine storage and micturition centers. When micturition is then initiated, efferent signals are released that stop sympathetic outflow to the bladder and activate parasympathetic outflow over the pelvic nerves. They in return release acetylcholine, that stimulates muscarinic receptors in the detrusor, which is the muscular layer of the bladder wall, and promote smooth muscle contraction (see Figure 1).

Most common receptor types include M2 and M3 receptors here. Muscarinic receptors in the urothelium, which is the impermeable epithelial layer lining the inner surface of the urinary bladder, stimulate the release of a factor inhibiting the detrusor contraction (Chess-Williams, 2002).

In brief, before micturition occurs, the detrusor smooth muscle will relax to facilitate rising fill-levels inside the bladder without that the intravesicular pressure rises significantly and the bladder neck, urethra and pelvic floor further remain contracted to prevent involuntary voiding. Upon micturition the urethra and pelvic floor subsequently relax and the detrusor muscle contracts to enable voiding (Michel et al., 2005; Michel and Barendrecht, 2008).

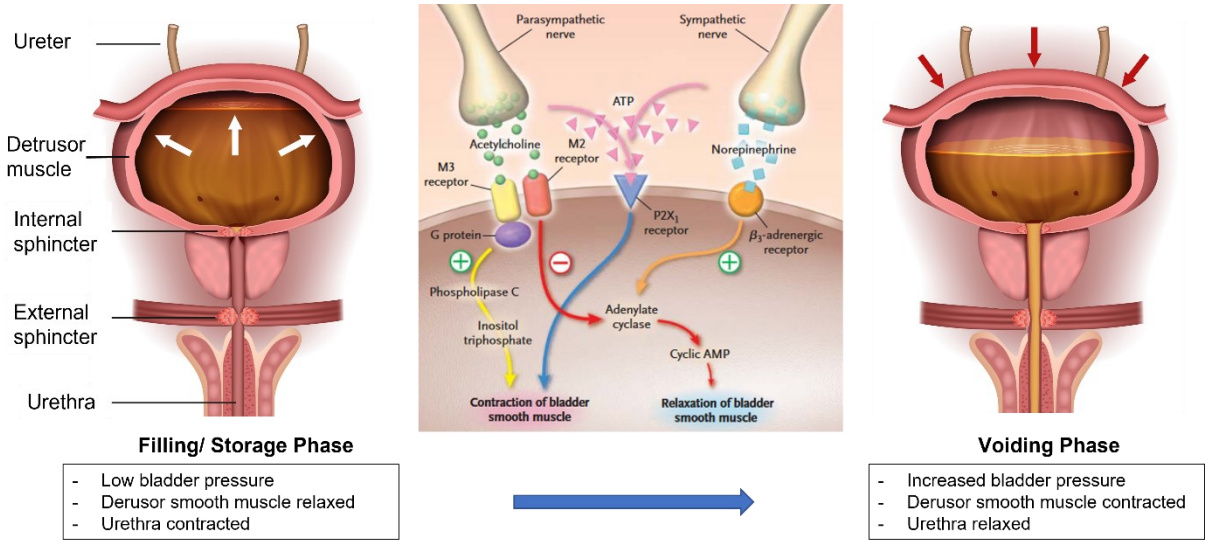

Figure 1. Scheme of urinary bladder during filling (left) and voiding (right) phase and receptor mediated contraction and relaxation of smooth muscle (middle). Modified and reproduced with permission from (Ouslander, 2004), Copyright Massachusetts Medical Society and Adobe stock.

While this process usually occurs voluntarily, this complex interplay can be out of balance for various reasons, such as age, diseases or inflammations and may then be the indication for drug therapy.

These facts have important implications on the urinary bladder as target for drug therapy. One unique advantage is, that it is accessible via the intravesical route and may therefore allow application of active pharmaceutical ingredients (APIs) through the urethra directly into the bladder. This opens up possibilities to apply drugs locally that are known to cause systemic adverse effects after oral administration. Further, the first-pass metabolism can thus be circumvented which in turn may facilitate application of lower drug doses. This can especially be desirable for elderly multi-morbid patients that would otherwise require high doses of multiple medications to achieve effective targeting of the diseased organ tissue (Palugan et al., 2021).

The difficulty, however, remains in maintaining a certain drug concentration within the bladder, since frequent voiding and constant production of urine cause washing out and dilution of the administered drug. When novel drug delivery systems are designed to remain within the bladder, it must be ensured that the urethra is not clogged at any time to avoid retention of urine. Another aspect to take into consideration is the impermeability of the urothelium, which can restrict the uptake of locally applied APIs and may require permeation enhancement (Crane et al., 2018; Tyagi et al., 2016). It can be beneficial for drug therapy, however, that the receptors that are expressed in the urothelium can be targeted directly through application of locally acting APIs.

Lastly, the fact that urinary tract disorders are a widespread and common problem for patients of different age groups and gender indicate the consistent need for effective drug therapy targeting the urinary bladder (Palugan et al., 2021).

1.2 Overactive bladder - pathophysiology and therapy

Bladder conditions are a common problem affecting more than half of the overall population. The prevalence of lower urinary tract symptoms thereby tends to increase with age (predominantly in women) and can cause significant reduction in the patient's quality of life (Coyne et al., 2008; Michel and Barendrecht, 2008; Milsom et al., 2001; Milsom and Gyhagen, 2019; Ruffion et al., 2013). A chronic symptom complex known as overactive bladder (OAB) was reported to affect more than 16 % of the adult population with a slight predominance for age-induced prevalence in women (Mckellar et al., 2019; Milsom et al., 2001; Murphy et al., 2013; Radomski and Barkin, 2012). It is defined as "urinary urgency, usually accompanied by frequency and nocturia, with or without urgency urinary incontinence, in the absence of urinary tract infections or other obvious pathology" (Haylen et al., 2010). Involuntary detrusor contractions during the filling phase of the bladder are typically considered the key symptom of this condition and cause uncontrolled voidings also at low bladder filling levels (Michel and Barendrecht, 2008). These symptoms come at great physical discomfort to the patients suffering from them and can also affect their social, professional, psychological and sexual aspects of life (Abrams et al., 2000; Coyne et al., 2008; Nicolson et al., 2008). Additionally, OAB causes significant financial burdens due to routine health care and treatment costs, but also costs suffered from loss of productivity at work (Tubaro, 2004).

The first-line treatment includes behavioural therapies such as fluid management and bladder or pelvic floor training. When this route of treatment fails or lacks satisfactory results, pharmacological treatment is indicated. Hereby, antimuscarinic drugs such as trospium chloride or oxybutynin can be administered, preferably formulated as an extended-release application due to lower incidences of dry mouth, which is a common adverse effect of the treatment. The antimuscarinic drug substance may thereby be given by itself or in combination with β_3-adreneceptor agonists. In severe cases it may even be an option to instruct patients to self-catheterize, although indwelling catheters are not recommended due to high risk of catheter-induced urinary tract infections or urethral destruction (Gormley et al., 2012; Lightner et al., 2019). Long-term therapy adherence, however, has been reported to be limited to approximately 10-36 % due to adverse effects of anticholinergic treatment and contributes significantly to preventable morbidity in patients which chronic conditions (Welk et al., 2021; Yeowell et al., 2018).

1.3 Drug delivery systems targeting bladder diseases

Oral (anticholinergic) drug therapy is the treatment of choice when behavioural therapies of chronic bladder conditions such as an overactive bladder fail. However, its adverse effects and lack of satisfactory symptom relief are reported to be some of the main reasons to cause discontinuation of

the treatment (Benner et al., 2010; Gormley et al., 2012; Jayarajan and Radomski, 2013; Marinkovic et al., 2012; Robinson et al., 2013). This contributes to the fact that such bladder conditions and their therapy have become a topic of interest for many research groups. Administering the API directly to the target site may thereby minimize systemic side-effects while taking advantage of the bladder's easy accessibility via the intravesical route. This treatment option is commonly used for administering liquid drug formulations directly into the bladder. Because these solutions are washed out of the bladder during voiding or quickly diluted by the patient's urine before clinically relevant drug concentrations are reached, optimization of such systems has been widely explored in the past (Crane et al., 2018; Kolawole et al., 2017; Lee and Choy, 2016; Palugan et al., 2021; Tyagi et al., 2016; Zacchè et al., 2015).

Mucoadhesive formulations (Kaldybekov et al., 2018) and hydrogels, nanotechnological formulations (McKiernan et al., 2011; Wang et al., 2012) or floating formulations (Wang et al., 2017) have been developed to avoid these problems and enable long-term therapy instead of frequently repeated drug administrations. Problems such as clogging of the urethra by highly viscous formulations or obstruction through the applied drug delivery device (DDD) at low filling levels, however, have limited their success. Efforts have also been made to enhance permeability of the urothelium to achieve sufficient transport of the API over the barrier to reach its target. Next to application of chemical agents such as dimethyl sulfoxide (Chen et al., 2003), one approach included electromotive drug administration. Here electrodes were placed inside the bladder and onto the abdomen to deliver electrical pulses that enhance permeation of the intravesically applied API (Di Stasi et al., 2003). The downside to these approaches is that the urothelium may be damaged and lose its functionality.

In order to develop a DDD that can be retained inside the bladder for a longer time, indwelling devices with sustained release characteristics such as osmotic systems have been explored that released the incorporated API for an extended period of time (Fraser et al., 2002; Lee and Choy, 2016; Nickel et al., 2012). Laar et al. developed an elliptical DDD with a central hole that was manufactured via electrospinning and incorporated the antimuscarinic drug trospium chloride. Although the API was released over an extended period of time, the release was inhomogeneous due to overlapping degradation and swelling effects (Laar, 2009). Haupt et al. developed lipid-based mini-tablet formulations incorporated in a tube made from silk proteins that were able to release the API trospium chloride over the course of a few weeks in therapeutically relevant concentrations (Haupt, 2013; Haupt et al., 2013). The downsides, however, are the complex manufacturing of the multi-component systems and the need for removing them cystoscopically after use that made the drug delivery systems suffer from poor overall applicability.

With new emerging technologies such as three-dimensional (3D)-printing, new approaches have been developed to design complex structures for a local application of APIs to overcome the limitations of the aforementioned therapies and avoid multi-step manufacturing methods. Melocchi et al. explored fused deposition modelling (FDM) printing of shape memory polymers to print structures that would be able to maintain a temporary shape suitable for application via catheter and would then obtain a permanent shape upon contact with water or urine to remain inside the bladder (Melocchi et al., 2019). While the approach is very innovative and the used polymer dissolves over time and must therefore not be extracted afterwards, it is limited to a very specific group of polymers that possess shape memory attributes and must further be thermoresistant to undergo the required extrusion process for generating feedstock material for the FDM printer and a second heating step during the printing process itself. The model API caffeine used for this study was released from the DDD within 2 hours and could therefore not sufficiently mimic a real-life application in which long-term administration of an active would be desired.

Xu et al. demonstrated the applicability of stereolithography (SLA) printing to manufacture a drug delivery system that could release the incorporated API over a more extended period of time (Xu et al., 2021). They designed a hollow and a solid flexible device to be printed with photopolymer resins by adding the API lidocaine hydrochloride into the elastic resin while the hollow devices were printed and subsequently filled with a drug-loaded mixture via syringe. Although the solid device was able to release the investigated API over the course of 2 weeks, the printed DDD would still need to be extracted. Further, the used polymer has not been approved in a pharmaceutical product so far.

Although these and many other developed DDD show the magnitude of interest there is currently in the field of developing superior treatment options, so far only oral formulations, transdermal patches and solutions for intravesical application are available to the patients. Those newly developed systems, that made it into clinical studies, unfortunately failed to make it beyond phase II clinical trials for unreported reasons or due to poor efficacy (Cima et al., 2014; Evans et al., 2021; Nickel et al., 2012).

The lack of success of the newly developed devices to make it to the market as well as the current interest in optimizing treatment options for patients suffering from various bladder diseases show that there is still a need for research and development enabling improved treatment for the urinary bladder.

1.4 Conceptualization of a novel intravesical drug delivery system

1.4.1 Requirements for the intravesical insert

The unique structure and physiology of the urinary bladder and their implications for drug therapy pose certain requirements for the development of intravesical drug delivery systems.

One apparent requirement is that the DDD must have a suitable shape to allow safe insertion via urinary catheter. This implies that it must not exceed a diameter of 6-8 mm or be able to maintain a temporary shape of these dimensions in which it can be applied. This in turn requires the insert to be flexible enough to withstand application and possibly fold and unfold for placement into a urinary catheter without damage. Flexibility and shape should also allow long residence of the device inside the bladder without causing irritation to the mucosa e.g., by sharp edges. Once inserted, the DDD should exhibit sustained release characteristics to avoid the need for frequently repeated instillations. It must thereby not clog the urethra to avoid urine retention inside the bladder but also not be too small in size to be eliminated during voiding. It would be desirable to incorporate pharmaceutically relevant polymers to ensure safety and tolerability of the device. Non-degradable or degradable polymers may be used for this purpose. The obvious advantage for biodegradable polymers is that they would not need to be extracted once the drug reservoir inside the insert is depleted. This aspect may however be compromised upon if the use of non-degradable polymers can compensate the discomfort of extraction by facilitating a longer application period. Another aspect to consider for degradable DDD is that upon degradation or disintegration no larger pieces or agglomerates should form that could potentially obstruct the urethra.

Flexible incorporation of different drug loads should further be an option to allow fabrication of differently dosed systems and accommodate APIs that would require both high or low drug loads.

1.4.2 Selection of model APIs

1.4.2.1 Trospium chloride

For the present work three different APIs were chosen as model compounds to develop and manufacture the intravesical drug delivery devices. Their selection was based on clinical relevance and the possibility to investigate the system's suitability for compounds with different physicochemical properties.

Trospium chloride (TrCl) was selected due to its well-established use for the treatment of bladder related conditions such as OAB (Madersbacher and Rovner, 2006).

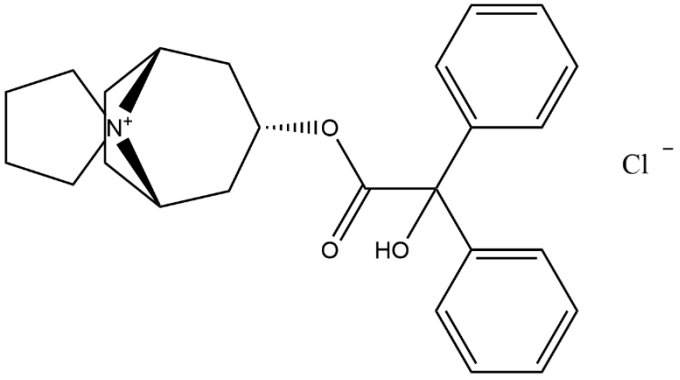

Figure 2. Chemical structure of trospium chloride.

As seen in Figure 2, it is a quaternary ammonium derivative of atropine. It is a permanently charged BCS class III anticholinergic agent that binds specifically to muscarinic receptors with a high affinity for M_1, M_2 and M_3 receptors causing smooth muscle relaxation (Madersbacher and Rovner, 2006). Due to its permanent charge, it is highly water soluble and therefore less likely to pass permeation barriers such as the blood-brain barrier as other antimuscarinics do. This makes TrCl especially suitable for local treatment when systemic side effects with other agents have been the cause for non-adherence to therapy. This hydrophilicity, however, is also reason for the low bioavailability of only approximately 10 % after oral administration, which is further reduced by more than 80 % when consumed with food (Doroshyenko et al., 2005; Heinen et al., 2013). After absorption from the upper gastrointestinal tract, it is bound at a magnitude of 50 - 80 % to proteins and has an elimination half-life of approximately 10-20 hours (Madaus, 2014). Typical dose regiment consist of a twice daily oral intake of 20 mg trospium chloride (Guay, 2005). 70 – 80 % of the absorbed trospium chloride is renally eliminated and therefore requires dose adjustment for patients with severe renal insufficiency. Most of the absorbed API is eliminated unchanged via urine, which has been reported to possibly have contributed to its positive local pharmacological activity (Madersbacher and Rovner, 2006). In contrast to the other antimuscarinic agents, it is not metabolized via the hepatic CYP system (Zinner, 2006).

Although the blood-brain barrier permeability of trospium chloride is assumed to be very low, some studies have indicated that a certain risk of penetration into the central nervous system is given for patients with a modified blood-brain barrier (Liabeuf et al., 2014). For these patients in particular, local application of the API could be beneficial.

Studies in isolated pig bladder models have shown, that intravesical administration of trospium chloride was dose-dependently effective at a minimal concentration of 1 µg/mL (Laar, 2009; Von Walter, 2009). This concentration was therefore applied as the minimal target concentration for the present work.

1.4.2.2 Lidocaine hydrochloride monohydrate

In order to reduce the costs during printing trials, a model API for trospium chloride was selected. Lidocaine hydrochloride monohydrate's (LC-HCl) molecular structure is fully ionic as well and the mean particle size as well as the solubility were determined to be comparable to trospium chloride which made it an ideal candidate as model API for trospium chloride (Haupt, 2013; Sládková et al., 2015).

Lidocaine hydrochloride is commonly used as a local anesthetic and class 1b antiarrhythmic drug. It belongs to the group of amides and targets the sodium channels located within the cell membranes. After membrane penetration, it binds in its protonated form to the inner part of the sodium channel and so prevents the formation of action potentials.

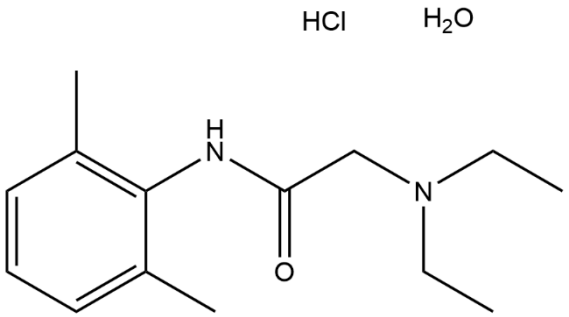

Figure 3. Chemical structure of lidocaine hydrochloride monohydrate.

Due to its anesthetic effect, it is widely applied in urologic practice before painful catheterizations or cytoscopic procedures. Various aqueous solutions and lidocaine-loaded topical gels are available for this purpose (Pedraza Sanchez et al., 2019).Their downside, however, is that they are quickly washed out of the bladder during voiding and cannot be retained within the bladder for an extended period of time.

Intravesical drug delivery devices were developed in the past to overcome this problem, e.g. by constructing a silicone tube filled with lidocaine salt crystals and a shape memory wire to obtain a pretzel like confirmation for bladder retention (Lee and Cima, 2011). The lidocaine-releasing intravesical system (LiRIS) was based on this approach and contained lidocaine hydrochloride in minitablets. The drug release was driven osmotically through a small orifice and enabled continuous dissolution over the course of 2 weeks. In phase 1 clinical trials it was found that the application of approximately 130 mg of lidocaine in 14 days was sufficient to relieve symptoms of interstitial cystitis or bladder pain syndrome (Nickel et al., 2012). However, the device has not been commercially approved until now.

Incorporation of LC-HCl into the newly developed intravesical DDD was therefore an interesting subject to demonstrate its feasibility, both as model API for TrCl and for an alternative treatment option.

1.4.2.3 Hydrochlorothiazide

Hydrochlorothiazide (HCT) was selected as third model API due to its poor water solubility (Ph. Eur. 10, 2020a). HCT is a BCS class IV thiazide low-ceiling diuretic drug for the treatment of edema and hypertension.

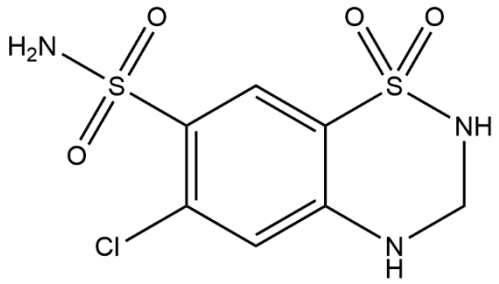

Figure 4. Chemical structure of hydrochlorothiazide.

It works primarily via inhibition of sodium reabsorption in the distal tubules and causes an increased elimination of electrolytes and osmotically bound water (Babu et al., 2014).
HCT has a plasma half-life of approx. 6 - 14 hours (Sanphui and Rajput, 2014). After oral administration 80 % is resorbed from the GIT and approx. 70 % is systemically available. 95 % of the API are eliminated unchanged renally.
Although HCT does not have a clinical relevance for intravesical applications, it was considered beneficial to investigate the feasibility of incorporating poorly soluble APIs into the drug delivery devices and their effect on drug release and to demonstrate the range of applicability.

1.5 Semi-solid micro-extrusion 3D-printing as manufacturing tool

1.5.1 Semi-solid micro-extrusion in pharmaceutics

By now, multiple 3D-printing techniques, e.g. binder jetting and selective laser sintering, have been investigated for their applicability in pharmaceutics (Jacob et al., 2020). The versatility, flexibility and on-demand nature of the processes have made them a focus point for pharmaceutical innovations regarding personalized therapies. Amongst the many technologies that have evolved from additive manufacturing of pharmaceuticals since the late 1990s (Rowe et al., 2000; Wu et al., 1996), semi-solid micro-extrusion (ME) has found special attention. As the name suggests, semi-solid inks such as pastes or gels are used to create three-dimensional objects in a layer wise manner. Filament-based printing technologies (commonly known as *fused deposition modeling*) are not considered part of semi-solid ME, although melting of the feedstock filament causes a liquid or semi-solid intermediate before solidification. Even though its implementation in pharmaceutics has only begun a few years ago in 2014 (Khaled et al., 2014), a vast number of research groups have focused on reaping its benefits for manufacturing of drug-loaded dosage forms. Amongst other advantages, pharmaceutical ME is able to accommodate a wide variety of excipients to form the semi-solid ink formulation. Developing precursor inks that can quickly incorporate a range of different actives without fear of cross-contamination due to the use of disposables may bridge the gap to implementation of the technology in decentralized settings, e.g. in hospital or community pharmacies.
When considering conventional manufacturing of oral dosage forms such as tablets, printed medicines offer possibilities to tailor release profiles or the dispensed dose by changing the tablet geometry (Korte and Quodbach, 2018; Pietrzak et al., 2015). This can help personalizing drug therapy or overcoming dosing inaccuracies due to tablet splitting when the right dose is not available (Zheng et al., 2020). Large scale production, however, is limited to the technology's throughput, which is a compromise between manufacturing time and resolution of the printed object. While the comparably low resolution of ME-objects can cause poor visual appearance, acceptability of the final dosage forms

does not have to be limited by it. Recent studies have shown that the possibility to modify shape, color and taste of oral dosage forms as well as its unique opportunity to manufacture chewables, causes especially pediatric patients to prefer ME-dosage forms over others (Januskaite et al., 2020). In contrast to other printing technologies, semi-solid ME can be carried out at room temperature at moderate pressures and has, therefore, been widely exploited by bioprinting communities to print living cells for organ tissue engineering or organ-on-a-chip models (Duan et al., 2013; Zhang et al., 2016). It enables the microfabrication of tissue or organ models to mimic in-vivo conditions. It also allows estimations of the effects of drug delivery systems and has the potential to eliminate ethical concerns and other difficulties caused by animal or human trials (Bhise et al., 2016; Chang et al., 2010; Matai et al., 2020).

Due to its many favorable qualities, semi-solid micro-extrusion was selected as suitable 3D-printing technology for the present work. Its use in the present study may enable a local application of active pharmaceutical ingredients for various bladder conditions such as OAB and may thus overcome systemic side-effects of orally applied drugs and allow lower concentrations to be applied. One essential factor was considered the possibility of processing a wide variety of polymers fairly easily at low temperatures into printable inks to generate flexible objects. This flexibility was assessed to be crucial for the applicability of the intravesical drug delivery devices.

1.5.2 Printing principle

The general printing principle of semi-solid micro-extrusion did not change significantly since its inception by Landers and Mülhaupt in 2000 (Landers and Mülhaupt, 2000; Mülhaupt et al., 2001). Similar to other additive manufacturing techniques, objects are created layer-wise via the repetition of specific process steps. The commands for the printer are defined by the digital design file and a subsequent slicing process, in which the desired geometry is translated into a machine language. In the case of ME, a semi-solid material, e.g. a polymer solution or hotmelt, is extruded from a cartridge through a nozzle of a given diameter onto a printbed or into a plotting medium. Pressurized air or a motorized piston are commonly used to generate the pressure necessary for the extrusion process. A kinematic system allows the printhead containing the semi-solid and the printbed to move independently of each other, enabling a combined movement in x-, y- and z-direction. Before printing of the first layer, the calibration of the nozzle in the x-, y- and z-axes needs to be performed. Depending on the printer, this is performed either fully automatically or semi-automatically. The first layer of the 3D object is created by lowering the nozzle to a defined height and position over the printbed. Material is extruded through the nozzle via the application of pressure and the kinematic system moves the nozzle over the printbed laterally along a pre-determined path. Once printing of the first layer is

finished, extrusion is halted and the nozzle or printbed moves along the z-axis to a pre-set height above the first layer. After repositioning the nozzle to the correct starting position, printing of the second layer starts. This process cycle is repeated until the object is finalized.

After extrusion of the semi-solid solidification takes place. Several routes are possible for solidification, among them crystallization, glass transition of thermoplastics, coagulation of polymer suspensions, drying, precipitation of polymer solutions, physical or chemical crosslinking, formation of polyelectrolyte complexes or printing in liquid non-solvents (Ligon et al., 2017). Also depending on feedstock properties, different modes of pre- and post-processing might be required. For most applications, the printhead consists of a temperature-controlled jacket for single-use syringes with single-use nozzles. Many printer manufacturers settled for disposables for every part in contact with the ink or formulation to reduce the risk of cross-contamination and facilitate sterilization. Connectors are used to fix the air supply or motorized piston to the syringes. Plungers can be inserted in the syringe before it is connected to the air or piston to ensure that gas entrapped in the ink does not escape, to completely wipe off the walls and to seal-off the printing system from solvent vapor stemming from the printing formulation. Depending on the printer, the printbed can also be temperature controlled. Besides the basic printhead design, a wide range of printheads is available for most ME printers (Ozbolat, 2016). These include, among others, high and low temperature printheads, printheads for multiple materials and co-axial printing, printheads equipped with UV-sources or lasers for crosslinking of photo-reactive inks and printheads for (melt) electrospinning. This allows the combination of different manufacturing techniques in a single process.

1.5.3 Process parameters

There is not one set of process parameter settings for all inks because of the wide range of suitable excipients, dispersants and solvents. Yet, the process is versatile enough to identify suitable process settings for most inks. The pressure difference Δp between the inside of the cartridge and the environmental pressure is the driving force for extrusion. Considering a liquid with the simplest rheological properties, a Newtonian fluid, a constant Δp results in a constant volumetric material flow and changes of Δp lead to respective changes of volumetric flow. When a constant Δp is applied, the printhead speed in the x-y-plane determines the thickness of the extruded strand (Tirella et al., 2009). The quicker the printhead moves, the lower the extruded amount per distance, the thinner the strand and vice versa. This can be used to improve the quality of prints as the spatial resolution of ME 3D-printing depends on the strand diameter (Linares et al., 2019). Decreasing Δp might also lead to narrower strands, as long as the yield stress σ_0 of the ink is exceeded. Velocities above the tear off speed, the speed where no continuous filament is formed anymore, need to be avoided. The layer

height determines, among other factors, the thickness of the deposited layers and may influence multiple quality attributes of the printed dosage forms, such as visual appearance and mechanical properties. Generally, the surface finish is better with lower layer height and even though a good visual appearance is favorable (Marques et al., 2019), the trade-off for lower layer height is an increased printing time. Another influential process setting is the jacket temperature of the printhead. It highly impacts the viscosity of the semi-solid or thermoplastic solid (Dores et al., 2020). A reduced viscosity due to a higher jacket temperature can enable printing at lower Δp and reduce the shear stress, which might be beneficial for certain formulations or cell-laden inks. While the influence of printhead temperature is mostly straightforward, the influence of the printbed temperature is more complicated as it serves multiple purposes. It can be modified to speed up the solidification process (via evaporation, $T \uparrow$, or glass transition, $T \downarrow$) but always has to be in a range that allows proper material adhesion. Furthermore, it can be adapted to decrease warping of material during drying.

The influence of process parameter variations and ink viscosity η on the printing process and object for a Newtonian fluid are listed in Table 1. Potential approaches to compensate the parameter changes to return to similar values of the strand diameter D_{strand} and feature resolution $x, y_{feature}$ are listed as well.

Table 1. Influence of process parameter changes and ink viscosity on printed structure and ink properties and approaches to compensate for the changes. Arrows in brackets indicate a limited influence. The table is only valid for Newtonian fluids. According to (Rahman and Quodbach, 2021) by courtesy of Elsevier.

	Effect			Compensation			
Modification	$\boldsymbol{D_{strand}}$	$\boldsymbol{x, y_{feature}}$	$\boldsymbol{\eta}$	$\boldsymbol{\Delta p}$	$\boldsymbol{v_0}$	$\boldsymbol{T_{jacket}}$	$\boldsymbol{\eta}$
$\boldsymbol{\Delta p} \uparrow$	↑	↓	-	-	↑	↓	↑
$\boldsymbol{h} \uparrow$	↓	↑	-	(↑)	(↓)	(↑)	(↓)
$\boldsymbol{v_0} \uparrow$	↓	↑	-	↑	-	↑	↓
$\boldsymbol{T_{jacket}} \uparrow$	↑	↓	↓	↓	↑	-	↑
$\boldsymbol{D} \uparrow$	↑	↓	-	↓	(↑)	(↓)	(↑)
$\boldsymbol{\eta} \uparrow$	↓	↑	-	↑	↓	↑	-

1.5.4 3D-Bioplotter

The pressure-assisted microsyringe (PAM)-operated 3D-Bioplotter from EnvisionTec GmbH (Germany) was used to manufacture the intravesical inserts in the present work.

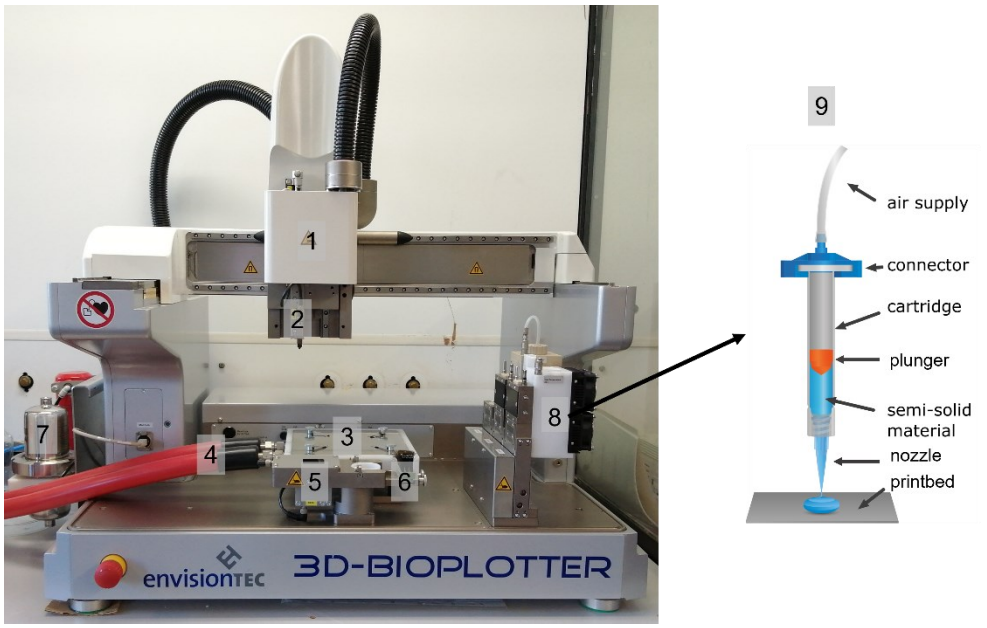

Figure 5. 3D-Bioplotter with numbered components and image of syringe to be inserted into low temperature print head modified from (Rahman and Quodbach, 2021) by courtesy of Elsevier.

The 3D-Bioplotter consists of the following key components (see Figure 5 for reference):

1. Print head carrier
2. Platform height control sensor
3. Printbed (temperature controlled from -10 – 80 °C)
4. Connection to Mini-chiller (temperature controlling system for printbed)
5. Photo calibration station
6. Cleaning station
7. Sterile and particle filters
8. Print heads in park position:
   - Low temperature print head for disposable polyethylene cartridges (volume: 30 mL) covering a temperature range from 0 – 70 °C
   - High temperature print head for a reusable stainless-steel cartridge (volume: 10 mL) covering a temperature range from 30 – 250 °C
9. Scheme of disposable syringe to be inserted into low-temperature print head

For calibration before printing, the platform height control sensor that is connected to the printhead, will touch upon the middle of the printbed and register the distance. Further, the needle-tip mounted to the cartridge will be lowered into the photo-calibration station to ensure the correct distance and placement of the needle to the platform.

Depending on the material properties (such as melting point, T_g, viscosity etc.) of the printing ink, the respective printhead is chosen to apply the required temperature. Further, the printbed temperature may be varied to aid the post-processing solidification or ensure sufficient adherence of the first layer to the printbed.

This printer setup was selected for manufacturing of the intravesical inserts due to its precision and possibility to process a wide range of materials due to the wide temperature range that can be covered. Further, the possibility of using disposable sterile syringes as well as the built-in particle and sterile filters for the input compressed air make it an ideal candidate to manufacture DDD that would require sterile manufacturing. Aseptic manufacturing can easily be implemented by placing the Bioplotter into a biosafety cabinet and using sterile disposable materials for parts that are in direct contact with the printing ink. Another key advantage of this printing technology is, that this manufacturing technology allows fabrication of highly flexible geometries, which was essential to this work.

1.6 Biopharmaceutical bladder model

1.6.1 Dissolution testing in compendial setups and their limitations

When designing intravesical DDDs, the main objective is usually to achieve a certain drug concentration within the urinary bladder which should remain within the therapeutic window of the API and allow effective treatment. Monitoring such concentrations is therefore of vital importance to understand whether treatment may be successful. In-vitro dissolution testing is commonly applied to investigate suitability of a given formulation and allows certain predictions regarding in-vivo performance that may also speed up regulatory processes when bioequivalence studies can be shortened. However, these predictions may only be valid, when dissolution conditions are chosen carefully and meaningful (Dressman et al., 1998). Previous studies have shown, that modifying dissolution setups in order to take more biorelevant conditions into account has led to significant differences in the resulting release profiles (Bassand et al., 2022; Speer et al., 2019; Stewart et al., 2020).

For intravesical preparations, so far only the conventional pharmacopeia apparatuses are available to determine drug release, that insufficiently mimic the conditions within the urinary bladder and there is no standardized compendial method available yet (Brown et al., 2011; Ph. Eur. 10, 2020b, 2020c; Siewert et al., 2003). Steady production of urine causes dilution of the drug present in the bladder and can be very different from patient to patient depending on their average fluid intake or on medical conditions such as e.g., diabetes insipidus. Furthermore, in case of OAB, frequent voiding can change the current concentration of the API throughout the course of treatment. Determination of drug concentrations, therefore, is difficult with the conventional testing methods. Additionally, it is unclear how to analyse the data from pharmacopeial dissolution testing for such locally acting drug delivery

systems. Neither a cumulative nor a differential analysis are ideal. The commonly applied cumulative plot has the disadvantage that the amount of drug that has been previously released (e.g. several days ago) is not relevant to the effectiveness of therapy at later time points. The differential plot better reflects the drug release going on at any given point in time but does not provide information on the concentration in the dissolution medium. Knowledge of this concentration is however critical since it is decisive for the effectiveness of local drug therapy.

1.6.2 Requirements for the development of the new bladder model

To overcome the limitations of the compendial dissolution setups for release testing of intravesical preparations, development of a new biopharmaceutical bladder model was necessary.

Bladder models have been designed in the past to simulate surgical procedures (Wong et al., 2017), investigate pressures within the bladder (Weaver et al., 2010) or to study effects of catheterization related problems (Kazmierska et al., 2010; Schulz et al., 2008; Stickler et al., 1999). Apart from that, regenerative medicine has focused on developing biomaterial-based bladders (Chae et al., 2022; Sharma and Basu, 2022) and tissue engineering (Korossis et al., 2006). Other models were developed to study urinary tract infections or other bladder related diseases (Xiong et al., 2021).

Besides using isolated pig bladders in an experimental setup (Laar, 2009; Von Walter, 2009), intravesical preparations have been tested in self-made constructions or variations of the compendial setup that were still far from physiological conditions (Haupt, 2013; Melocchi et al., 2019; Xu et al., 2021).

Those systems have some substantial drawbacks when it comes to taking (patho-)physiological conditions into account and at the same time enabling reproducible measurements.

Therefore, the following requirements have been the base for this work to design a biopharmaceutical bladder model for determining the drug release under more physiological conditions.

Most importantly, physiological conditions such as anatomical features, changing (urine-) volume, voiding mechanism, movement and body temperature should be taken into account based on average values from (adult) humans. Since patients have interindividual differences and different (patho-) physiological conditions should possibly be investigated, those features should be adaptable to a certain extent. Ideally, the model should be able to be operated fully automated to be able to investigate drug release over an extended period of time and account for sampling intervals throughout the entire study period. Important for the evaluation of efficacy of a given therapy is the determination of actual local drug concentrations at predefined timepoints. Additionally, it was considered beneficial, if the tested inserts could be observed during dissolution testing to understand their behavior inside the bladder. Therefore, glass or clear plastic was preferred for construction of parts surrounding the bladders as well as the bladders themselves. This would have to come at the

expense of having a flexible bladder. The bladder itself should be modeled together with the urethra to provide the opportunity of simulating the insertion process of the DDD.

2 Aim of the thesis

The present work focuses on semi-solid micro-extrusion 3D-printing of flexible, drug-loaded intravesical inserts for bladder targeting.

The aim was to enable local application of different APIs with different physicochemical properties to potentially overcome limitations of orally applied drugs. For this purpose, trospium chloride (TrCl), lidocaine hydrochloride monohydrate (LC-HCl) and the model drug hydrochlorothiazide (HCT) were selected.

The second focus of the thesis was the development of a biopharmaceutical bladder model for dissolution testing of the newly developed inserts.

In more detail, the aims of the thesis were:

- Development of flexible inserts for a controlled long-term presence in the urinary bladder consisting of:
  - Different matrix materials (degradable and non-degradable polymers)
  - Three APIs with varying physicochemical properties
  - Different geometries and drug-loads for fine-tuning of the drug release
- Characterization of the printing formulations and printed inserts
- Development of a biopharmaceutical bladder model for in-vitro drug release studies
  - Comparison to compendial method
  - Variation of model parameters to investigate release under different (patho-) physiological conditions

3 Results and discussion

3.1 Development of printable (drug) formulations and process understanding

3.1.1 Introduction and objectives

The first step towards developing intravesical drug delivery systems is to develop a suitable printing ink that will serve as feedstock material for the 3D-Bioplotter. Of key importance here are the selected excipients and their viscoelastic behavior. Polymer selection was based on the degradable or non-degradable nature of the polymer and their ability to form highly flexible objects. Additives to ensure flexibility and to obtain a semi-solid formulation such as plasticizers or solvents should be added only when necessary. Characterization of rheological behavior of the formulation can give valuable insights into process understanding and assist formulation development. The formulation must be processable by the 3D-printer without causing any nozzle blockage and must be able to generate objects with high shape fidelity.

Depending on the intended application and required degree of optimization, formulation development for ME can be a complicated matter for many reasons. First of all, the rheological behavior of real ME formulations is preferably shear-thinning and therefore non-Newtonian. Non-Newtonian fluids usually display a time-dependent component and are often visco-elastic (Azad et al., 2020). This flow behavior enables printing of formulations that would be too viscous otherwise. Secondly, it has been observed that slight changes to the formulation require the adaption of multiple process parameters (Cheng et al., 2020; Chung et al., 2013). Thirdly, pharmaceutical ME is still a young manufacturing technique and there is no agreement on CQAs that formulations and printed dosage forms need to be optimized for Lastly, the wide range of available ME printers with different pressurization systems, temperature controls, cartridge diameters, nozzle shapes and nozzle diameters do not allow for a generalization of formulation properties. Formulations that are accurately printable on one printer may not be processable on another printing system or when using another nozzle diameter. Specific values are of little use unless the identical setup available as in the cited study can be employed. If a highly optimized ink with as robust as possible characteristics and print performance is required, formulation development requires time, a high degree of understanding of the influencing factors and thorough iterative optimization. On the other hand, it is fairly simple to obtain a printable ink with somewhat worse but still good printing performance with few experiments and little optimization via trial-and-error approaches.

Understanding the flow behavior of an ink is key to developing a suitable printing process and to generate profound knowledge of the process capabilities. The general requirement for pharmaceutical inks is that formulations should be semi-solid and, thus, have a yield point (Mouser et al., 2016). The yield point of a pharmaceutical ME formulation can be directly measured in a rotational shear ramp experiment as the yield shear stress τ_0 where flow is initiated for the first time (see Equation 1), which can be translated to the printing process.

$$\tau = \tau_0 + K(\gamma)^n \qquad for\ \tau \geq \tau_0 \qquad \text{Equation 1}$$

τ: flow stress; τ_0: yield flow stress; K: flow consistency index; n: flow behavior index; γ: viscoelastic flow rate

Similarly, the yield flow point τ_0 can be determined in an oscillatory experiment at the cross-over point where the loss modulus G'' becomes larger than the storage modulus G' (Chung et al., 2013). The storage modulus G' represents the elastic part of a formulation, the loss modulus G'' the viscous part. Consequently, the cross-over point is the shear rate when the viscous part begins to dominate the flow behavior and the formulation begins to flow. The yield point can be increased by adding more polymer and vice versa (Cheng et al., 2020). Once flow is initiated, shear-thinning flow behavior is favorable, as the required pressure for the extrusion through the nozzle is reduced (Aho et al., 2015; Cheng et al., 2020). For maximum structural integrity after printing, no time-dependent flow behavior should be present, i.e. no thixotropy. As most polymer solutions and melts display thixotropy, a quick recovery of the initial viscosity should take place, to ensure maximum shape fidelity (Conceição et al., 2019).

After first formulations have been developed, their suitability for printing must be assessed. Therefore, the printed object must be able to withstand gravitational forces and form defined strands and layers with sufficient structural integrity. Fine-tuning between process parameters and formulation development is critical for achieving satisfactory print quality. In order to evaluate the quality and success of a print, it must first be clear how quality is defined.

In bioprinting and partially in pharmaceutical ME the term printability is used to describe all relevant characteristics. Printability is usually understood as “the ability of a bioink or a set of printing parameters to be used for extrusion bioprinting” (Gillispie et al., 2020) or as the ability of an ink to retain the desired shape with high fidelity (Chung et al., 2013; Yang et al., 2020). The time point when the shape fidelity is determined can also have an impact on the obtained value. While the printed object may seem to have high shape fidelity directly after printing, it may change over time when printed layers flow together or structures collapse due to the weight of the next layers.

However, there is still no consensus about the definition of printability. Some researchers present holistic approaches to cover several parameters related to printability.

Paxton et al. introduced a two-step screening method to assess the printability of bioinks (Paxton et al., 2017). The first step consists of a manual dispensing of the test ink through a 250 µm nozzle to investigate if drop or proper strand formation occurs and if layers stack on top of each other or if they coalesce. This approach has been widely adapted and is called the layer stacking test (O'Connell et al., 2020). The second step comprises rotational rheometry experiments to identify the yield stress, shear-thinning behavior and structural recovery. By investigating the relationship between printing pressure, the extruded material volume and the printhead speed for different nozzle radii, the authors defined windows of printability for different formulations.

Independent of the chosen development approach and understanding of shape fidelity, there is no universal procedure on how to select the width of a printed filament or the layer height. In our experience, processes with a suitable ink lead to defined and acceptable results when the layer height is between 65 % - 80 % of the nozzle diameter and the line width is equal to the nozzle diameter. A layer height in this range leads to adequate contact area and structural integrity of the strands. A line width much larger than the nozzle diameter is a sign of over-extrusion where too much material exits the nozzle and is displaced to the side. This process state lacks satisfactory control, as the final line-width can differ considerably. A narrower line width than the nozzle width represents under-extrusion, which might be used to deposit thinner strands at higher speeds. However, in ME larger deposition volumes are frequently desired and under-extrusion would be a cause for further process optimization. Also, it has to be mentioned that extensive assessment of the printability is not strictly necessary to obtain acceptable print results, as demonstrated by multiple researchers in pharmaceutical ME (El Aita et al., 2019; Khaled et al., 2018, 2015). Yet, to gain a better understanding of the fundamental impact factors of excipients and process settings, thorough analyses are indispensable.

The first objective of the current work was therefore to develop printable feedstock material for the 3D-printer for manufacturing of the intravesical inserts. Efforts were made towards gaining process understanding and identifying critical quality attributes of the printing ink to be able to obtain reproducible prints. After identifying suitable excipients for formulation development, the semi-solid formulations were rheologically characterized and critical process parameters were identified. After selecting and designing a suitable geometry for the printed inserts, optimization of the printing conditions was investigated via a design of experiments to obtain prints with high shape fidelity. For this purpose, quality defining descriptors were defined and newly introduced that allowed characterization of the printed objects. Further, the effect of post-process drying on the properties of the final inserts was investigated to determine suitable drying conditions.

3.1.2 Excipient screening for the development of semi-solid printing formulations

3.1.2.1 Polymers and solvents

Based on literature research, non-degradable and degradable polymers were selected for formulation development. It was important to select polymers that were known to be biocompatible and therefore safe for insertion and preferably already established for pharmaceutical applications. For the biodegradable polymer it was further important that the degradation products of the polymer were non-toxic.

The non-degradable insert was based on the well-established polymer ethylene vinyl acetate copolymer (EVA) that has been used in the past to manufacture various marketed products such as NuvaRing® that eludes hormones over the course of three weeks (Organon, 2022; Schneider et al., 2017). It was therefore already proven to be flexible, highly biocompatible, and suitable for long-term application. Additionally, it has also been used for 3D-printing applications in the past (Genina et al., 2016). For the present work a grade was selected with a high vinyl acetate (VA) content. An increased VA content will inhibit crystallization of the polyethylene chain segments and achieve a softer polymer even without addition of plasticizers (Schneider et al., 2017).

The first degradable inserts were based on the polymer poly(ε-caprolactone) (PCL) due to its known biocompatibility and degradation (Konta et al., 2017). It has also been used in the contraceptive implant Capronor® that releases levonorgestrel over the course of 12-18 months (Darney et al., 1989). It was further selected due to its low melting point and high flexibility (Ulery et al., 2011) and has been used in the past also in 3D-printing applications to manufacture scaffolds or drug eluting systems (Fu et al., 2018; Yeong et al., 2010). For this work a grade with low molecular weight was selected to ensure faster degradation and higher flexibility as well as a lower viscosity during printing.

Since the melt-viscosity of both polymers turned out to be too high even at temperatures above 200 °C to be processed by the Bioplotter, a solvent was required to obtain semi-solid printable formulations. After screening various common organic solvents including acetone, ethyl acetate, toluene, methanol, xylene, chloroform, cyclohexane and tetrahydrofuran (THF), chloroform and THF showed the most promising capability of sufficiently dissolving both polymers. Due to its lower toxicity, THF was selected as solvent for further formulation development. According to the *ICH Guideline for Residual Solvents Q3C(R8)* THF is classified as class 2 solvent and has a permissible daily exposure of 7.2 mg (ICH Expert Working Group, 2021). This indicates, that drying the object after printing is crucial to ensure safety of the insert.

In first small-scale trials the polymers were mixed with the solvent on a heating plate in different ratios and manually extruded from a 5 mL syringe for initial evaluation. It became apparent from these trials that a plasticizer would be required to provide sufficient flexibility.

3.1.2.2 Addition of plasticizers

Plasticizers are pharmaceutical excipients which may be added to polymer formulations to reduce brittleness and enhance flexibility through their intercalation between the polymer chains.

Various plasticizers were investigated for formulation development with focus on the biodegradable PCL formulation. This was particularly necessary since the trials with only polymer and solvent resulted in rigid structures. A soft and flexible insert would be desired to avoid harming the bladder mucosa as reported for some of the larger, more rigid systems described in the literature (Chancellor, 2001; Nickel et al., 2012).

Therefore, for initial evaluation and comparison of various plasticizers, formulations were prepared according to the compositions in Table 2 and cast as films. This approach allowed simple determination of mechanical and visual properties at an early stage of development.

The incorporation of highly polar plasticizers such as glycerol or polyglycol was not feasible and was therefore discarded from further studies. Stearic acid did not mix homogeneously with the polymers either which could be seen as a white tarnish in the formulations.

Table 2. Composition of formulations for plasticizer screening. All values given as % [w/w] (PCL: polycaprolactone, PEG: polyethylene glycol, CA: citric acid, SA: stearic acid, TEC: triethyl citrate, OA: oleic acid, DBS: dibutyl sebacate, TA: triacetin, MCT: medium-chain triglycerides).

No.	PCL	THF	Glycerol	Sorbitol	PEG 400	CA	SA	TEC	OA	DBS	TA	MCT
1	1.5	7.0	-	-	-	-	-	-	-	-	-	-
2	1.5	7.0	1.5	-	-	-	-	-	-	-	-	-
3	1.5	7.0	-	1.5	-	-	-	-	-	-	-	-
4	1.5	7.0	-	-	1.5	-	-	-	-	-	-	-
5	1.5	7.0	-	-	-	1.5	-	-	-	-	-	-
6	1.5	7.0	-	-	-	-	1.5	-	-	-	-	-
7	1.5	7.0	-	-	-	-	-	1.5	-	-	-	-
8	1.5	7.0	-	-	-	-	-	-	1.5	-	-	-
9	1.5	7.0	-	-	-	-	-	-	-	1.5	-	-
10	1.5	7.0	-	-	-	-	-	-	-	-	1.5	-
11	1.5	7.0	-	-	-	-	-	-	-	-	-	1.5

The successfully cast and dried films were characterized via puncture test (see section 5.2.8.13.1). With this setup, force distance diagrams were obtained as exemplarily shown in Figure 6.

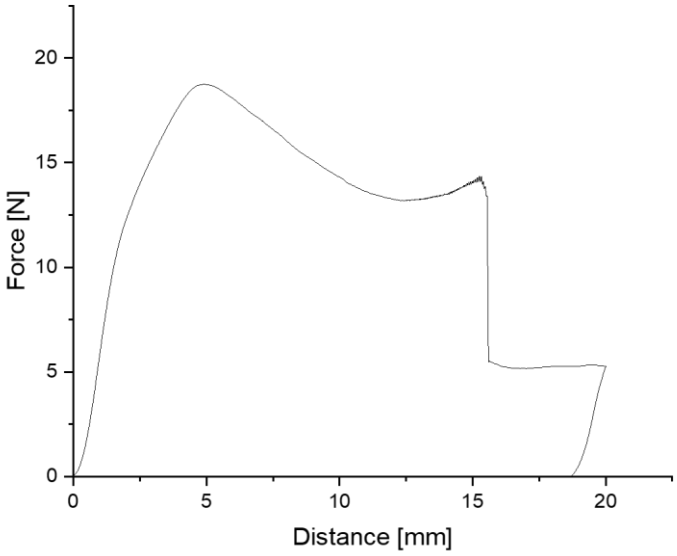

Figure 6. Exemplary force-distance diagram obtained during puncture test of cast films containing polycaprolactone and plasticizer.

The curves showed multiple regions corresponding to different responses to the applied strain. After an initial elastic deformation (linear ascending part of the curve), plastic deformation occurred, which was no longer reversible. After a peak force was registered, a drop in force was detected corresponding to the film losing its integrity. This can be caused by small ruptures in the film or parallel arrangement of the polymer chains to each other causing less resistance to deformation. Re-arrangements may also cause a stiffening of the material that is observable as increased forces until major ruptures occur, and the curve drops parallel to the y-axis.

Since the obtained films were highly flexible and not all films ruptured during the test, the slope was calculated from the linear regions in the ascending part of the curve before plastic deformation occurred. Smaller values were considered beneficial because this corresponds to a less steep slope and therefore less force being required to deform the films.

Table 3 shows the results of the puncture test and visual evaluation. Formulations for which plasticizer incorporation was not feasible, were discarded immediately. Upon drying, some of the films revealed a white tarnish indicating precipitation or re-crystallization and were also discarded.

Table 3. Results of puncture test and visual evaluation of cast films composed of polycaprolactone and plasticizer; mean ± sd, n=3 (n.a.: not applicable; -: incorporation of plasticizer was not feasible/ poor visual properties due to inhomogeneous film; +: incorporation of plasticizer feasible/ homogeneous films obtained).

No.		Incorporation feasible	Slope [N/mm]	Visual evaluation
1	Without plasticizer	n.a.	13.8 ± 0.6	-
2	Glycerol	-	-	-
3	Sorbitol	-	-	-
4	PEG 400	-	-	-
5	Cetylalcohol	-	-	-
6	Stearic acid	-	-	-
7	Triethly citrate	+	5.9 ± 0.7	-
8	Oleic acid	+	7.5 ± 0.3	-
9	Dibutyl sebacate	+	8.5 ± 0.3	+
10	Triacetin	+	9.4 ± 0.3	+
11	Medium-chain triglycerides	+	10.4 ± 0.5	+

The best results were achieved with dibutyl sebacate (DBS) as plasticizer, which was evident by obtaining a smooth and homogeneous film with the smallest slope determined via puncture test. Therefore, DBS was selected for future formulation development.

For the EVA formulation, it was observed that the films were already quite flexible and therefore only required addition of very little amounts of plasticizer to improve their handling. Also here, DBS was selected due to its easy incorporation resulting in smooth and homogeneous films.

3.1.3 Rheological characterization

3.1.3.1 Rotational rheometry

3.1.3.1.1 Hershel-Bulkley fit

Rheological characterization of the semi-solid printing formulations was performed by applying rotational and oscillatory rheometry.

The Hershel-Bulkley equation was used to fit the data obtained in rotational rheometry experiments to gather information about the viscoelastic properties of the printing ink (see Equation 1). This equation can give information on the flow behavior of a given formulation by determining the flow behavior index n (Schwab et al., 2020; Zidan et al., 2019). Values larger than 1 indicate shear-thickening behavior, whereas values lower than 1 represent shear-thinning behavior and n=1 corresponds to Newtonian flow. For this purpose, corresponding to a medium high drug load determined in preliminary investigations, 10 % drug-loaded formulations with varying solvent content were

examined and the consistency index K and flow index n determined by using the Hershel-Bulkley equation (see section 5.2.8.16.2).

For the EVA formulations (see Figure 7), the Hershel-Bulkley equation gave a good approximation of the flow curve (see R^2 values in Table 4).

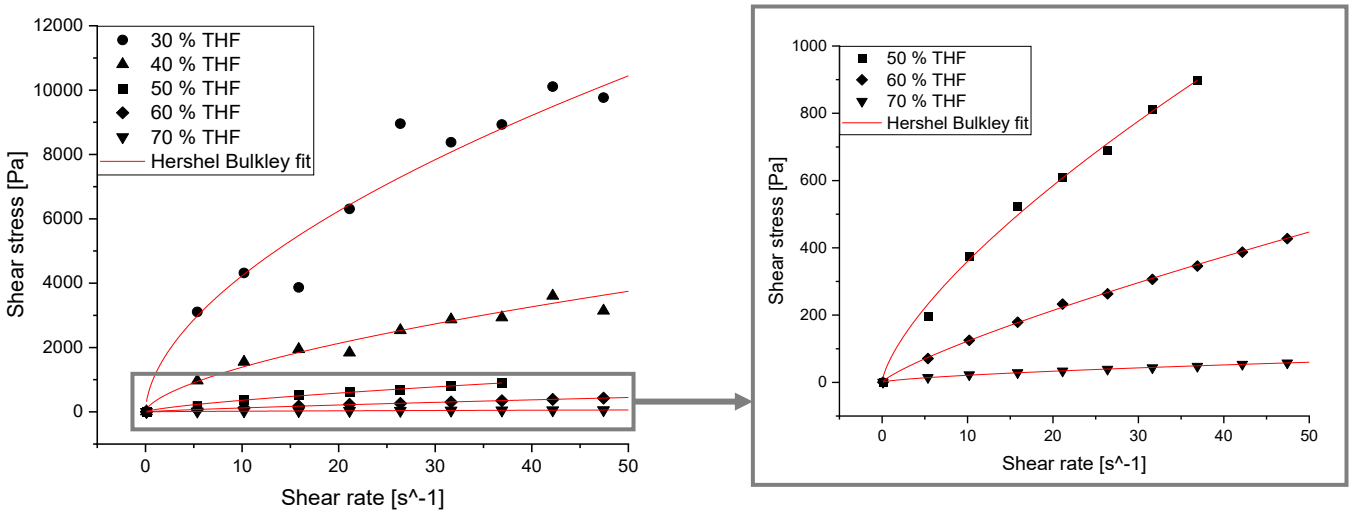

Figure 7. Experimental data and Hershel-Bulkley fit obtained during rotational rheometry experiments for EVA formulations with 30-70 % solvent content. Left graph representing an overview of all experiments and right graph representing an enlarged section for solvent contents above 50 % THF.

The values for the flow behavior index n are below 1 in all cases indicating a shear thinning behavior, as expected for polymer solutions. Since the formulations were liquid-like and did not display a yield point, τ_0 could not be determined reliably. This suggests that the formulation will start to flow even under little to no applied pressure and should flow from the needle tip of the printing syringe easily depending on the diameter of the orifice. The formulation that was considered most suitable for printing and easy to handle with the setup of the Bioplotter, was the 50 % THF containing formulation, to which the API was added. This formulation had a flow behavior index n of 0.67 and a consistency index K of 80.57 (see Table 4).

Table 4. Results for flow behavior index n, flow consistency index K and R2 values obtained via Hershel Bulkley fit for EVA and PCL formulations containing different solvent contents. Mean ± sd; n=3.

		30 % THF	40 % THF	50 % THF	60 % THF	70 % THF
EVA	n	0.56 ± 0.06	0.65 ± 0.02	0.67 ± 0.04	0.78 ± 0.03	0.78± 0.08
	K	1160.65 ±37.27	287.09 ± 20.10	80.57 ± 17.99	19.57 ± 3.30	4.27 ± 0.14
	R^2	0.9465	0.9315	0.9907	0.9987	0.9974
PCL	n	0.71 ± 0.07	0.72 ± 0.04	0.82 ± 0.03	-	-
	K	272.56 ± 19.75	111.33 ± 12.43	26.90 ± 4.10	-	-
	R^2	0.9942	0.9950	0.9983	-	-

For the PCL formulations, it was not feasible to perform measurements with the same setup beyond a solvent content of 50 %, as the formulation became too liquid and flowed out of the gap of the rheometer. The fit with the Hershel-Bulkley equation also in this case showed good correlation with the experimentally obtained values (see Figure 8).

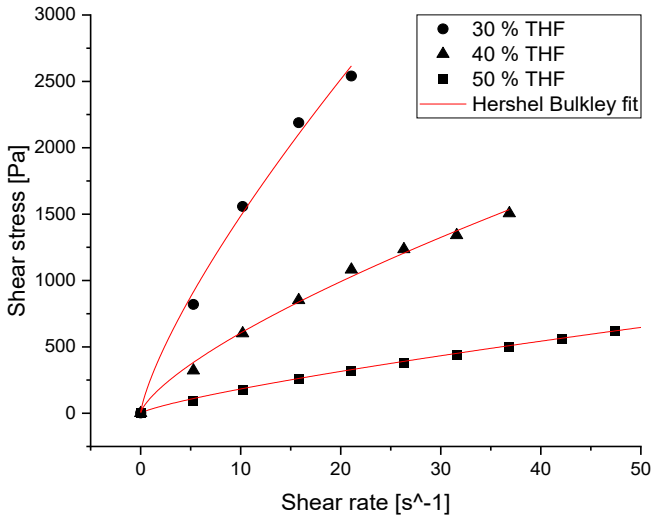

Figure 8. Experimental data and Hershel-Bulkley fit obtained during rotational rheometry experiments for PCL formulations with 30-50 % solvent content.

These formulations displayed shear-thinning behavior with no clear yield flow point as well. The most suitable formulation for 3D-printing determined in pre-trials was the 40 % THF containing PCL-formulation with added API. Their flow behavior index n and consistency index K were found to be in similar magnitude of the most suitable EVA formulation (0.72 and 111.33 respectively, see Table 4).

3.1.3.1.2 Creep test

The creep test can be performed to assess how a printing ink will respond to shearing inside of the printhead of the Bioplotter and determine the required time until structural integrity is regained. It can be helpful to determine whether material will recover sufficiently after printing to retain its shape until the material is solidified.

The two polymers EVA and PCL were formulated into printable inks and subjected to high shear intervals of the duration of one printing cycle, followed by a low shear interval to allow the formulations to recover (see section 5.2.8.16.2).

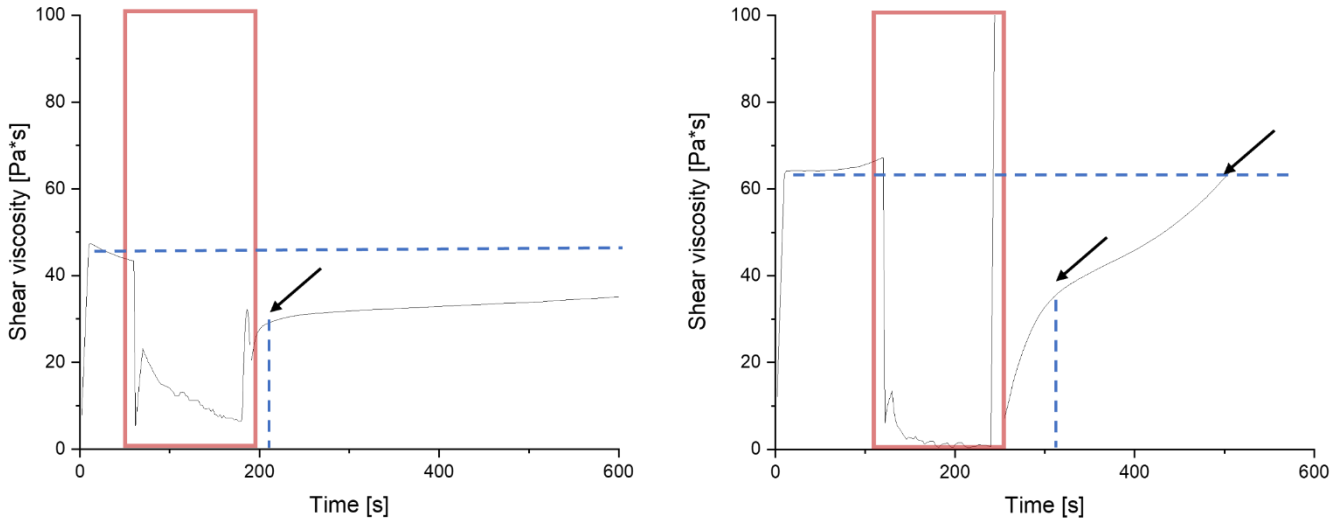

Figure 9. Results of creep test plotted as shear viscosity against time for EVA (left) and PCL (right) formulations. Dashed lines indicate initially measured viscosity during low shearing; red boxes indicating interval of high shear corresponding to applied stress during printing and arrows indicating recovered viscosity shortly after high shear interval and time point at which initial viscosity value was reached again (only observed for PCL).

In case of EVA, the formulation regained approximately 66% of its starting viscosity after only 30 seconds which was enough to allow strands to be printed without flowing apart or completely flowing together with the next layer printed onto the previous one (see Figure 9, left). Full recovery, however, was not observed even after 10 min. In case of the PCL formulation, the shear viscosity was higher in the beginning compared to the EVA formulation and could fully be recovered after approximately 4.5 min (see Figure 9, right). Also here, a steep rise in the viscosity curve was observed after the high shear interval, during which 55 % of the original viscosity value was reached after 75 s. This time was sufficient to allow printing of the formulation with high shape fidelity of the printed strands. Both formulations were able to regain sufficient structural integrity to facilitate printing multiple layers of the formulations. This indicates that these formulations are able to withstand high shear rates occurring during the printing process while maintaining a high enough viscosity after printing to avoid loss of shape fidelity. It further showed that the viscosity was reduced during printing and can be considered low enough to facilitate easy flow through the needle tip mounted to the printing cartridge.

3.1.3.2 Oscillatory rheometry

Since the formulations were determined to be shear-thinning as shown in rotational rheometry experiments, the viscosity during printing is not constant and cannot be readily determined.

Oscillatory rheometry offers the advantage of performing measurements in the linear viscoelastic (LVE) region of a sample, in which its structure is not destroyed. While the viscosity during printing cannot readily be determined in this setup either, it does allow determination of certain rheological parameters and can be used to draw comparative conclusions.

For instance, the loss factor tan δ, which is the quotient of the loss modulus G'' and the storage modulus G' can be used to determine whether the properties of a formulation are more in line with those of an ideally viscous (tan δ > 100) or ideally elastic (tan δ < 0.01) formulation. Further, the phase angle may be determined which can help classify a given formulation as more liquid- (phase angles between 45-90°) or more solid and gel- (phase angles between 0-45°) like. Generally, a high G' would be preferred for good shape retention and a low yield stress for easy extrusion.

For this investigation, the 10 % drug-loaded EVA and PCL formulations with various solvent contents as described in section 3.1.3.1.1 were subjected to oscillatory measurements (see section 5.2.8.16.3). For both the EVA and PCL formulations, the determined phase angles indicated a liquid-like behavior for all investigated solvent contents (see Table 5). This could also be confirmed by plotting the shear moduli against the complex shear strain. In all cases for both polymers the curve of the loss modulus G'' was located above the curve of the storage modulus G' (Figure 10 and Figure 11).

Table 5. Results for phase angle, tan δ, and complex component of shear viscosity obtained for EVA and PCL formulations during oscillatory rheometry experiments. Values measured at 0.1 % complex shear strain.

		30 % THF	40 % THF	50 % THF	60 % THF	70 % THF
EVA	Phase angle [°]	65	77	85.2	65	56
	tan δ	2.2	4.6	13.6	2.2	1.5
	Shear viscosity (complex component)	699.4	175	40.6	28.1	48.1
PCL	Phase angle [°]	86.6	86.8	85.2	-	-
	tan δ	16.5	18.2	11.8	-	-
	Shear viscosity (complex component)	102.4	60.4	17.7	-	-

For EVA the G' and G'' curves for the formulations with 30 - 50 % solvent content displayed a wide LVE region. Formulations with higher solvent contents showed a decline in both curves after approximately 0.1 % complex shear strain (see Figure 10, bottom row) and a LVE region could not be determined. This was possibly observed because these formulations were already liquid and minimal agitation already caused the structure of the respective sample to be irreversibly destroyed.

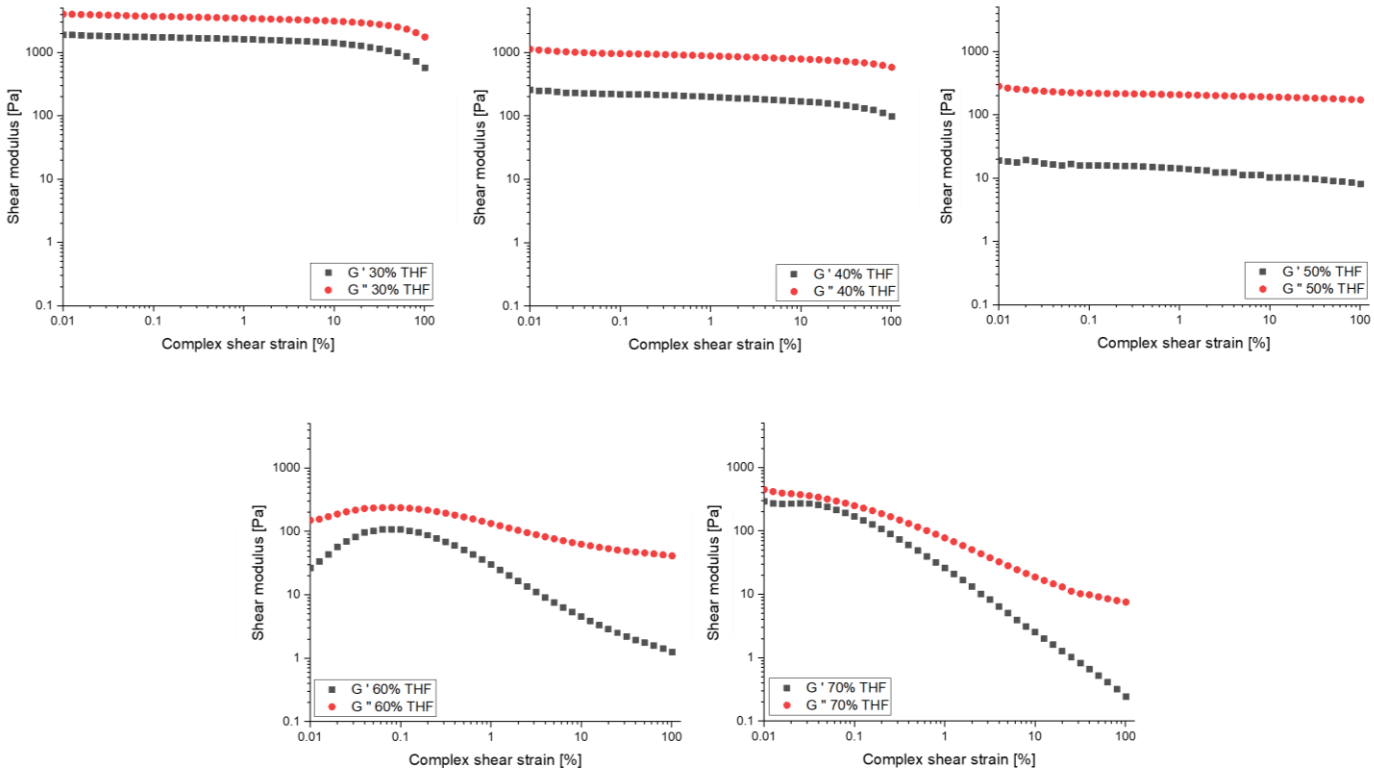

Figure 10. Storage modulus G' and loss modulus G" plotted as shear modulus plotted against complex shear strain for EVA formulations with 30-70 % solvent content (n=1). Measured at a frequency of 1 Hz.

For the PCL formulations, this was also observed for the higher solvent content (50 % THF, see Figure 11, right). However, here the curve for the loss modulus G'' remained nearly linear. Also here, structural integrity of the sample seemed to be lost and declined after approximately 0.1 - 0.2 % complex shear strain corresponding to a more liquid sample.

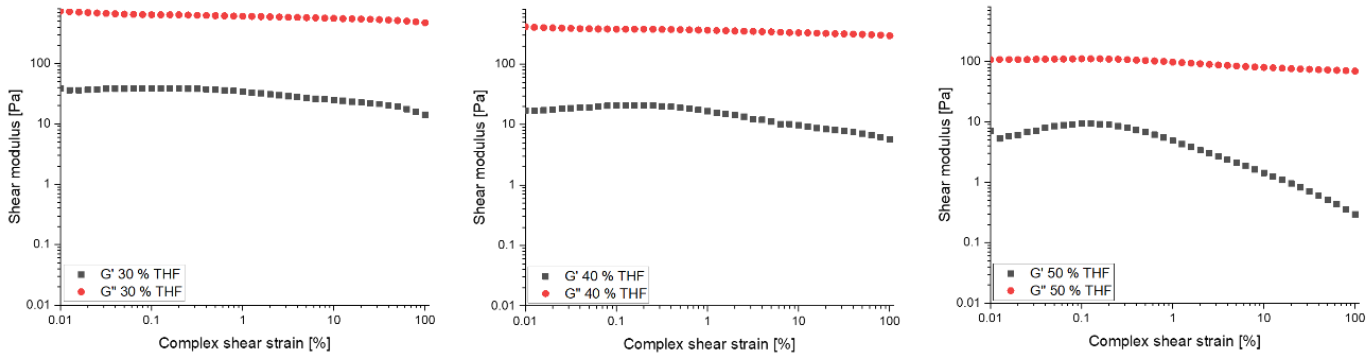

Figure 11. Storage modulus G' and loss modulus G" plotted as shear modulus plotted against complex shear strain for PCL formulations with 30-50 % solvent content (n=1). Measured at a frequency of 1 Hz.

The formulations that were considered to be most suitable for 3D-printing, show values of similar magnitude for their respective shear viscosity. For EVA, this refers to a value of 40.6 and for PCL to a value of 60.4 (see Table 5). While these values cannot serve as a harsh cut-off beyond which printing no longer is feasible, they may serve as an indicator for evaluation of printability.

In an additional experiment, the most suitable formulations (50 % THF content for EVA and 40 % THF content for PCL) were selected and formulated with different APIs. The LC-HCl amount was hereby substituted by the same amount of TrCl or HCT and the oscillatory measurements were repeated.

Figure 12 shows an overview of the resulting plots. In all cases a LVE region could be determined and the phase angle, loss factor and shear viscosity were determined at 0.1 % complex shear strain within this region.

A: EVA

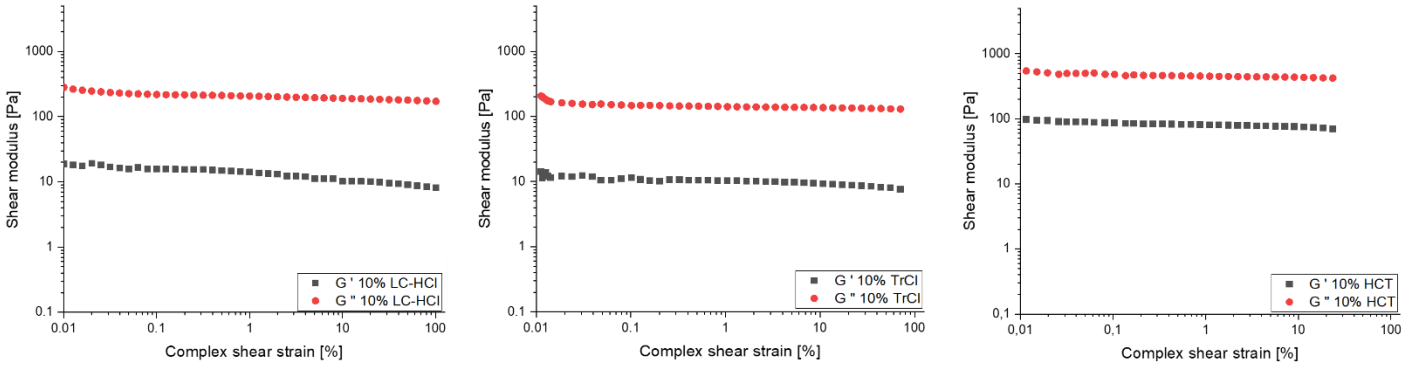

B: PCL

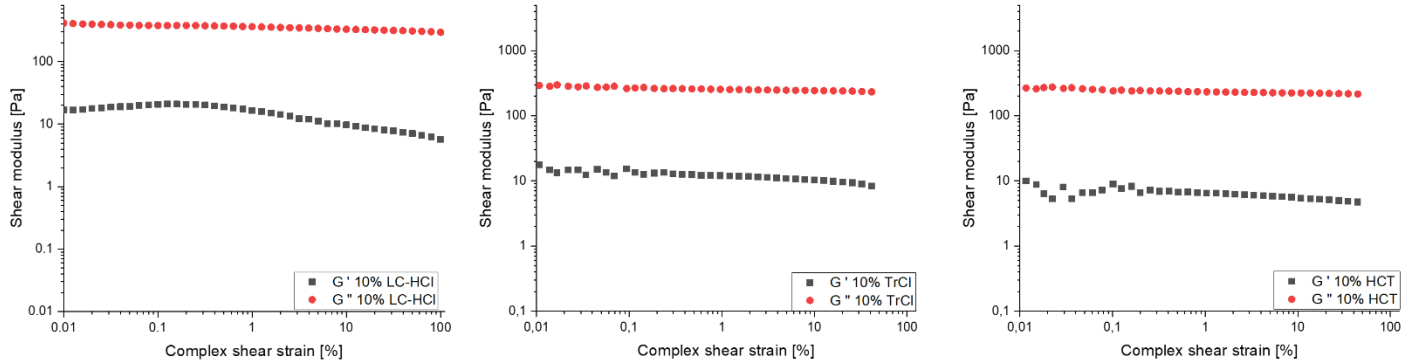

Figure 12. Storage modulus G' and loss modulus G" plotted as shear modulus plotted against complex shear strain for EVA (A, top) and PCL formulations (B, bottom) with three different APIs (formulations include 10 % [w/w] of LC-HCl: lidocaine hydrochloride, TrCl: trospium chloride or HCT: hydrochlorothiazide) (n=1).

For all formulations a liquid-like consistency was found by evaluating the phase angle. All obtained values for the loss factors were larger than 1 and suggested a higher viscous component in the formulations, that was also visible in the curves for the loss modulus G'' which were located above the ones for the storage modulus G'. The window of shear viscosity that is posed by the printable EVA formulations with different APIs reaches from 33 to 75 (see Table 6). For PCL, this window extends from 43 to 60 and lies within similar magnitude. This confirms that printable formulations seem to exhibit similar rheological behavior in the LVE regions determined with the applied setup and the complex shear viscosity may serve as an indicator for printable formulations.

Table 6. Results for phase angle, tan δ, and complex component of shear viscosity obtained for drug loaded EVA and PCL formulations during oscillatory rheometry measurements. Values obtained at 0.1 % complex shear strain.

		LC-HCl	TrCl	HCT
EVA	Phase angle [°]	85.2	86	79.5
	tan δ	13.6	14	5.4
	Shear viscosity (complex component)	40.6	33	75
PCL	Phase angle [°]	86.6	86.5	87.9
	tan δ	18.2	16.5	26.7
	Shear viscosity (complex component)	60.4	46.6	42.5

Nevertheless, these measurements may not replace practical experiments with the 3D-Bioplotter. They may only be used sensibly during early stages of formulation development to roughly assess whether or not a formulation may be printed or should be discarded immediately. This can be beneficial if only less material is available for screening trials, since these measurements only require small samples whereas a printing trial with the Bioplotter will require a much higher material consumption.

3.1.4 Selection of the geometry of the intravesical insert

By using a 3D-printer to manufacture the intravesical inserts, almost any geometry can be manufactured in theory once a suitable drug-loaded substrate has been selected and a suitable printing technology is used.

The simplest geometries would be a cylinder or a sphere. Both have the disadvantage, that they are not readily scalable for intravesical applications, because they are limited in size in order to avoid obstruction of the urethra. This implies that their dimensions would have to be smaller than the diameter of the urethra to prevent clogging and therefore they would also be small enough to be eliminated during voiding. One possible adaptation to overcome this limitation would be to introduce holes into the sphere or cylinder so that urine could still drained. Nevertheless, their dimension is still limited to the diameter of the catheter used for insertion. Especially the cylinder would further require softening of the edges to avoid physical irritation of the mucosa. Considering this aspect, geometries with sharp edges such as cuboids or pyramids are not suitable either. Haupt et al overcame this challenge by manufacturing small rods and connecting them via tubes made from a silk protein to a circular shaped insert (Haupt, 2013).

Another possible geometry is a ring structure. It is readily scalable when keeping the strand diameter small and would not pose any danger to the mucosa or urine drainage. Increasing the strand diameter

would eventually pose a risk for safe application. Its limitation lies therefore in the relatively low amount of API that may be incorporated.

Larger yet simple geometries include slabs or films. Although they could assume relatively large dimensions, if they can be rolled up for insertion, their disadvantage, however, is that they are likely to clog the urethra when the bladder filling level is low. This problem could be overcome by introducing orifices here and creating a net-like structure.

For the present work, the net-geometry was chosen for manufacturing the intravesical inserts because this approach combines the possible advantages of the above-mentioned geometries while allowing safe residence inside of the bladder without clogging the urethra and thus continuously enabling urinal flow. This net-like shape also enlarges the accommodatable mass and surface area through multiple strands in the net and so allowing higher drug loads as opposed to simpler geometries. It is important however, to avoid any areas with a diameter larger than 1.5-2 mm to avoid blockage regardless of the position of the insert within the bladder. Apart from that the surface of the insert should not be sticky upon contact with urine to avoid aggregation after insertion.

Table 7. Different geometries and their suitability for designing an intravesical insert (ranked from least favorable - - to most favorable + +).

Properties / Geometry	Scalability without obstructing urethra	Elimination during voiding	Irritation of mucosa	Max. drug load	Surface area to volume ratio
Cylinder	- -	- -	-	-	-
- Hollow cylinder	-	-	-	- -	+
Sphere	- -	- -	+ +	-	- -
- Hollow sphere	-	-	+ +	- -	-
Cuboid	- -	+	- -	-	-
Pyramid	- -	+	- -	-	-
Drug carriers connected via chain	+ +	+	+ +	+	+/-
Ring	+ +	+ +	+ +	+	+/-
Slab/ Film	- -	+ +	+	- -	+
Net	+ +	+ +	+ +	+ +	+ +

3.1.5 Design of 3D-models

Before the printing process of the inserts can be carried out, computer aided design (CAD) files need to be created. This digital file format refers to the 3D rendering of the object that should be printed. After generating the three-dimensional object, the CAD file needs to be converted into a STL (stereolithography) file. This is the standard file type used for most rapid prototyping systems and is a triangulated representation of a 3D CAD-model.

This triangulation of the surfaces of the object can cause faceting of the model. If the STL file is faceted or coarse, the final model will be, too. This in turn means, that the finer the STL file is generated, the smoother the surface will be. This, however, comes at the expense of large file formats and longer built times attributed to lower layer heights that will be used to print the structure. In the present work, the printed structures consisted only of a low number of layers and therefore, this was not considered a compromise that needed to be made.

The STL file can then be transferred into the slicer software of the 3D-printer that analyzes the model and generates a G-code. This machine code is required to instruct the printer on how to make the object. After completing these steps, the actual printing process can begin.

In the scope of this work, all models were sliced with a layer height of 80 % of the nozzle diameter for optimal printing results. The intravesical drug delivery devices printed in the present work were designed in a net-shape to allow safe residence of the insert inside of the bladder without clogging the urethra (see Figure 13). The diameter of the entire insert was set to 5 cm and the diameters of the printed strands of the inserts were kept below 1.5 mm. This was to ensure that the urethra would not be blocked by the inserted DDD regardless of its position within the bladder.

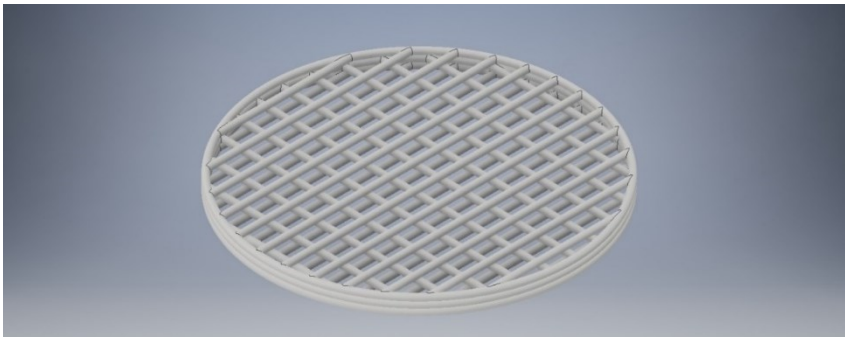

Figure 13. CAD model of intravesical insert.

3.1.6 Printability

3.1.6.1 Strand thickness in relation to speed, pressure and temperature

After evaluating the basic properties and suitability of a given formulation, its printability is of particular interest.

One indicator for printability can be the strand thickness after printing. As demonstrated for a trial PCL-formulation, the strand thickness can significantly vary by altering printing temperature, pressure and speed (see Figure 14).

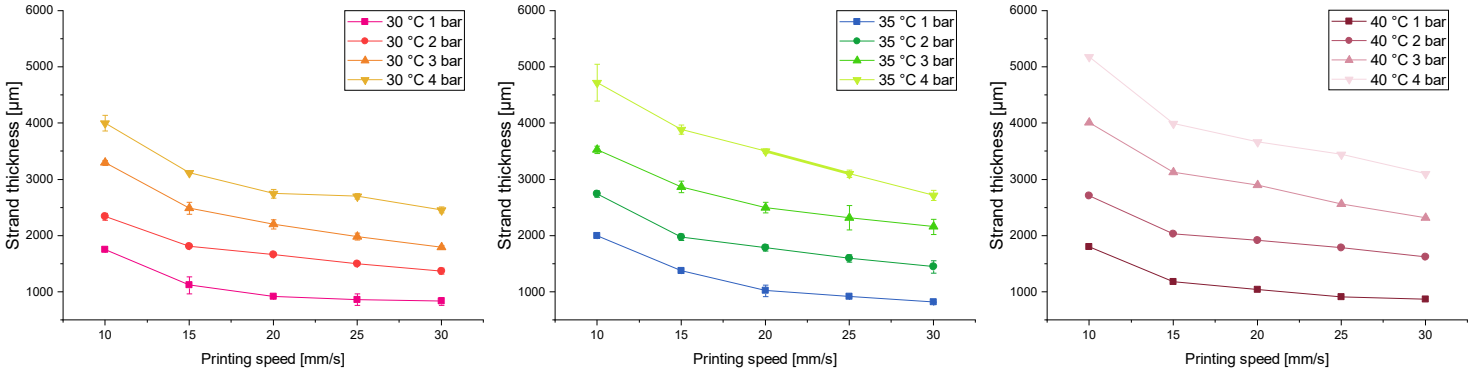

Figure 14. Strand thicknesses of PCL formulation printed under different printing conditions (left to right: 30, 35 and 40 °C printing temperature printed at speeds of 10-30 mm/s and printing pressure of 1-4 bar) after drying; mean ± sd, n=3.

The process parameters should be carefully finetuned depending on the material, in order to achieve a print with high shape fidelity. Too wide strands obtained by over-extrusion can be counteracted by lowering the temperature or pressure or increasing the printing speed. Overly high printing speeds can also lead to low resolution of the printed object when not enough time is given to the strands to adhere to the printbed or previous layer. For the investigated printing temperatures of 30, 35 and 40 °C a nearly linear decrease in strand thickness was observes with increasing printing speed. Below a speed of 15 mm/s a steep increase of strand thickness was observed. As too much material was deposited here, the strands started to flow apart before solidification. Within the same printing speed and pressure, an increase of printing temperature of 5 °C could affect the strand thickness significantly. At a medium printing speed of 20 mm/s and 2 bar printing pressure e.g. the strand thickness was increased by approximately 120-130 µm per 5 °C temperature increase (1661 µm at 30 °C, 1785 µm at 35 °C and 1915 µm at 40 °C). Differences in thickness between temperatures were found to be smallest within the same printing speed at the lowest investigated printing pressure. In this case the extruded amount of material seemed to be affected less by the temperature change possibly because the applied pressure was too low to extrude more material from the needle tip. This experiment demonstrated that within the same formulation, the resolution of the printed object can be varied significantly by adjusting the printing conditions.

Variations between 830 and 5180 µm (30 °C, 1 bar, 30 mm/s and 40 °C, 4 bar and 10 mm/s respectively) were observed corresponding to a more than 6-fold broadening of the strand thickness. It further showed that the different settings of the 3D-printer can counteract each other, and multiple different combinations of settings may lead to the same strand thickness. This could be important, e.g., when the excipients used require processing at a specific printing temperature.

3.1.6.2 Layer-stacking test

An easy way to determine printability during early stages of formulation development on small scale batches is the layer stacking test. In this simple test material is (manually) extruded from a syringe and the ability of the formulation is assessed whether layers can be stacked without losing structural integrity (Paxton et al., 2017).

This approach was used in early trials to quickly narrow down a printable range of formulations without wasting much material and resources (see section 5.2.2). The less merging of strands occurred after stacking them, the more suitable the ink was considered for 3D-printing. When the formulation was extruded from the needle tip in drops and was not able to form a continuous strand, its viscosity was too low and it was not able to generate distinguished layers (see Figure 15 2nd image from left).

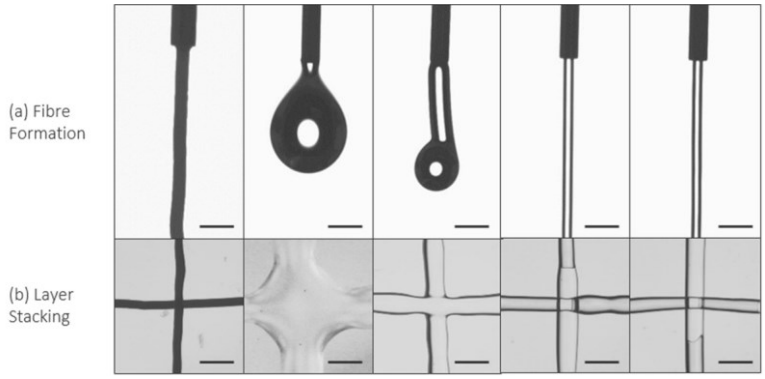

Figure 15. Images of fiber formation after extrusion from needle tip (top row) and layer stacking ability of extruded strands (bottom row) of different printable inks according to (Paxton et al., 2017). Image used under the terms of the Creative Commons Attribution 3.0 license.

For small scale initial suitability experiments, the semi-solid formulations containing polymer, solvent and plasticizer (and later API) were mixed on a heating plate and manually extruded through a 5 ml syringe into net-shapes. By evaluating the resulting structures according to their ability to form continuous strands without merging during drying as well as haptic aspects, it was feasible to identify a suitable drug-free trial formulation for the 3D-printing process. The most promising formulations were then transferred to the 3D-printer for first printing trials. Issues regarding flexibility as well as printability of the semi-solid formulations could be resolved by carefully adjusting the ratios of the

components and critical printing parameters. The viscosity of the semi-solid formulation had hereby the highest impact on determining printability with sufficient shape fidelity of the resulting inserts.

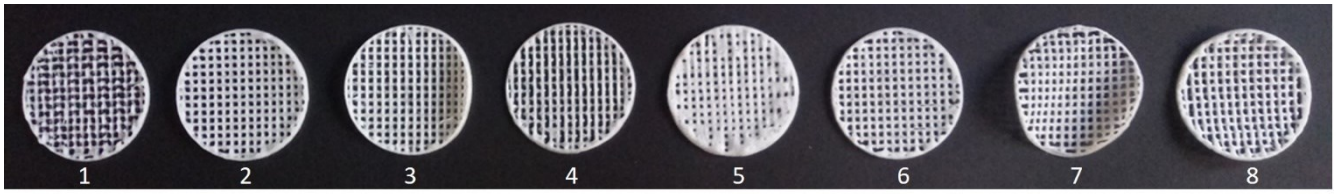

Figure 16. Examples of the effect of different printing parameters for the same formulation containing PCL, DBS and THF. Insert 1 was printed at 0.5 bar with 15 mm/s speed, inserts 2,3 and 4 at 0.8 bar and 15, 17 or 20 mm/s respectively and inserts 5,6 and 7 at 1 bar and 15, 23 or 30 mm/s. All inserts have a diameter of 5 cm.

As mentioned in section 3.1.6.1, a low printing pressure and/or too high printing speed typically led to incomplete strand formation (see exemplarily for PCL Figure 16, inserts no. 1 and 8), whereas excessive pressure and/or insufficient printing speed led to thick strands and confluence (see exemplarily Figure 16, insert no. 5). Therefore, careful adjustment of these parameters was critical for printing the formulations.

3.1.6.3 Printability index

Once the initial screening process was completed and formulations were transferred to the Bioplotter for printing trials, the quality of the print needed to be assessed. Next to visual evaluation, a method was required to objectively evaluate the print result and optimize printing parameters to achieve a high degree of shape fidelity.

Ouyang et al. proposed the printability index for this purpose (Ouyang et al., 2016). They defined printability based on the square shape enclosed by a printed rectangular grid. When the formulation was too liquid, the layers would fuse and enclose a circular area, whereas too viscous formulations would result in irregularly shaped geometries.

The underlying calculations were based on the determination of the circularity of the enclosed area (see Equation 2).

$$C = \frac{4*\pi*A}{L^2}$$ Equation 2

C: Circularity of enclosed area; A: enclosed area; L : perimeter length

The printability Pr was then defined by putting the circularity in relation to a perfect square (see Equation 3). In this case, a perfect square would equal to Pr = 1.

$$Pr = \frac{\pi}{4} * \frac{1}{C} = \frac{L^2}{16*A}$$ Equation 3

Values larger or smaller than 1 would correspond to the degree of deviation from a squared shaped pore enclosed by the printed strands (Pr < 1, low-viscosity ink creates pores of higher circularity due to coalescence and Pr > 1, high-viscosity ink creates highly irregular strands with larger L). This value was used as one quality attribute to determine the quality of the printed object and went into the calculation of the printability score (see section 3.1.6.4).

3.1.6.4 Printability score

Although few proposals have been published on how to determine printability of a given formulations, no parameter was defined, that sufficiently takes multiple quality defining aspects into consideration. Therefore, a new parameter was proposed in this work to combine the different quality attributes into one quantitative parameter. The following equation was proposed for this purpose:

$$P_{score} = |1 - Pr| + \left|1 - \frac{D_{s(measured)}}{D_{s(needle)}}\right| + \frac{D_{s(max)} - D_{s(min)}}{D_{s(mean)}} \qquad \text{Equation 4}$$

P_{score}: printability score; Pr: printability index; $D_{s(measured)}$: measured stand diameter; $D_{s(needle)}$: diameter of applied needle tip; $D_{s(max)}$: maximum strand diameter; $D_{s(min)}$: minimum strand diameter; $D_{s(mean)}$: mean strand diameter

The first term $|1 - Pr|$ describes the geometry by taking into account the shape of the enclosed area and its deviation from the ideal value. The second term $\left|1 - \frac{D_{s(measured)}}{D_{s(needle)}}\right|$ includes the accuracy of the printed object in relation to its design by determining the deviation of the actual strand diameter from its ideal value which equals the needle diameter. This assumes that the extruded strand is formed homogeneously and is not stretched after printing or flows apart after being deposited.

The third term $\frac{D_{s(max)} - D_{s(min)}}{D_{s(mean)}}$ represents the homogeneity of the print by including the variability of the strand diameter throughout a print in relation to its mean.

Since all of the single terms would ideally equal zero, the smaller the determined P_{score} value is, the better the overall quality of the printed object should be.

3.1.6.5 Finding optimal printing settings - Design of Experiments

After collecting some previous knowledge of printing conditions to achieve acceptable results for a given formulation, a next objective was to find optimized printing settings.

For this purpose, a central composite design (CCD) statistical design of experiments (DoE) was selected based on the possibility to resolve quadratic terms in the response surface model. This design consists of four factorial points, four star points and one center point, which is replicated three times. The distance of the star points to the center point was chosen to be 1.414 to allow rotatability.

The investigated responses were strand thickness, relative standard deviation (RSD) of the strand thickness, Pr and P_{score}. 10 % LC-HCl-loaded PCL and EVA formulations were used to perform the experiments. The design space was chosen according to previous experience with the formulations. Table 8 and Figure 17 show the results of the CCD for the PCL formulation.

Table 8. Uncoded factors and results for responses of central composite design for the PCL formulation. Values for printability index (*Pr*) and strand thickness given as mean of 20 measurements.

Factors		Responses			
Printing pressure	Printing speed	Pr	Strand thickness	RSD Strand thickness	P_{score}
0.8	15	0.87	813.07	34.57	1.33
1.8	15	1.02	2025.80	9.04	1.52
0.8	25	0.96	689.07	48.63	1.95
1.8	25	0.97	1346.00	4.00	0.67
0.6	20	0.92	711.80	61.73	2.26
2	20	1.00	1741.69	6.96	1.23
1.3	13	0.98	1499.20	8.72	1.04
1.3	27	0.96	866.38	41.74	1.50
1.3	20	0.98	1151.13	5.15	0.49
1.3	20	0.99	1157.19	4.61	0.46
1.3	20	1.00	1161.07	4.34	0.46

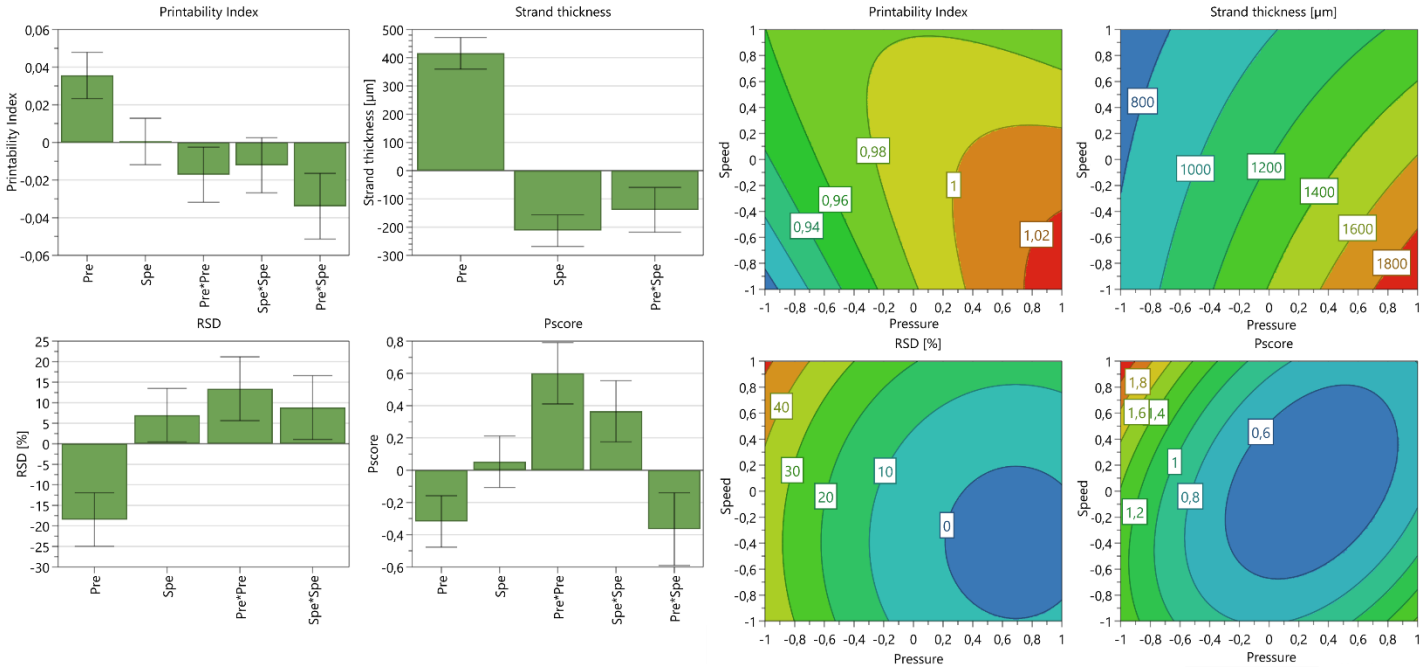

Figure 17. Coefficient (left) and contour (right) plots displaying the effects on printability index, strand thickness, relative standard deviation (RSD) of strand thickness and printability score (Pscore) for PCL formulation. Error bars in coefficient plot indicate 95% confidence interval (R2: Printability index: 0.95, Strand thickness: 0.98, RSD: 0.93, Pscore: 0.96; Q2: Printability index: 0.66, Strand thickness: 0.93, RSD: 0.69, Pscore: 0.77).

It can be seen that the printing pressure had the highest effect on the investigated responses. The effect was found to be non-linear for the printability index, RSD of strand thickness and P_{score} value.

In all cases good models were obtained with high R^2 values and Q^2 values above 0.66. Increasing printing pressure at constant speed led to higher values for the printability index. This effect however decreases with increasing speed (see Figure 17, right). This implies that at low printing speed, the quality of the print can be improved by adjusting the pressure to a certain extent but cannot be further increased at high speeds. When the speed is set too high, not enough time might be given for the material to set and adhere to the printing surface or previous layer, so that the quality of the print will be reduced. Increasing the speed at constant pressure, however, only had a larger influence on the printability index at low printing pressures and did not compensate the effect of printing pressure at medium to high pressure settings. For the strand thickness, as expected, increased printing pressure and reduced printing speed led to thicker strands. Here also the printing pressure had the higher impact on the strand thickness compared to the printing speed. The RSD of the strand thickness showed significant effects also for the quadratic terms of pressure and speed indicating non-linear relations. The response surface plot shows an optimal region of settings to be applied for RSD values around zero at high printing pressure and low printing speed. During these settings, the material was extruded from the syringe homogeneously and the formulation had sufficient time to adhere to the below layer. This resulted in less variability of strand diameter. It must be kept in mind, however, that these settings will also lead to rather wide strands, which may not be favorable. The printability score also gave an optimal region for a value of 0.6 within the investigated process window at medium to high printing pressure and speed. The effect of speed was only significant in its quadratic term and could be varied in a larger region to obtain the same printability score.

In Figure 18 a visual representation of the results of the CCD for the printability score is given.

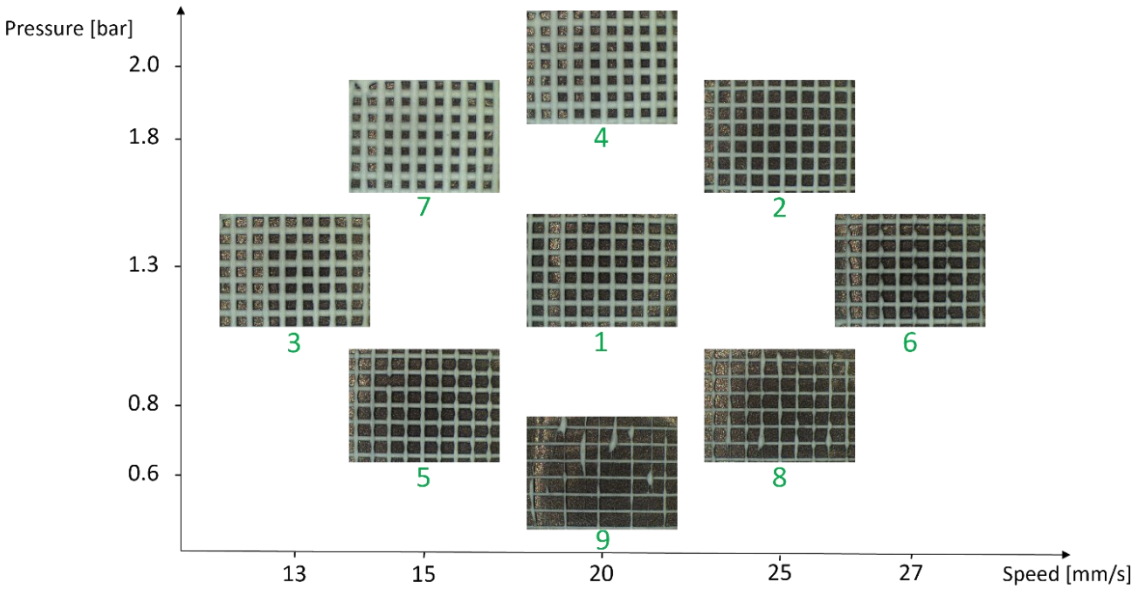

Figure 18. Visual representation of the results of the experimental runs of the central composite design for the printability score obtained for the printed PCL formulation. Ranking from smallest to largest P_{score} value.

The quality of the printed grid structures varied largely depending on the respective printing settings. The corresponding values of the printability score allow an objective ranking of these results that is in good agreement with a subjective order one may apply. For this quality attribute a cut-off value should be applied that deems the obtained print acceptable. This must be decided individually and in agreement with the functionality of the printed object. For instance, a comparably low resolution may be acceptable when immediate release dosage forms are printed that do not exhibit complex release profiles. In this case it would be of greater importance that the deposited mass is homogeneous and the process reproducible. However, when sustained release dosage forms are manufactured, the strand diameter and its geometry are of greater importance when diffusion pathways within the matrix of the strands influence the release behavior. In the present example, a cut-off value for the given PCL-formulation was defined at 1.04, rendering inserts no 1, 2 and 3 acceptable, whereas insert 4 was already inacceptable due to too wide strand diameters (corresponding to a P_{score} value of 1.23).

These results demonstrate that the CCD was useful to determine optimal process settings in respect to the investigated responses and the P_{score} value can be used to objectively classify the quality of the printed objects.

The experiment was repeated with another formulation to determine whether the model is valid also for other systems. For this purpose, a 10% drug-loaded EVA formulation was prepared. The results are summarized in Table 9 and Figure 19.

Table 9. Uncoded factors and results for responses of central composite design for the EVA formulation. Values for printability index (*Pr*) and strand thickness given as mean of 20 measurements.

Factors		Responses			
Printing pressure	Printing speed	Pr	Strand thickness	RSD Strand thickness	P_{score}
0.5	15	0.95	867.71	42.59	1.49
1.5	15	1.08	2599.47	28.40	2.89
0.5	25	0.95	527.94	51.79	2.27
1.5	25	1.04	1905.82	9.73	1.57
0.3	20	1.07	299.94	68.17	2.94
1.7	20	1.09	1783.88	31.82	2.27
1	13	1.03	1769.29	30.24	2.04
1	27	0.99	1270.65	18.18	0.98
1	20	0.98	1393.29	7.54	0.86
1	20	1.00	1390.36	7.07	0.80
1	20	0.99	1398.09	7.16	0.81

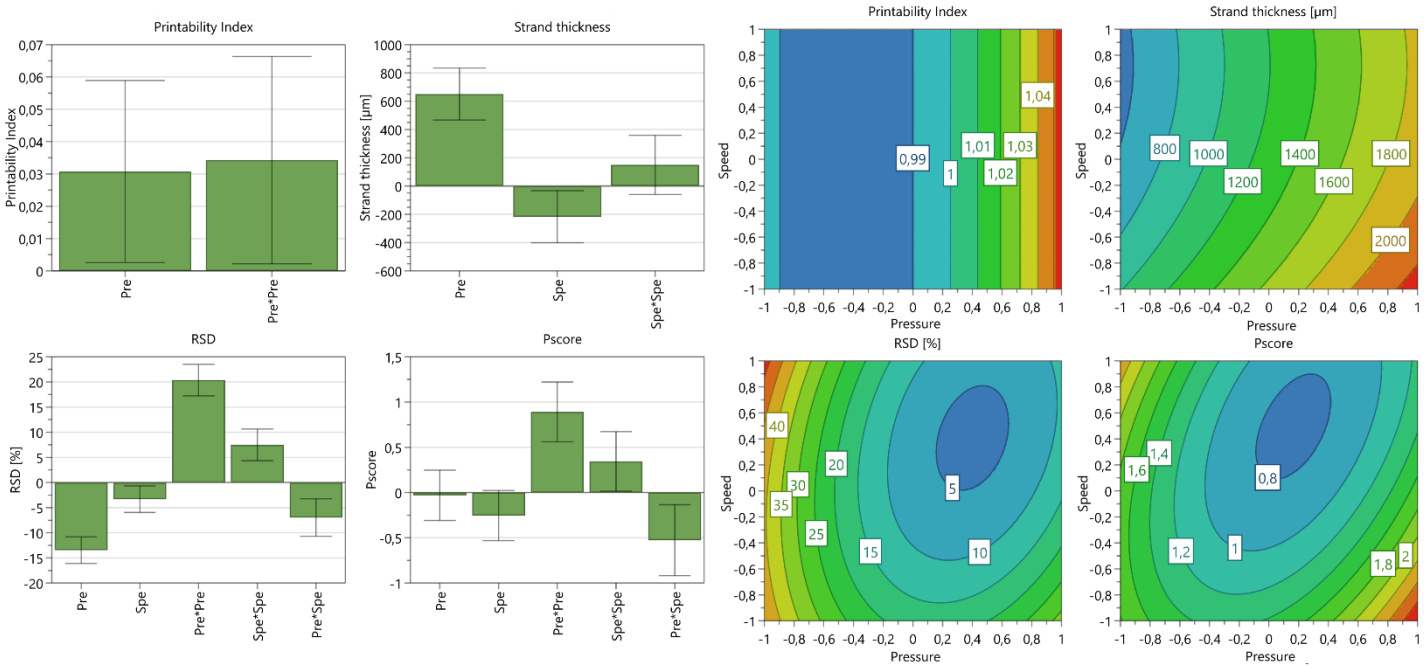

Figure 19. Coefficient (left) and contour (right) plots displaying the effects on printability index, strand thickness, relative standard deviation (RSD) of strand thickness and printability score (Pscore) for EVA formulation. Error bars in coefficient plot indicate 95% confidence interval (R2: Printability index: 0.61, Strand thickness: 0.92, RSD: 0.99, Pscore: 0.93; Q2: Printability index: -0.28, Strand thickness: 0.78, RSD: 0.93, Pscore: 0.50).

In this case, the printability index seemed to be influenced only by the pressure. However, here only a poor model was obtained, since the goodness of prediction was very low (Q^2: -0.28, R^2:0.61). This model showed that at a given pressure, the printing speed had no influence on the printability index (see Figure 19, right). Better models were obtained for the other responses with R^2 values above 0.92 and Q^2 values above 0.5. For strand thickness and RSD of strand thickness also here a high influence of the printing pressure compared to the printing speed was detected. For the strand thickness no significant non-linear relation was observed, whereas for the RSD, both speed and pressure displayed non-linear relations. The strand thickness at constant speed was shown to increase with increasing pressure. At constant pressure, the strand thickness slightly decreased with increasing speed for low to medium high speeds. Above a certain speed threshold (approx. 24 mm/s) the strand diameter slightly increased again, possibly due to incomplete adherence of the strands to the underlying surface resulting in overcompensation of the effect of the pressure. In the response contour plots regions of low RSD and P_{score} values were observed for medium to high pressure and speed indicating that high resolution prints were obtained with low variability. The viscosity of this formulation during printing was rather low so that higher speeds were required to avoid over-extrusion of material.

The visual representation of the results of this CCD in Figure 20 shows that for this formulation the variability of the shape fidelity for the investigated design space was much higher as seen for the PCL formulation and more inserts were printed with very poor resolution (see e.g. inserts 6, 7, 8 and 9). This indicates that the process window for this formulation appears much smaller and the formulation

responds sensitively to changed settings. This can also be seen in the response surface plots in which the optimal regions are much smaller and the best obtained values for RSD and P_{score} are overall higher than for the PCL formulation.

However, also in this case the P_{score} value allowed a ranking of the quality of the printed inserts that is in good agreement with the visual classification one might apply.

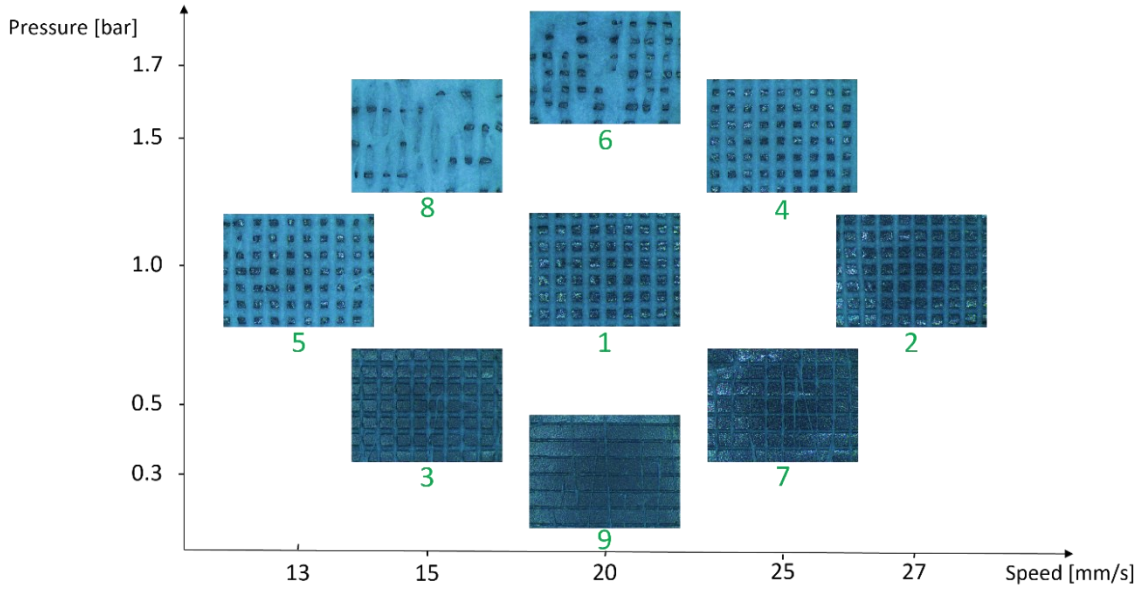

Figure 20. Visual representation of the results of the experimental runs of the central composite design for the printability score obtained for the printed EVA formulation. Ranking from smallest to largest P_{score} value.

In this case, a cut-off value at a P_{score} of 0.98 was be applied which renders inserts 1 and 2 acceptable. Insert 3 (P_{score} value of 1.49) would be classified inacceptable due to incomplete formation of strands. The printing settings applied to obtain these inserts are in agreement with the process windows found via the CCD. This cutoff value obtained for the EVA formulation was found to be in similar magnitude as the cutoff value applied for the PCL formulation.

It would be interesting to apply this approach to more formulations in the future to gather more knowledge of cut-off values for different kind of formulations with different viscoelastic properties.

3.1.7 Post-processing/ Drying

3.1.7.1 Drying kinetics and porosity

After examination of the formulations and the 3D-printing process itself, evaluation of post-processing concludes the last step towards broader process understanding. Since the feedstock material for the 3D-printer is semi-solid, solidification after printing plays an important role in manufacturing of the inserts. Solidification in this case takes place by solvent evaporation. This process can be sped up by increasing the drying temperature or reduction of the surrounding pressure by using a vacuum dryer.

These drying conditions and their effect on the insert properties were investigated by subjecting the printed inserts to different drying conditions from 30 - 40 °C under atmospheric or reduced pressure (500 mbar). Drying kinetics were evaluated by determining how fast the mass of the inserts was reduced for the respective temperature and pressure combination.

Figure 21 shows the exponential mass reduction of the printed inserts under different drying conditions.

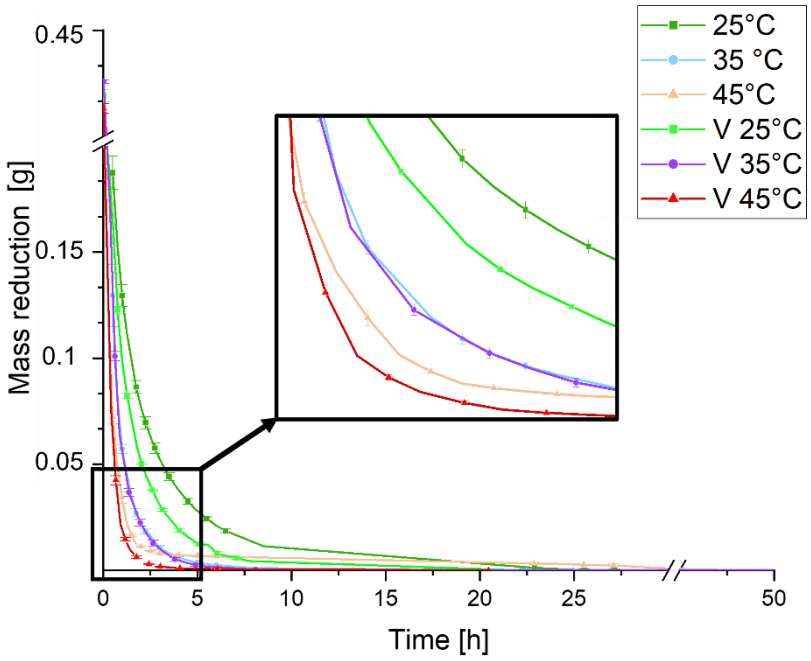

Figure 21. Mass reduction of the printed inserts under different drying conditions (V: vacuum dryer), mean ± sd, n=3.

As expected, drying occurred faster when the temperature was elevated, or the pressure reduced. In the beginning this happened fast due to the large surface area of the insert caused by its net-structure and high amounts of solvent located on the surface. Drying then slowed down because the solvent had to evaporate from inside the insert. Within the pores that form inside the inserts, different capillary pressures can cause the solvent to be more or less eager to be removed from the pore depending on its size and curvature. The vapor pressure of the solvent hereby reduces with reduced pore diameter. Under reduced pressure, the boiling point of a solvent is lowered, and the vapor pressure is elevated, which explains the faster solvent evaporation. However, for the inserts dried at 35 °C this was not observed. This may have occurred due to formation of differently sized and curved pores under these drying conditions.

When evaluating the respective SEM images of the dried inserts, it became apparent that they in fact had differently sized pores according to the drying conditions that were applied (see Figure 22).

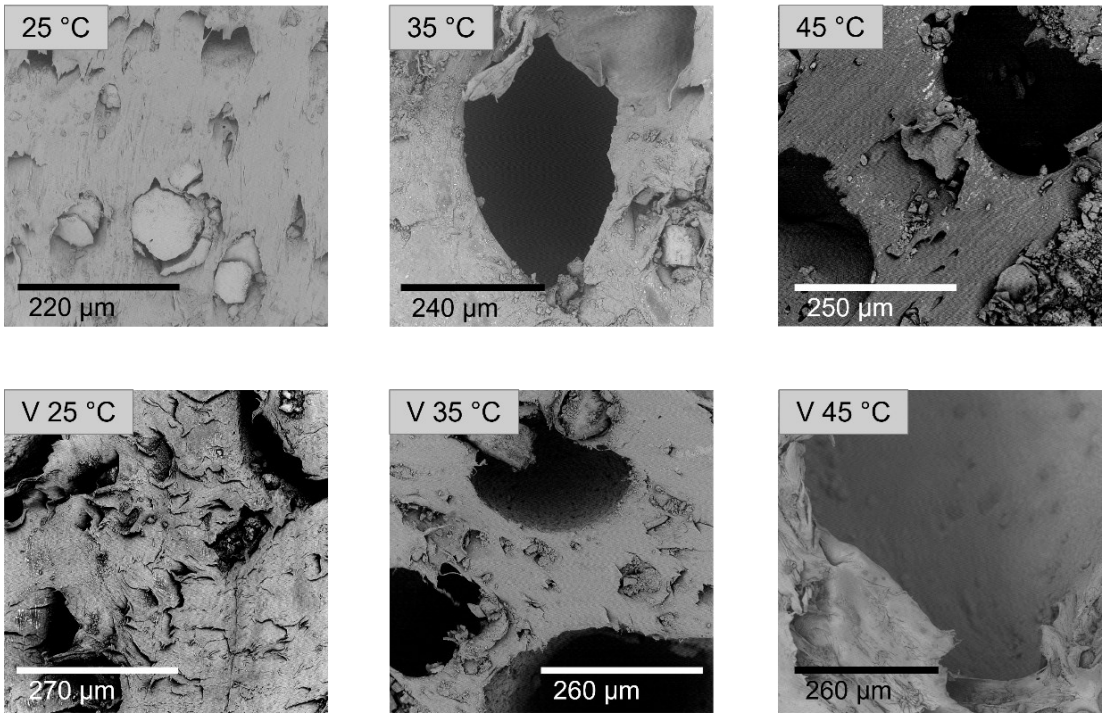

Figure 22. SEM images of PCL-inserts dried under different drying conditions. Top row: atmospheric pressure, bottom row: reduced pressure (V: vacuum dryer at 500 mbar).

The largest pores seemed to be obtained under reduced pressure at 45 °C (Figure 22, bottom right), whereas the smallest pores were visible for the inserts dried at 25 °C under atmospheric pressure (Figure 22, top left). This was possibly caused by slower and gentler drying. This could have given the matrix more time to release the solvent and close its pores by confluence of the still soft and more mobile matrix after the gas bubble of the solvent was released from the insert. This would leave behind only small pores compared to faster drying under higher temperature or reduced pressure. Here, the solvent could expand within the matrix and cause formation of larger pores as the matrix solidified around it. For the inserts dried at 35 °C both inserts showed comparable pore sizes, which would be in accordance with the observation of mass reduction during drying. However, SEM images only allow analysis of small areas of the insert and should be interpreted with caution.

To confirm these findings, µCT-measurements were performed to visualize the internal structure throughout the entire insert. These images revealed big differences in the internal porosity of the inserts (Figure 23).

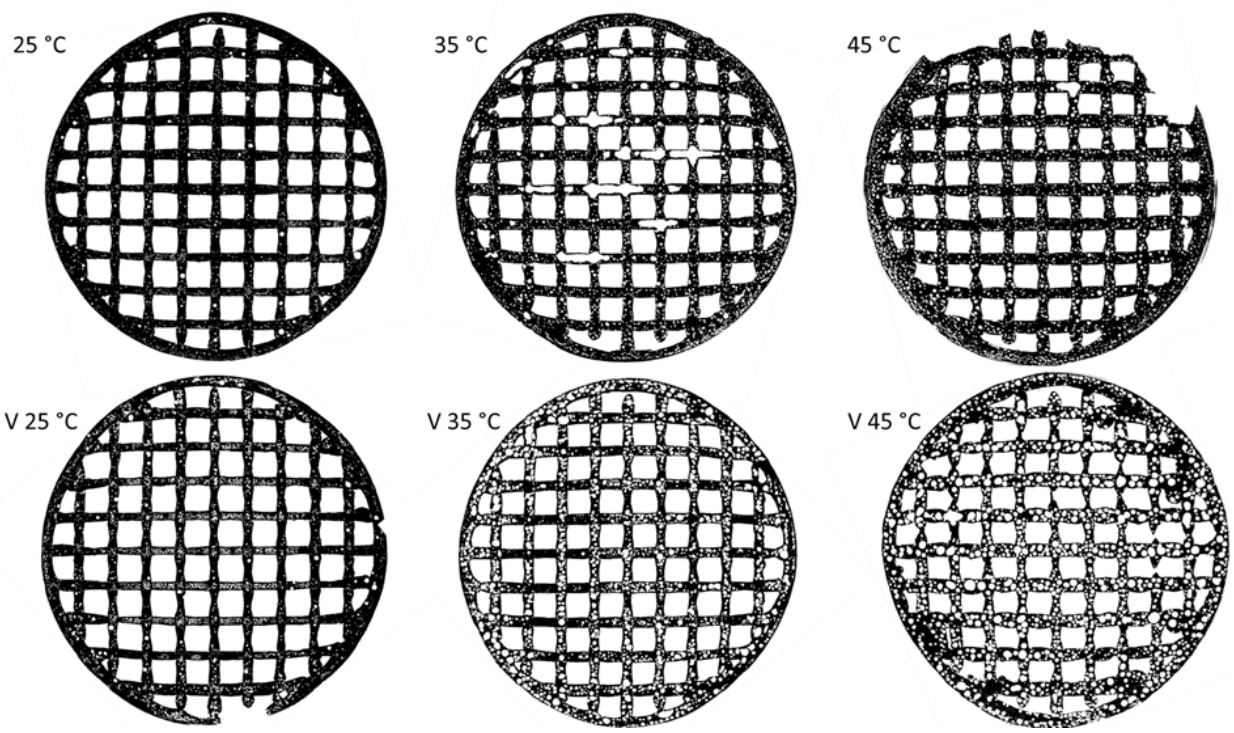

Figure 23. µCT images of PCL-inserts dried under different drying conditions. Top row: atmospheric pressure, bottom row: reduced pressure (V: vacuum dryer at 500 mbar). Incomplete sections in images taken at 45 °C and V 25 °C due to positioning of the insert in sample holder during measurement.

As seen for the SEM images, also here the smallest pores were observed for the insert dried under atmospheric pressure and 25 °C and the largest pores under reduced pressure and 45 °C. It became apparent that the pores seemed to become larger with increasing temperature and reduced pressure, but the insert dried at 35 °C under atmospheric pressure seemed to present an exception here. In this case, formation of few very large pores was observed in the middle of some strands that were not seen in this magnitude for any other drying condition (see Figure 23, top center). One hypothesis for this occurrence may be that under this specific drying condition the matrix of the insert was still liquid enough so that gas bubbles were able to confluence to larger bubbles inside some of the strands before solidification took place.

3.1.7.2 Strand thickness and aspect ratio of printed strands

Apart from the porosity, the different drying conditions also influenced the diameter of the inserts, as well as the measured strand thickness and roundness of the strands in their cross-section.

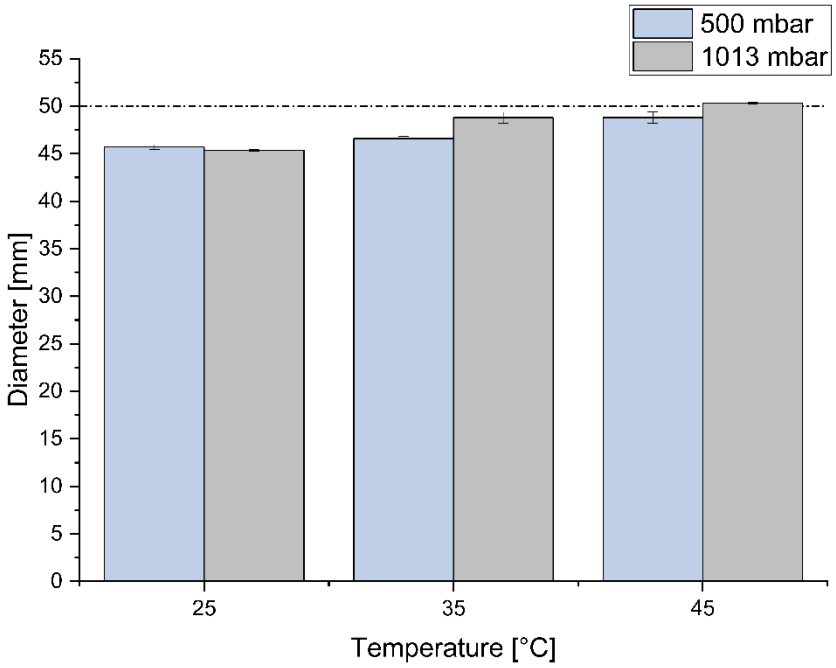

Figure 24. Diameters of PCL-inserts dried under atmospheric and reduced pressure at different temperatures. Dashed horizontal line indicates diameter according to CAD-design of the inserts; mean ± sd, n=6.

Shrinkage of the inserts was most pronounced at 25 °C and increased with temperature and decreased pressure (see Figure 24). Similarly, the strand diameter was also larger at higher drying temperatures but did not differ significantly under different pressure conditions (see Figure 25, left).

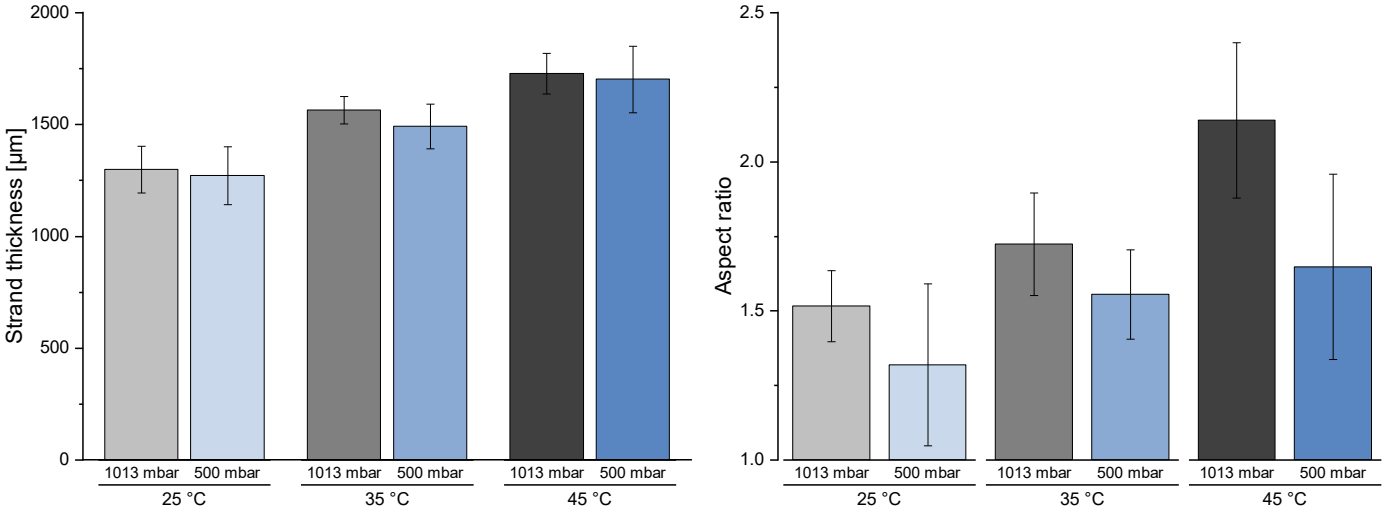

Figure 25. Strand thickness (left) and aspect ratio (right) measured for PCL inserts dried under different drying conditions. Strand thickness given as mean ± sd (n=10) and aspect ratio as mean ± sd (n=6).

The roundness of the strands expressed as the aspect ratio of the cross-section was found to be increased with decreasing pressure and lower temperature.

The nearly linear relationship between stand thickness and drying temperature was possibly caused by higher temperatures leading to the lower viscosity of the printed formulation and consequently

strands flowing apart more. Further, the observed porosity seen in the SEM and µCT images within the strands also caused larger strand diameters due to expansion of the strands.

The rounder strands obtained under reduced pressure could have been caused due to expansion of the solvent gas nearly uniformly in all directions across the strand's cross-section and fast solidification of the matrix.

3.1.7.3 Dissolution testing

As described in the literature, the porosity of a drug delivery device can influence the drug release. This was shown in an adaption of the Higuchi equation (Higuchi, 1963a):

$$Q = \sqrt{\left(\frac{D\partial}{\tau}\right)(2C - \delta C_S)\, C_S t} \qquad \text{Equation 5}$$

Q: at time t released amount of API; D: diffusivity of the API in permeating fluid, C: initial concentration in the polymeric matrix; C_S : saturation solubility in matrix; ∂: porosity; τ : tortuosity of matrix (=dimensions of radius and branching of pores and canals in matrix)

This equation suggests that with increasing porosity the drug release will be enhanced as well. As shown in the corresponding release curves, this was also the case (see Figure 26).

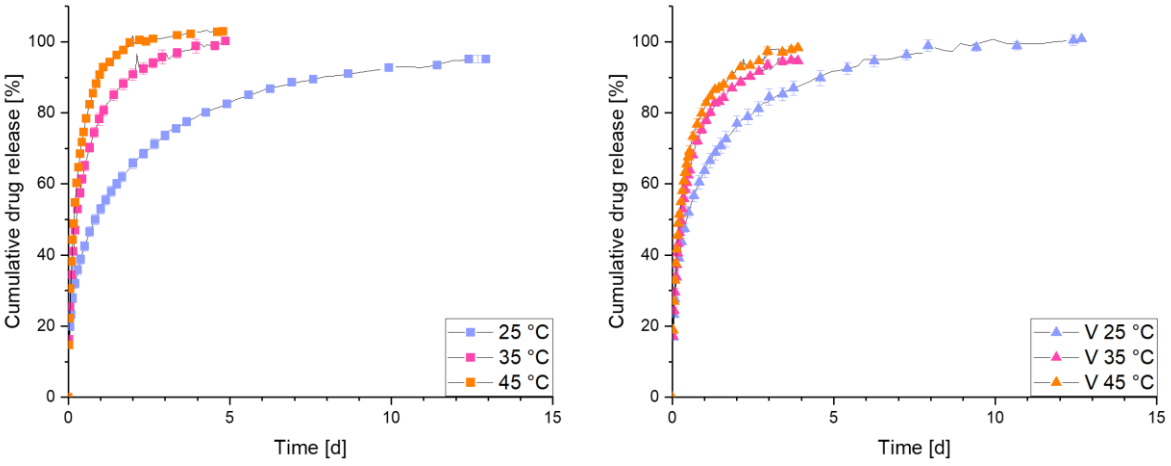

Figure 26. Dissolution profiles of drug-loaded PCL inserts dried under atmospheric (left) and reduced (right, V: vacuum dryer) pressure in 900 mL dem. water (37 °C) at 100 rpm; mean ± sd, n=3.

For each pressure condition the release was fastest for the inserts dried at 45 °C and slowest for inserts dried at 25 °C. For the inserts dried under atmospheric pressure, the diffusion pathways for the dissolved API molecules are longer, since the strands seem more compact and appear to have smaller pores. Under reduced pressure rounder strands were obtained including large pores that made the diffusion pathways shorter and therefore resulted in a faster drug release. The higher porosity may also have led to a higher specific surface area which further increased the drug release.

Considering the intended sustained release application for the intravesical inserts developed in the scope of this work, drying the inserts at low temperatures and atmospheric pressure was considered most beneficial for achieving the required dissolution profiles. Therefore, drying at 25 °C under atmospheric pressure was applied to all inserts during further studies.

3.1.8 Summary

Efforts were made towards gaining process understanding to obtain suitable printing formulations and printed objects with reproducible and high quality.

Semi-solid printable formulations were successfully developed by carefully finetuning the ratios of polymer, solvent and plasticizer for the polymers EVA and PCL. The viscosity of those formulations was thereby identified as the most critical quality attribute for ensuring reproducible results.

Evaluation of the rheological properties gave valuable insights into the printing ink's behavior. Rotational and oscillatory rheometry were evaluated as tools to roughly categorize printable formulations during early stages of formulation development. Recovery of the formulation after applying high shear stresses can thereby give predictive information on whether a printing ink can withstand the printing process while recovering sufficiently to ensure shape fidelity of the printed object. Strand thickness as one indicator for the printability of a trial formulation was assessed to be highly affected by printing temperature, pressure and speed and could be widely influenced by varying the printing settings of the 3D-printer. Initial characterization of a formulation's suitability for 3D-printing was feasible by applying the layer stacking test. Optimization of the printing conditions speed and pressure was successfully investigated in a CCD design of experiments that demonstrated the possibility of finding optimal process settings. The quality of the printed object was thereby evaluated e.g. by the newly developed printability score that seemed to be a promising measure to quantitatively assess the print quality. The DoE revealed that the range for achieving acceptable printed inserts was smaller for the EVA formulation compared to PCL under the investigated experimental conditions.

Post process drying was further identified as critical process parameter with high impact on the insert's properties such as porosity, geometry and release behavior. For sustained release applications it was considered most beneficial to dry the inserts under atmospheric pressure and lower temperatures. Gaining process understanding was essential for the development of suitable inks in the following chapter.

3.2 Manufacturing of sustained release intravesical inserts for long-term presence in the urinary bladder

3.2.1 Introduction and objectives

The aim of the following chapter was to develop sustained release flexible drug-loaded intravesical inserts. The purpose of their application is to enable long-term application of APIs with different properties to improve patients' acceptability for such dosage forms.

For their development, the use of polycaprolactone (biodegradable) and ethylene vinyl acetate copolymer (non-biodegradable) was investigated. The starting point of formulation development was based on pre-trials during which printable formulations were obtained. One objective of the following chapter was to explore the addition of additives to these formulations to prolong the release.

The suitability of the developed systems for the long-term application of the three APIs lidocaine hydrochloride (LC-HCl), trospium chloride (TrCl) and hydrochlorothiazide (HCT) was investigated for both polymers.

One of the degradable polymer-drug combinations with a fast observed drug release was chosen to study the effect of drug load and insert design on dissolution and explore the possibility of fine-tuning drug release. To investigate the influence of porosity on dissolution, a method was developed to quantify the porosity of the inserts and correlate it with drug release.

The degradable insert containing TrCl was further refined by investigating other biodegradable polymers with more favorable properties for the intended application.

Lastly, a short-term stability study was performed to determine whether the developed inserts would remain stable for some time throughout storage.

3.2.2 3D-Printing of inserts

After designing the CAD-files and preparing the semi-solid formulations, they were printed into net-shaped circular inserts (see Figure 27).

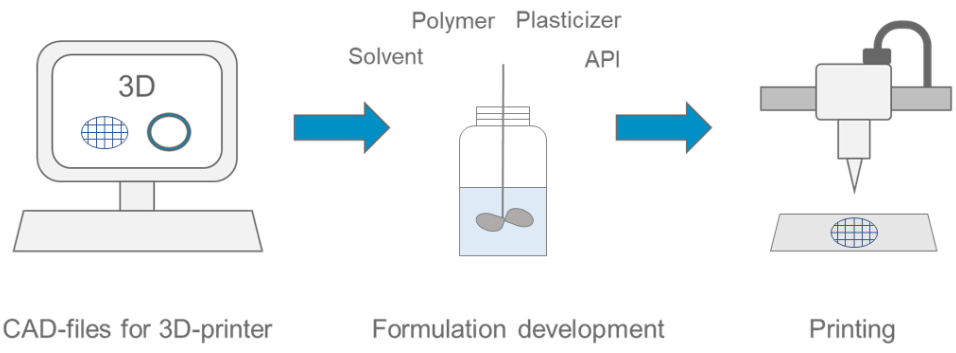

Figure 27. Schematic overview of printing process according to (Rahman-Yildir et al., 2022a) by courtesy of Elsevier.

Printing parameters were carefully adjusted to obtain inserts with high shape fidelity and resolution. The printed inserts were tested regarding their flexibility by rolling them up and placing them into a glass tube of 6 mm inner diameter (corresponding to 18 Charrière) to demonstrate their applicability via conventional urinary catheter (see Figure 28). After removing the coiled inserts from the glass tube, they unfold within 5-10 seconds to resume their original shape.

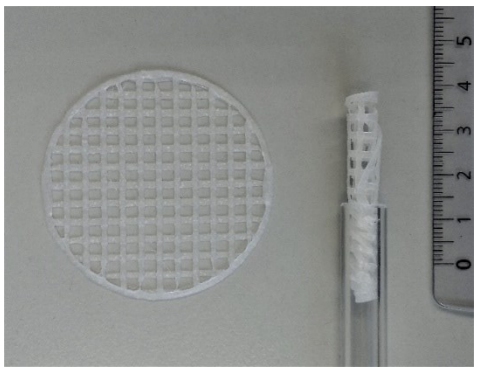

Figure 28. Printed net-shaped inserts unfolded (left) and coiled up (right) for insertion via catheter according to (Rahman-Yildir et al., 2022a) by courtesy of Elsevier.

3.2.3 Starting point of formulation development

Based on formulation pre-trials, formulations with LC-HCl were printed according to the composition in Table 10 and subjected to release studies. To avoid floating of the inserts on the surface of the dissolution medium due to their low density, the basket method (USP type 1) was selected.

Table 10. Composition of semi-solid printing formulation of first printing trials.

Formulation [%, w/w]	PCL	EVA	THF	DBS	LC-HCl
PCL	31	-	46	15	8
EVA	-	38	46	8	8

The corresponding dissolution curves are shown in Figure 29.

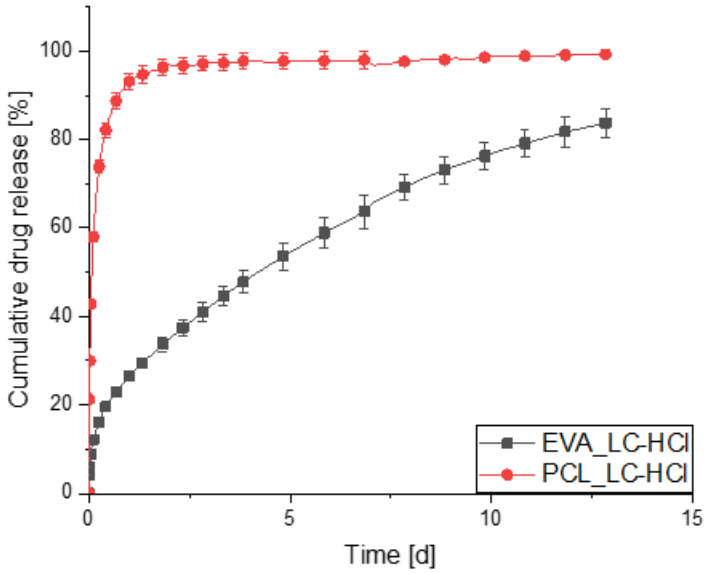

Figure 29. Release curves of LC-HCl-loaded EVA and PCL inserts in 900 mL dem. water at 100 rpm; mean ± sd, n=3.

From the high obtained correlation coefficients, it could be seen for both formulations that the drug release followed a Higuchi drug release kinetic (see Table 11). This was in accordance with the literature decribing a release for API particles that are suspended within a (polymeric) matrix (Higuchi, 1963b).

Table 11. Calculated R^2 according to Higuchi and Korsmeyer-Peppas (KP) model and KP diffusional exponent n; values given as mean of triplicate measurements.

Polymer	PCL	EVA
Higuchi R^2	0.97	0.99
KP R^2	0.98	0.99
KP exponent n	0.42	0.41

As the aim was to develop sustained-release inserts that would be able to release the API over the course of several weeks, the overall drug release was still too fast especially for the PCL formulation. In this case, a high amount of plasticizer was required to ensure sufficient flexibility, which may have caused higher chain mobility and therefore less rigid entrapment of the API within the matrix.

The inserts were further analyzed after dissolution via scanning electron microscope to investigate the surface morphology and internal structure. Figure 30 indicates that the surface of both inserts showed some small pores, but especially the internal structure seemed to be highly porous. This could explain the fast release that was observed for the inserts. The formation of a porous network upon dissolution

could thereby enhance water permeation into the matrix and facilitate the dissolution of the highly water-soluble API LC-HCl.

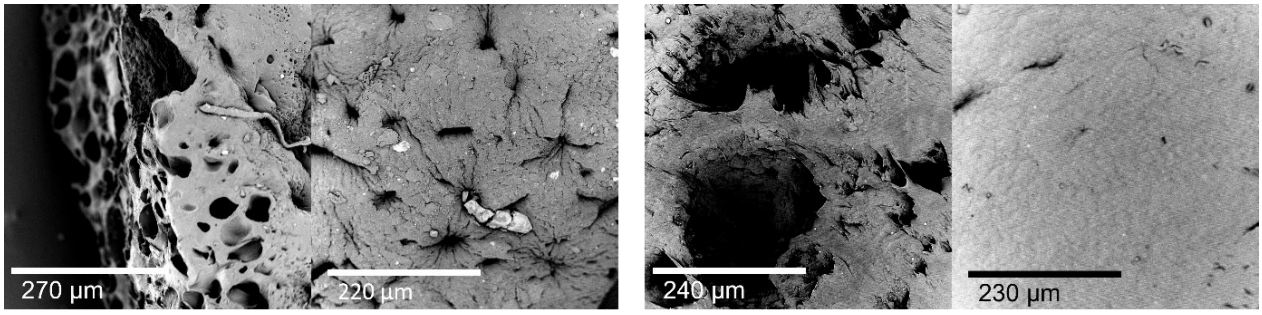

Figure 30. SEM images of cross-sections (left) and surface (right) of inserts after dissolution studies (EVA left, PCL right).

According to the Higuchi equation, different approaches can be taken to reduce the release rate. Taking the internal structure and high porosity into account, one approach may be the reduction of the surface area. Another approach would be to lower the drug load or to choose different polymers/APIs to create a higher attraction of the API to the matrix.

In the following chapters, different approaches were taken to influence the release rate of these inserts.

3.2.4 Effect of additives

3.2.4.1 Selection of additives

To further sustain the drug release, it was hypothesized that additives may be added to the formulation that would be able to block the pores within the matrix and so create diffusion barriers for the dissolved API particles and dissolution medium.

Hydroxypropyl methylcellulose (HPMC) was selected as water soluble and swellable potential pore-blocking agent that could sustain the initial phase of drug release.

Additionally, Eudragit® RS was chosen as pH-independently swellable, non-water-soluble additive with low permeability to potentially achieve a sustained drug release while being less prone to be washed out of the pores over time compared to HPMC. Incorporation of the additives required adjustment of the respective printing conditions to obtain inserts with high shape fidelity (see Table *35* for reference of composition and applied printing conditions).

3.2.4.2 Dissolution testing

As seen in Figure 31, HPMC acted as pore forming agent instead of blocking the pores as diffusion barrier. In this case the release of LC-HCl from the EVA matrix was enhanced compared to the HPMC-free formulation. This may have occurred due to the good water solubility of HPMC which led to washing out of the polymer and thus creating more pores. Therefore, HPMC was proven to be unsuitable for sustaining the drug release.

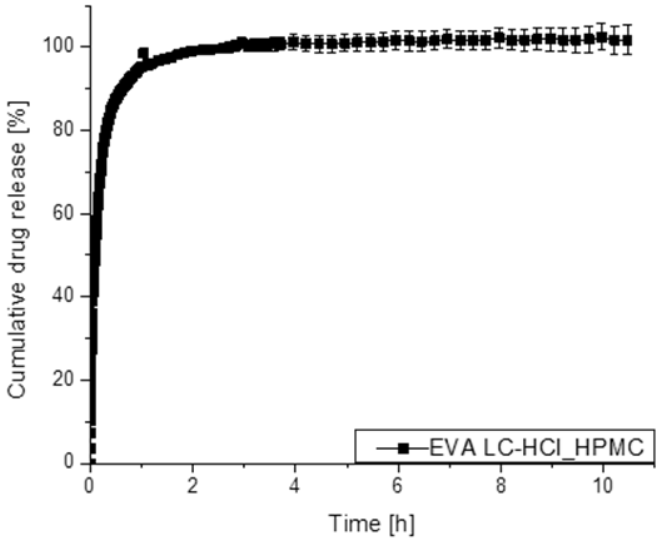

Figure 31. Cumulative dissolution profile of LC-HCl-loaded EVA insert with added HPMC in 900 mL dem. water at 100 rpm; mean ± sd, n=3.

Also in case of Eudragit RS, the drug release could not be further delayed (see Figure 33). For 3 % added Eudragit® RS, the EVA formulation also exhibited an enhanced drug release compared to the formulation without additive. When increasing the ratio of the additive to 5 %, the initial drug release was slightly decreased up to 4 days but then exceeded the release of the additive-free formulation. This indicates that the approach was only partly successful and apparently a diffusion barrier was only able to be kept intact for the first few days of release. However, after this phase the polymer seems to have been washed out of the pores as well. For the 3 % Eudragit formulation this effect could not be achieved even for the initial phase.

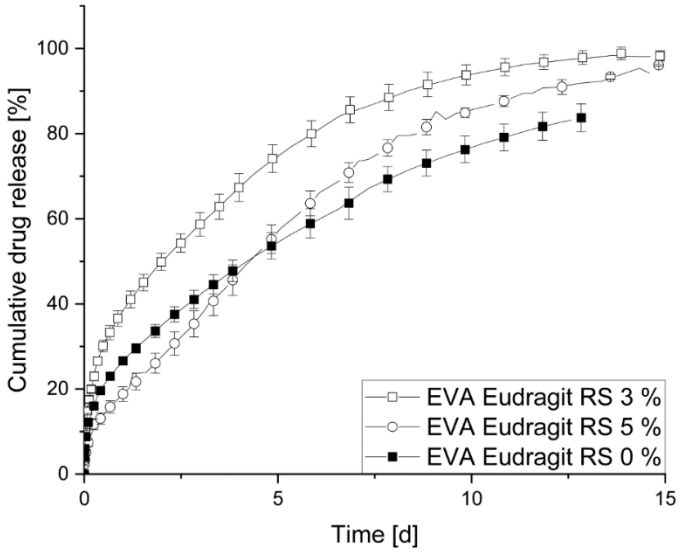

Figure 33. Cumulative dissolution profiles of LC-HCl-loaded EVA inserts with and without added Eudragit RS in 900 mL dem. water at 100 rpm; mean ± sd, n=3.

For PCL the drug release could also not be sustained by incorporating 3 % Eudragit RS (see Figure 32).

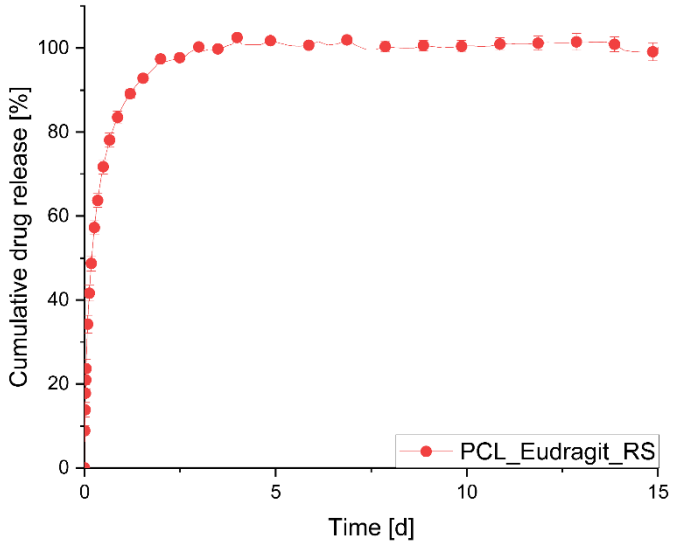

Figure 32. Cumulative dissolution profiles of LC-HCl-loaded PCL inserts with added Eudragit RS in 900 mL dem. water at 100 rpm; mean ± sd, n=3.

In this case the observed drug release remained practically unchanged compared to the formulation without additive.

The pores inside the matrix of the inserts could not sufficiently be blocked by the additive so that water permeation into the matrix was not inhibited and a diffusion barrier was not formed. To achieve an effective diffusion barrier the additive would have to be present in most of the pores or surround the insert with a layer of low permeability. Since this was not achieved by incorporating the additives into the semi-solid formulations before printing and the polymer did not swell sufficiently to block most of

the pores, this approach was not successful. Addition of further additives was therefore discarded from further formulation development to sustain the drug release.

3.2.5 Effect of API and polymer

3.2.5.1 Formulations

To study the effect of matrix polymer and API on the drug release and determine favorable combinations for sustained release applications, 10 % drug-loaded formulations with three different APIs were prepared and printed according to Table 12.

Table 12. Composition and printing conditions of semi-solid printing formulations. Final drug-loaded inserts after drying were gravimetrically assessed to contain less than 7.2 mg solvent (THF).

Formulation [%, w/w]	PCL	EVA	THF	DBS	API	Printing speed [mm/s]	Printing pressure [bar]
PCL LC-HCl	37.5	-	37.5	19	6	20	1.3
PCL TrCL	37.5	-	37.5	19	6	20	1.3
PCL HCT	37.5	-	37.5	19	6	20	1.2
EVA LC-HCl	-	40	47	8	5	20	1.0
EVA TrCL	-	40	47	8	5	20	0.8
EVA HCT	-	44	41	9	6	18	2.3

3.2.5.2 Dissolution testing

Dissolution studies under sink conditions revealed different release profiles of the APIs depending on the matrix-polymers and the APIs' solubilities (Table 13).

Table 13. Saturation solubilities and maximum concentrations achieved in dissolution medium during release studies of LC-HCl, TrCl and HCT in dem. water.

	Solubility at 37 °C in dem. H_2O [mg/mL]	Maximum concentration during dissolution [mg/ml]
LC-HCl	814	0.13
TrCl	636	0.13
HCT	1.03	0.04

All inserts followed a Higuchi release kinetic as the drug particles of all three drugs are suspended within a polymeric matrix (see Table 14) (Higuchi, 1963a; Siepmann and Siepmann, 2012). The application of the Korsmeyer-Peppas (KP) model further allowed determination of the KP exponent n. As reported in the literature, depending on the geometry, values close to 0.45 indicate that the release is controlled by Fickian diffusion which seems applicable for the LC-HCl loaded inserts. Values from 0.45 to 0.89 suggest an anomalous drug transport behavior between Fickian diffusion and Case II

transport for cylindrical geometries (Peppas and Sahlin, 1989; Ritger and Peppas, 1987; Siepmann and Peppas, 2011) which appears to be the case for the TrCl- and HCT-loaded PCL inserts.

Table 14. Calculated R2 according to Higuchi and Korsmeyer-Peppas (KP) model, diffusional exponent n according to KP model and amount of released API after 14 d; mean ± sd, n=3.

	LC-HCl		TrCl		HCT	
Polymer	PCL	EVA	PCL	EVA	PCL	EVA
Higuchi R^2	0.98	0.99	0.99	-	0.99	-
KP exponent	0.45	0.42	0.52	-	0.57	-
KP R^2	0.99	0.99	0.98	-	0.99	-
% drug release after 14 d	92 ± 0.4	82 ± 2.5	99 ± 0.5	43 ± 2.2	75 ± 2.1	9 ± 0.6

For the non-degradable EVA polymer, the dissolution of the API followed the solubility of the API in the dissolution medium i.e., that the highest soluble API (LC-HCl) displayed the fastest release reaching approximately 82 % after 14 days (see Figure 34, left). The slowest release was seen for the EVA insert containing HCT, which had the lowest solubility in water (see Table 13).

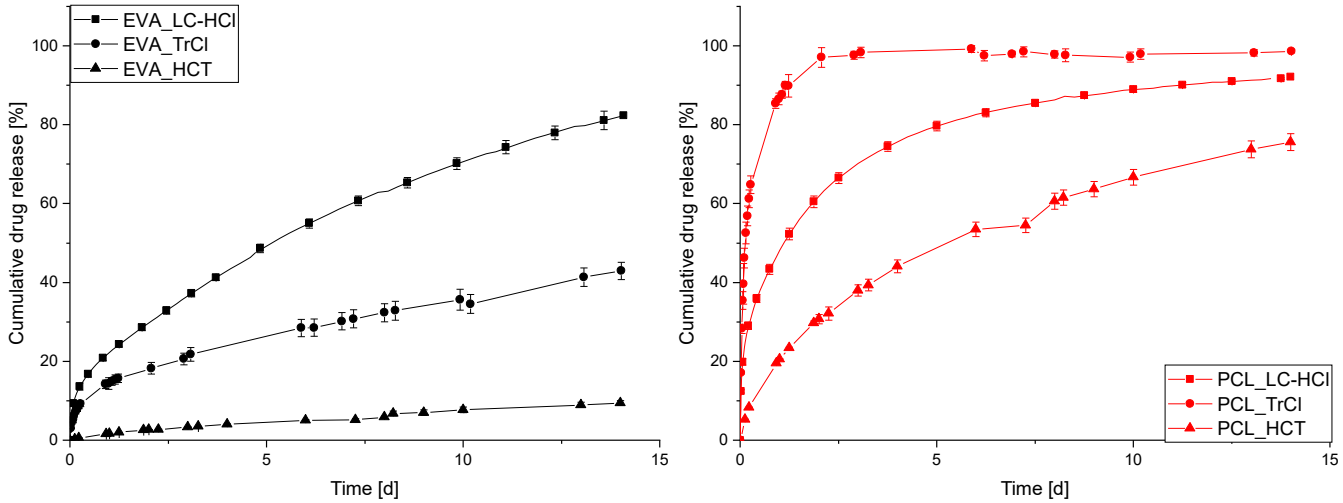

Figure 34. Dissolution profiles of drug-loaded EVA (left) and PCL (right) inserts in 900 mL dem. water at 100 rpm, mean ± sd, n=3. Used from (Rahman-Yildir et al., 2022a), by courtesy of Elsevier.

The high solubility of the API in the dissolution medium allows the dispersed drug crystals within the matrix to be dissolved and released fast while leaving behind a porous network that further accelerates drug release.

For the PCL inserts, however, a different trend is visible. Here it can be seen that the drug release was fastest for TrCl, reaching a plateau after approximately 2 days, although its solubility was determined to be slightly lower than LC-HCl (636 mg/mL and 814 mg/mL respectively), in which case 92 % of API release was observed after 14 days. HCT showed the slowest release also in case of the PCL insert, reaching a drug release of 75 % after 14 days of dissolution testing.

Generally, the release of the different APIs from the PCL inserts occurred faster than for the respective EVA inserts. One explanation could be the differences in wettability as seen from the results of the contact angle measurements (see Figure 35) that revealed a higher wettability for PCL with a contact angle of around 58° as opposed to EVA with a contact angle of around 90° after 60 s (Table 15), indicating that the dissolution medium could permeate easier into the PCL matrix and therefore accelerate the drug release.

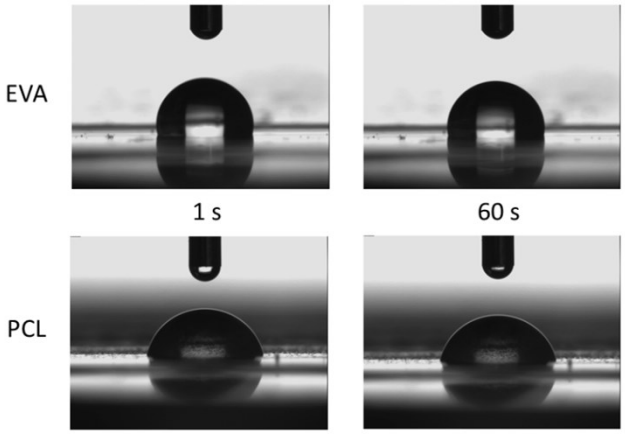

Figure 35. Images of drop shape analysis after 1 and 60 s of EVA (top) and PCL (bottom) films using dem. water. Modified from (Rahman-Yildir et al., 2022a), by courtesy of Elsevier.

The PCL insert further required a higher amount of plasticizer to achieve flexible inserts which may have led to increased chain mobility and therefore enhance the mobility of the API molecules allowing them to be released faster from these inserts (Cho et al., 2007).

Table 15. Contact angles for dem. water on EVA or PCL films; mean ± sd, n=3.

Contact angle [°]	1 s	60 s
EVA	92.8 ± 2.8	89.6 ± 1.6
PCL	57.6 ± 1.9	57.6 ± 1.5

During the investigated timeframe of the release studies the mass loss of the PCL inserts attributed to degradation was found to be less than 5 % and most of the polymeric matrix was still intact after dissolution Therefore, contributing effects of matrix erosion to the release behavior seem unlikely.
The drug release observed during the dissolution studies appear to be within therapeutically relevant magnitude for LC-HCl and TrCl. For LC-HCl, indwelling devices have been reported in the literature that exhibited comparable release of lidocaine over two weeks and were shown to be effective (Nickel et al., 2012). For TrCl, an effective concentration of at least 1 µg/mL was found previously in isolated pig bladder models (Von Walter, 2009) and could be achieved for the TrCl-loaded EVA insert between days 2-14 of the experiment. However, these concentration values were determined mathematically based

on the release rates and an assumed average daily bladder filling of an adult and would have to be confirmed in in-vivo studies.

3.2.5.3 Strand thickness

Measurements of the strand thickness revealed similar diameters for all inserts and could therefore not explain the differences observed during dissolution studies possibly caused by variations in diffusion pathways of the API molecules within the polymeric matrix (see Figure 36). It showed however, that adjustment of the printing settings resulted in homogeneous inserts regardless of the formulation.

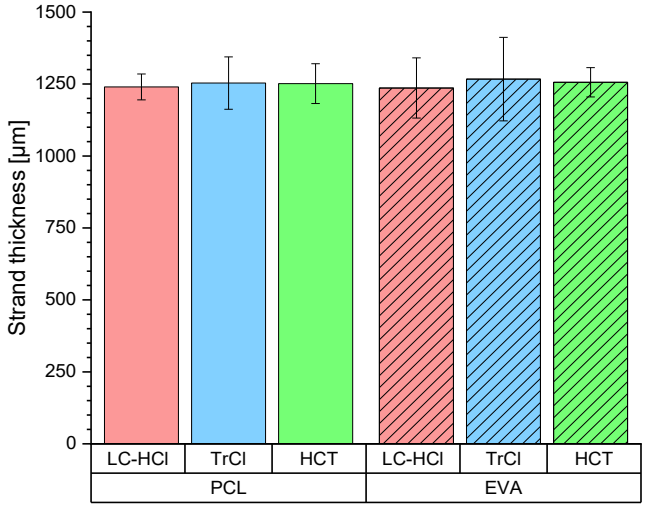

Figure 36. Strand diameters of drug-loaded PCL and EVA inserts; mean ± sd, n=18.

3.2.5.4 DSC measurements

Figure 37 displays the results of the DSC measurements of the plain excipients and printed drug-loaded inserts. In all cases endothermic melting peaks are visible for the pure APIs and the printed inserts.

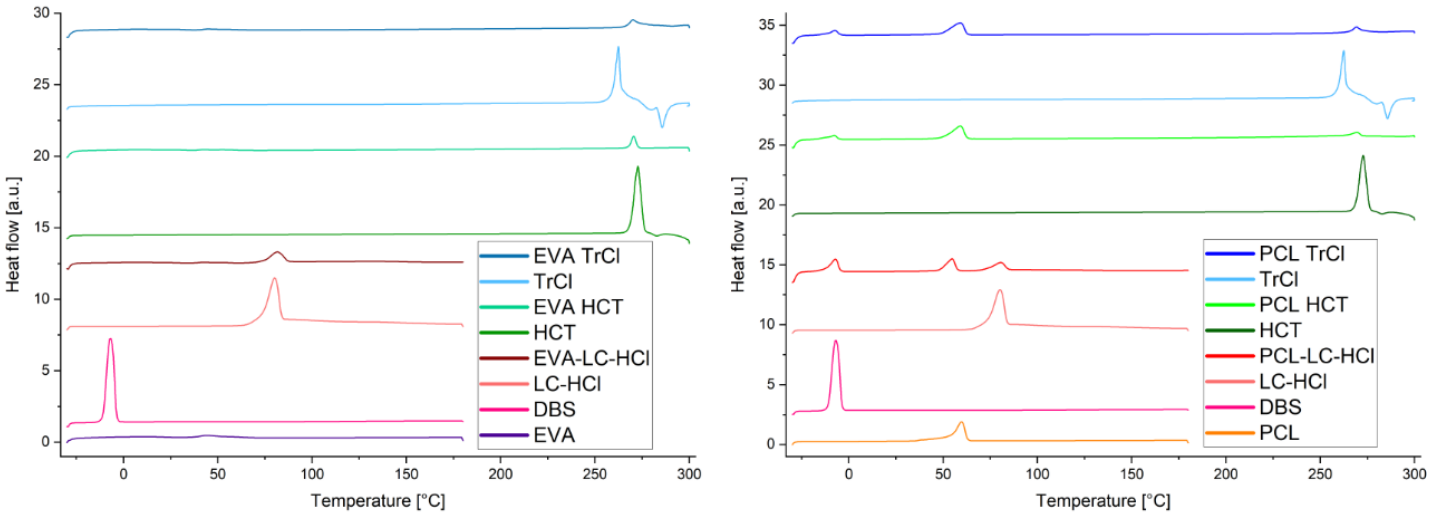

Figure 37. DSC diagrams of pure APIs, excipients, and drug-loaded EVA (left) and PCL (right) inserts (endo up). Used from (Rahman-Yildir et al., 2022a), by courtesy of Elsevier.

This indicates that the drug is present in crystalline form within the amorphous EVA-matrix or the semi-crystalline PCL-matrix of the inserts.

Therefore, differences seen in the dissolution profiles may not be attributed to the presence of larger quantities of the amorphous forms of the APIs. Furthermore, it shows that the printing process does not significantly change the crystallinity of the APIs.

3.2.5.5 FT-IR measurements

It was hypothesized that the different release behaviors seen for the PCL inserts with APIs of different solubility could be derived from deviating interactions between the polymer and API. However, the results from the FT-IR measurements do not provide conclusive evidence for this hypothesis (see Figure 38).

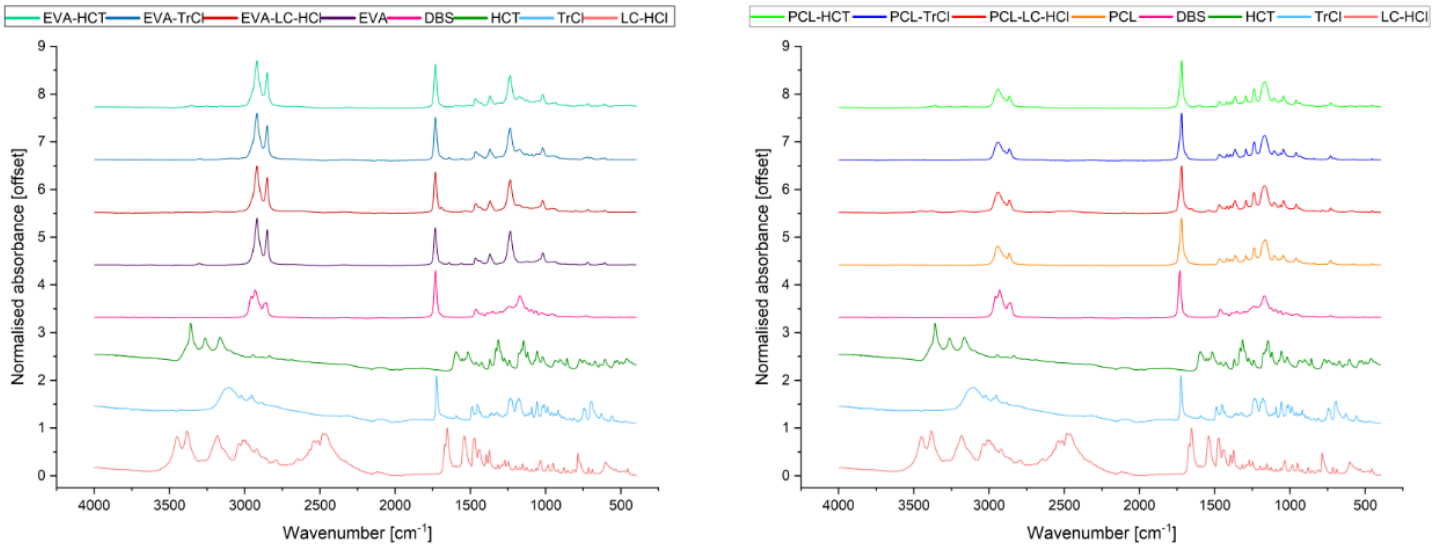

Figure 38. FT-IR spectra of pure APIs, excipients, and drug-loaded printed EVA (left) and PCL (right) inserts. Used from (Rahman-Yildir et al., 2022a), by courtesy of Elsevier.

For LC-HCl and TrCl the characteristic peaks seen for the APIs can be also seen in the printed inserts. There was no observable greater spectral shift or absence of certain bands. Therefore, it can be concluded, that no significant interaction between the APIs and excipients can be confirmed. For HCT some shifts were visible in case of the PCL-inserts, as well as the absence of some characteristic bands of the API in the printed insert, which indicates some interactions between HCT and PCL. Regarding LC-HCl, the drug showed N–H stretching vibration at 3450 and 3385 cm^{-1}, a small peak at 3010 cm^{-1} for an aromatic C-H stretch and a sharp band at 1653 cm^{-1} representing the C=O stretching of the amide group (Wei et al., 2014). Other two characteristic bands of LC-HCl at 1543 cm^{-1} and 1475 cm^{-1} were also observed in the printed inserts but mainly covered by the bands of the polymer, corresponding to C-N stretching (da Silva Anacleto et al., 2018). All characteristic bands of LC-HCl were present in the LC-HCl-loaded PCL-inserts without any noticeable change in band position indicating that LC-HCl did not interact with the polymeric matrix. Therefore, regarding the dissolution profile seen for this API it

cannot be concluded from the FT-IR measurements that the sustained release compared to the TrCl loaded inserts results from interactions between polymer and API.

For the TrCl-loaded samples, the peaks with maxima at 3111 cm^{-1} representing the stretching vibration of the O-H bond in the hydroxyl group and the band at 3025 cm^{-1} corresponding to the stretching vibration of the C-H bonds of the aromatic rings were not present as noticeable peaks in the scans of the printed inserts. Instead, there was a slight raise in the baseline visible, which could be caused by the API but cannot be confirmed with certainty. Bands at 2970 and 2885 cm^{-1} were observed due to the stretching vibration of the CH_2 groups of the pyrrolidine and the cycloheptane rings but were probably superimposed by the bands of the polymer in the printed inserts. The C=O group stretching vibration was located at 1726 cm^{-1} for all samples. The absorption bands for the stretching vibration of the C-O-C linkage involving the ester group were visible at 1180 cm^{-1} and the stretching vibration of the C-O bond in the C-OH group was present at 1055 cm^{-1}. However, these bands were hardly visible for the printed inserts. Furthermore, the band at 3111 cm^{-1} was in close proximity to the wavenumber 3130 cm^{-1} which is known to be caused by stretching vibration of O-H for a water molecule interacting via ionic hydrogen bond with a chloride anion and may therefore be difficult to interpret correctly (Urbanova et al., 2013). From these observations it may be concluded that interactions between polymer and API cannot be ruled out completely. Further experiments including different drug loads are needed for more profound interpretation.

The IR spectra of pure HCT showed characteristic bands at 3360 -3162 cm^{-1} corresponding to the N-H stretching vibration for drug and printed inserts. Bands at 1596 cm^{-1} for the C=O stretching showed a slight shift in the printed inserts towards higher wave numbers (1606 cm^{-1}) indicating some interactions between polymer and drug. A band at 1518 cm^{-1} for the S=O stretching was observed in both API and printed insert. The band at 1057 cm^{-1} was present in the pure API's spectrum but not seen in the printed inserts (corresponding to aromatic C=H stretch). It is evident that most of the characteristic peaks that were present in the spectra of the pure drug were also visible in the same region in the spectra of the printed insert. Some exceptions seen in peak shifts toward higher wave numbers indicate that there may be some interaction between the drug and the polymer (Babu et al., 2014) which is in accordance with the slow release seen in the dissolution profiles.

In the case of all EVA samples, no absence or shift in peaks of the pure API and printed insert were visible, which lead to the conclusion that there was no major interaction between EVA and the respective APIs observable and may therefore not explain differences observed during dissolution (see Figure 38, left).

3.2.5.6 Evaluation of the morphology - Raman and SEM measurements

To gain more insights into the different trends seen for the dissolution profiles of the investigated drug-polymer combinations, independent imaging methods were applied to examine the inner structure of the inserts as well as the API distribution within the printed objects.

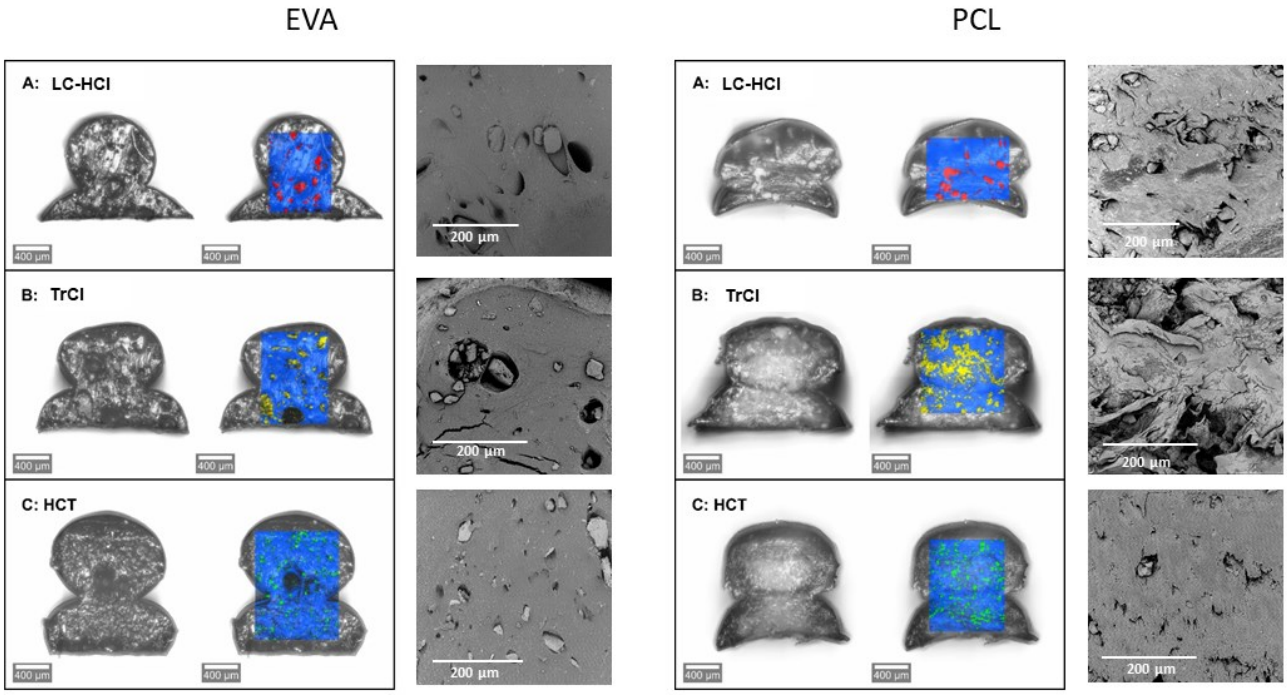

Figure 39. Raman-microscopy bright-field (left) and SEM (right) images of cross-sections of printed drug-loaded inserts. EVA-inserts displayed left, PCL-inserts right. Polymers displayed in blue, LC-HCl in red, TrCl in yellow and HCT in green. Used from (Rahman-Yildir et al., 2022a), by courtesy of Elsevier.

For the EVA inserts, Raman microscopy showed the formation of bigger API particles and clusters in the TrCl-loaded insert, whereas HCT seemed to be finely dispersed (see Figure 39, left).

The particle size of the LC-HCl crystals and the TrCl crystals seemed to be comparable, while the HCT crystals appeared much smaller. This resonates with the dissolution data, since the freely soluble LC-HCl and TrCl have a similar distribution of the API within the matrix and therefore their dissolution speed in the dissolution medium may depend on the API's solubility.

For the PCL inserts however, in the case of LC-HCl there seemed to be bigger particles embedded in the homogeneous polymer matrix (right side of image). The other two inserts showed a finer dispersion of the particles throughout the matrix. Furthermore, the matrix seemed to be rougher and more disrupted especially for the TrCl insert (see SEM images), which could explain the observed release behavior. Therefore, it may be concluded that the faster drug release despite the lower solubility of TrCl compared to LC-HCl occurred because the API particles were more finely dispersed (and smaller in size) and seemingly caused a less smooth matrix, which would allow a faster dissolution of the API

and easier permeation of water into the matrix. For the case of HCT, the much lower solubility seems to be the predominant cause for the sustained release.

3.2.6 Effect of drug load

In order to evaluate the effect of drug load on the resulting drug release and generate inserts with different release profiles, model PCL implants were printed with 5, 10 and 15 % LC-HCl. LC-HCl in PCL was used as model system because here the biggest particles were embedded into the homogeneous PCL matrix (see section 3.2.5.6.) which should reveal the biggest differences for different drug loads.

As expected, the lower drug load showed the slowest release, reaching approximately 78 % after 2 weeks, whereas the 15 % drug-loaded inserts reached the plateau after only 4 days (see Figure 40, left). The dissolved API crystals will leave behind pores that create a porous network enabling water to penetrate faster into the matrix and dissolve the remaining API. This effect is enhanced when the drug load is higher, and more API particles are present.

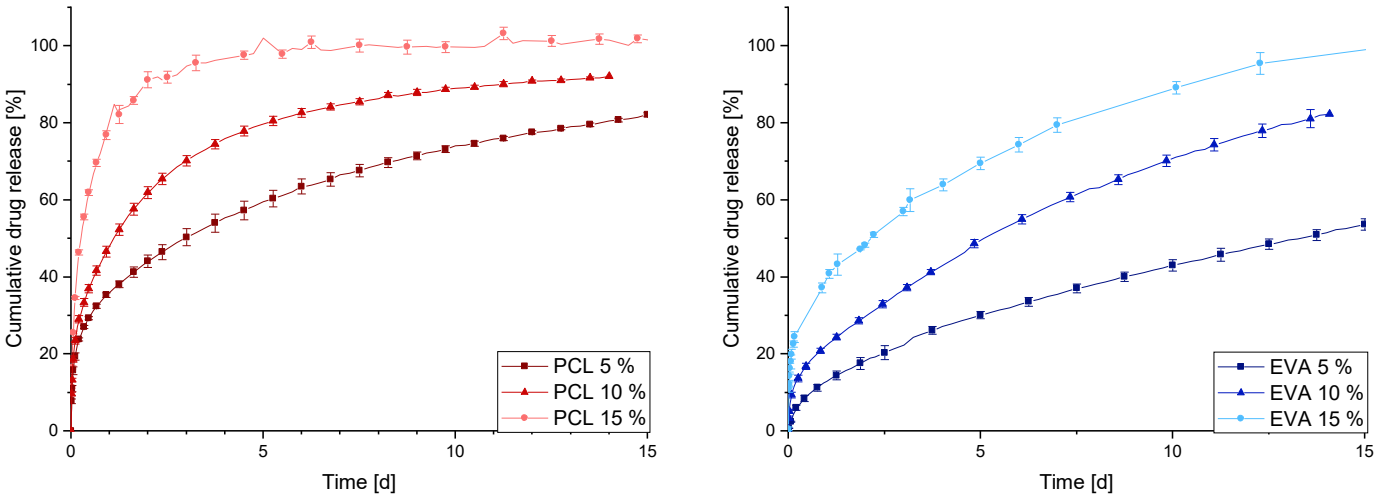

Figure 40. Dissolution profiles of LC-HCl-loaded PCL and EVA inserts with different drug loads in 900 mL dem. water at 100 rpm; mean ± sd, n=3 (modified from (Rahman-Yildir et al., 2022a), by courtesy of Elsevier).

This experiment was also carried out for LC-HCl-loaded EVA formulations. The corresponding release profiles showed the same trend for different drug loads as seen for the PCL inserts (see Figure 40, right). Also in this case, as expected, the drug release was significantly slower for the lower drug load.

3.2.7 Effect of geometry

3.2.7.1 Strand thickness and mass

Since 3D-printing allows a fast and easy manipulation of the shape of a printed object, the design was modified to alter the release properties of the insert and simulate different desirable release profiles depending on the intended treatment. The formulation of the 10 % LC-HCl-loaded PCL insert was used

to print different amounts of layers as well as an insert with three layers without infill and a ring printed in three layers with a double contour (see Figure 41).

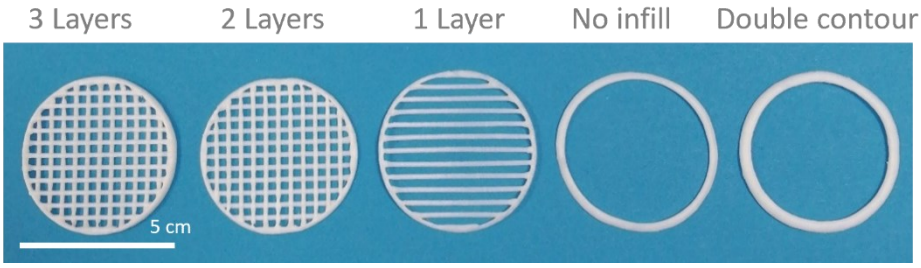

Figure 41. Images of LC-HCl-loaded PCL inserts with different geometries (modified from (Rahman-Yildir et al., 2022a), by courtesy of Elsevier).

As seen in Figure 42, the diameter of the printed strands varies significantly when the geometry of the insert is altered.

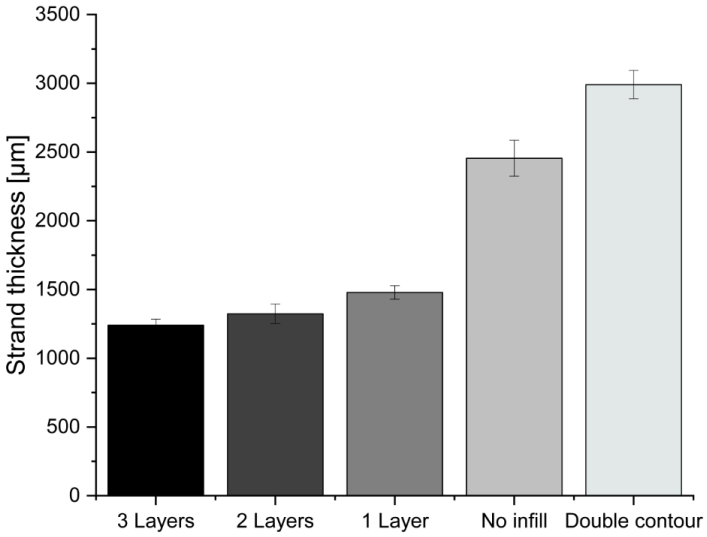

Figure 42. Strand thickness of inserts printed with different number of layers, without infill and ring with double contour; mean ± sd, n=10.

While with increasing number of layers the diameter only increases slightly, large differences are visible when no infill is printed. When the infill is printed, the outer contour that is printed beforehand, experiences forces from the printed strands that hold the contour together and pull the formulation slightly inward. This prevents the contour from flowing apart, since it is to some extent fixed by the connected inner strands. This effect is more pronounced when more layers are printed. In case of the double contour, the weight of the material that is extruded on top will also cause the layers below to flow apart even more, resulting in larger contour diameters. Since the second contour is printed next to the first contour of one layer before the formulation can dry, the two contours flow together immediately and form one large strand. In this case the widest point of the insert was approx. 3.0 mm

which was above the designated limit of 1.5 mm. It would have to be confirmed during in-vivo studies whether this would be critical for safe application concerning blockage of the urethra.

As expected, the amount of material (and therefore API amount) printed is proportional to the number of layers or contours printed (see Figure 43). This limits the deliverable amount of drug for a given geometry and must be kept in mind when dose adjustment needs to be performed.

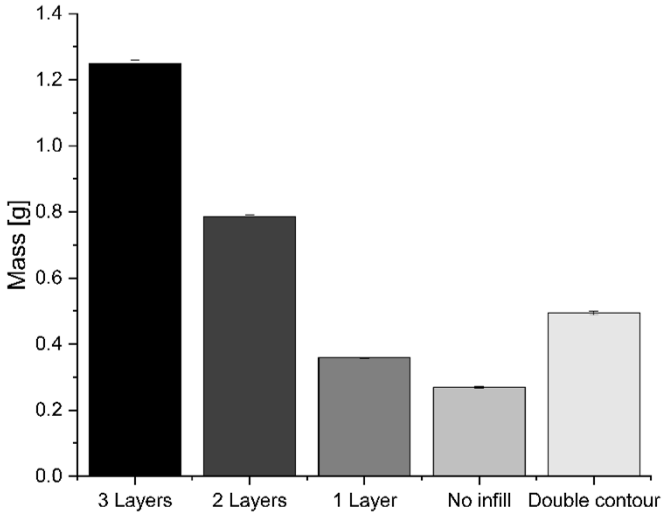

Figure 43. Mass of inserts printed with different number of layers, without infill and ring with double contour; mean ± sd, n=6.

3.2.7.2 Dissolution testing

As seen in the dissolution profiles, the drug release was enhanced when less layers were printed and slowest when only the ring without infill was printed (see Figure 44).

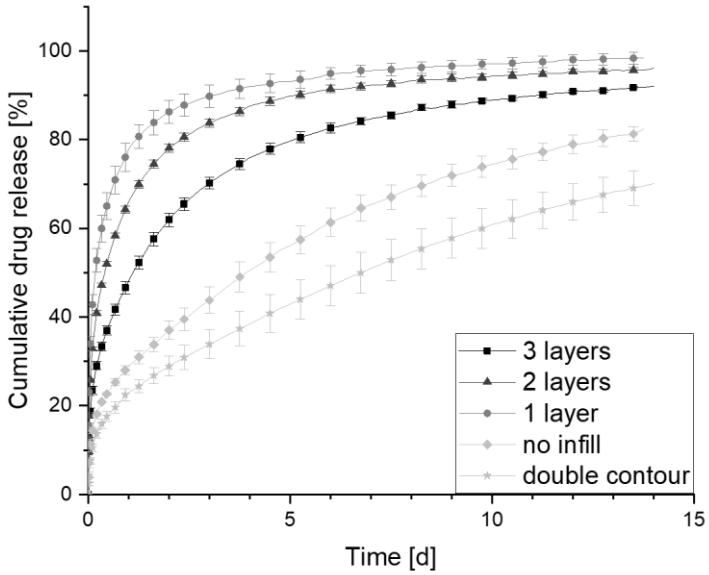

Figure 44. Dissolution profiles of LC-HCl-loaded PCL inserts with different geometries in 900 mL dem. water at 100 rpm; mean ± sd, n=3. (modified from (Rahman-Yildir et al., 2022a), by courtesy of Elsevier)

50 % of drug release were reached after approx. 1.1 days when three layers were printed, as opposed to 0.5 days for 2 layers and only 0.2 days for 1 layer. The rings without infill and one or two contours reached 50 % of LC-HCl release after 4 and 7 days respectively.

This may have occurred because of a lower surface area to volume (SA/V) ratio in case of more layers, since strands are partially overlapping and therefore decreasing the overall surface area compared to the single layers

From the literature it is well-known that larger SA/V ratios increase the drug release due to the higher surface area available to the dissolution medium (El Aita et al., 2020; Raju et al., 2014; Windolf et al., 2021). Furthermore, overlapping strands that are partially fused together will create longer diffusion pathways for the dissolved API particles and therefore extend the release. In case of the ring without infill the release is even slower, since three strands are fused together, and no thin strands are present where diffusion pathways are shortest. The effect is enhanced when a double contour is printed which translates to an even larger strand-diameter. This shows that the dissolution profile of the same formulation can be easily adapted by manipulating the shape of the insert which can be beneficial depending on whether a short or long-term treatment is desired.

3.2.8 Effect of porosity

3.2.8.1 Porosity-influencing factors

As described in chapter 3.1.7, the porosity of a drug delivery system can have a great impact on its dissolution profile. Therefore, in the following chapter the effect of porosity was investigated in more detail. To reduce the porosity of the inserts to achieve a more sustained release, its cause and influencing factors need to be identified first. The main influencing factors were determined to be the formulation itself, the preparation method and post-processing steps (see Figure 45).

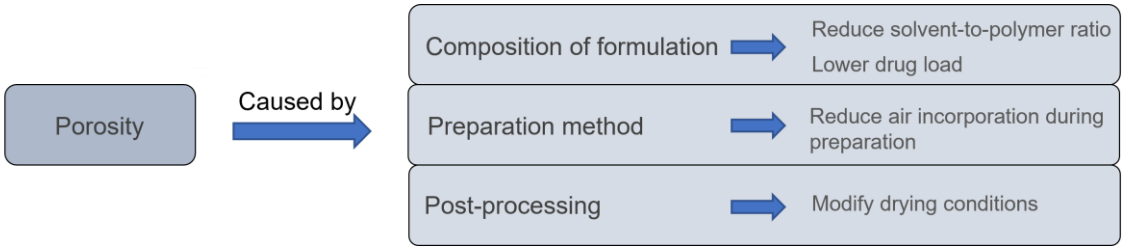

Figure 45. Causes for porosity of printed inserts and possible ways of influencing them.

Since the semi-solid printing formulation typically contains a solvent that will evaporate during drying and may also cause formation of bubbles during preparation, a reduced solvent to polymer ratio could potentially reduce the porosity of the resulting insert. The drug load of the insert also plays a key role, as the suspended drug particles will lead to formation of pores within the polymeric matrix upon dissolution. Further, during preparation of the semi-solid formulation air is usually incorporated into

the mixture during stirring. This could possibly be reduced by applying gentler mixing or introducing a resting period after agitation in which the entrapped gas bubbles have time to escape the formulation. Since early development has shown that decreasing the rotation speed of the overhead stirrer by half did not result in sustained release of the drug loaded inserts, this approach was considered ineffective. Furthermore, allowing the formulation to rest for one hour after mixing also did not show the desired effect and was therefore not pursued further. As the drug particles were suspended within the investigated formulations, a too long rest time also led to sedimentation of the particles and even particle growth over time that led to blockage of the printing nozzle. Therefore, longer resting times were not implemented. However, since the printing process itself takes less than three minutes per insert, sedimentation of the drug particles during printing of one batch was not observed.

Stirring the mixture under vacuum to avoid air incorporation was also not considered to be a viable option since removal of the incorporated solvent was not desired. Therefore, the porosity caused by the preparation method was inevitable due to the nature of the process and formulation.

Lastly, as shown previously, the post-process drying has a big influence on the formation of pores and its modification should be considered carefully.

3.2.8.2 Quantification of porosity

To gain understanding of the effect of porosity on the dissolution of the printed inserts, a method was required to reliably allow its determination.

Porosity of a given sample is typically determined by standard methods such as helium pyknometry or gravimetric measurements when the density of all involved components are known. This, however, becomes difficult in multi-component systems where the exact density of the matrix with API is not known. Gas adsorption methods such as BET to estimate the surface area of a sample and get an approximation of the sample's porosity or mercury porosimetry are well established methods to investigate the porosity of a sample (Markl et al., 2018; Sinha et al., 2019). These methods rely on a gaseous or liquid fluid to be able to directly access the sample's pore volume. However, their drawbacks are that the inner porosity cannot be determined and that the measurements are sensitive to the samples' wettability.

Porosity can also qualitatively be assessed e.g. by optical microscopy or SEM imaging. In these cases, inner pores can be made visible, but their quantification remains difficult, since only small sections of the sample are investigated and extrapolation to the entire sample would be error prone. Another disadvantage is, that the sample must be destroyed for the measurement.

In the scope of the present work, µCT imaging was used to determine the pores within printed inserts. The benefit of this method is that the entire sample can be measured without destroying it. This allows pore quantification through analysis of the resulting images and direct correlation to the release curves obtained during dissolution studies of the same sample. It must be mentioned however, that this method is limited to the achievable resolution of the µCT images. Oftentimes, compromises must be made between the resolution of the image and size of the investigated object. For this purpose, a custom-made 3D-printed fixture was designed to keep the insert in place during measurements (see Figure 46).

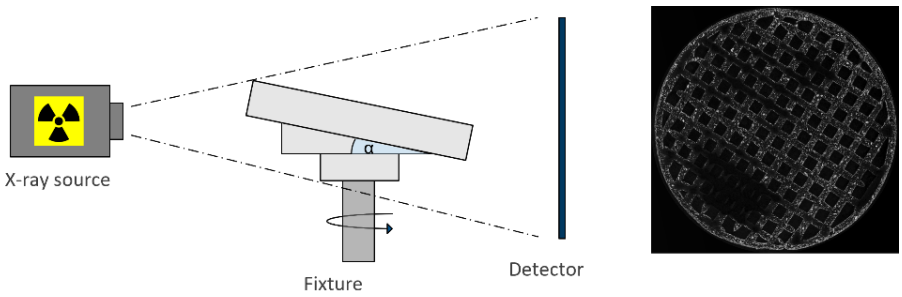

Figure 46. Scheme of µCT images being taken of printed inserts in customized sample holder.

The fixture was improved from a larger sample holder that could hold the insert unfolded to a smaller fixture for which the sample was folded twice and so reduced in size. This size reduction of the sample's diameter allowed the fixture to be placed closer to the X-ray source of the µCT and so resulted in images of higher resolution. This in turn results in a more reliable measurement since also smaller pores can be determined. It was feasible to distinguish polymeric matrix, API-crystals and pores in the µCT images of the printed inserts due to their different densities. Image analysis was applied to divide the grey values of the components into different clusters representing matrix and pores/air. By quantifying those ratios and summing up the so obtained values of the air and matrix, it was considered feasible to determine the inner porosity caused by evaporated solvent and incorporated air before dissolution as well as pores caused by dissolved drug particles after dissolution.

One main challenge throughout the development of this quantification method was to distinguish between air bubbles inside the printed strands and mesh holes within the net-structure of the printed infill pattern. When creating a grey-scale image of the insert during image analysis, mesh holes and air bubbles cause the same grey values since they have the same density. This could be overcome by applying a size exclusion function that allowed quantification of pores that did not exceed a certain size threshold.

Through image analysis it was feasible to determine the volume of the air and matrix separately from each other (see Figure 47) as well as their surfaces (Figure 48).

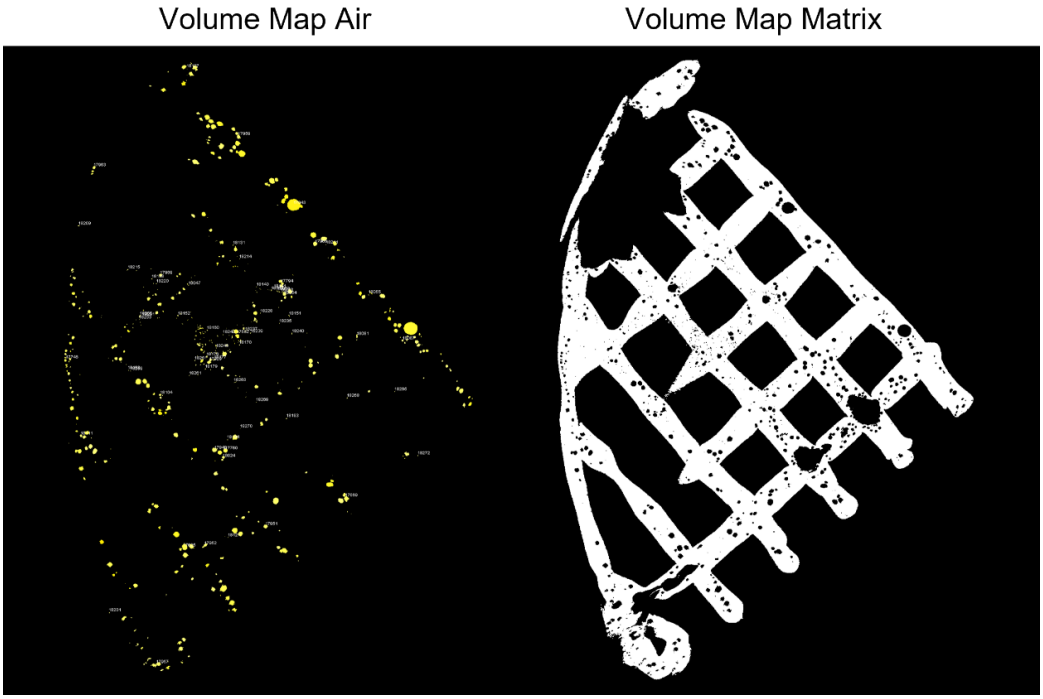

Figure 47. Exemplary images of volume maps of inserts obtained during image analysis of µCT images.

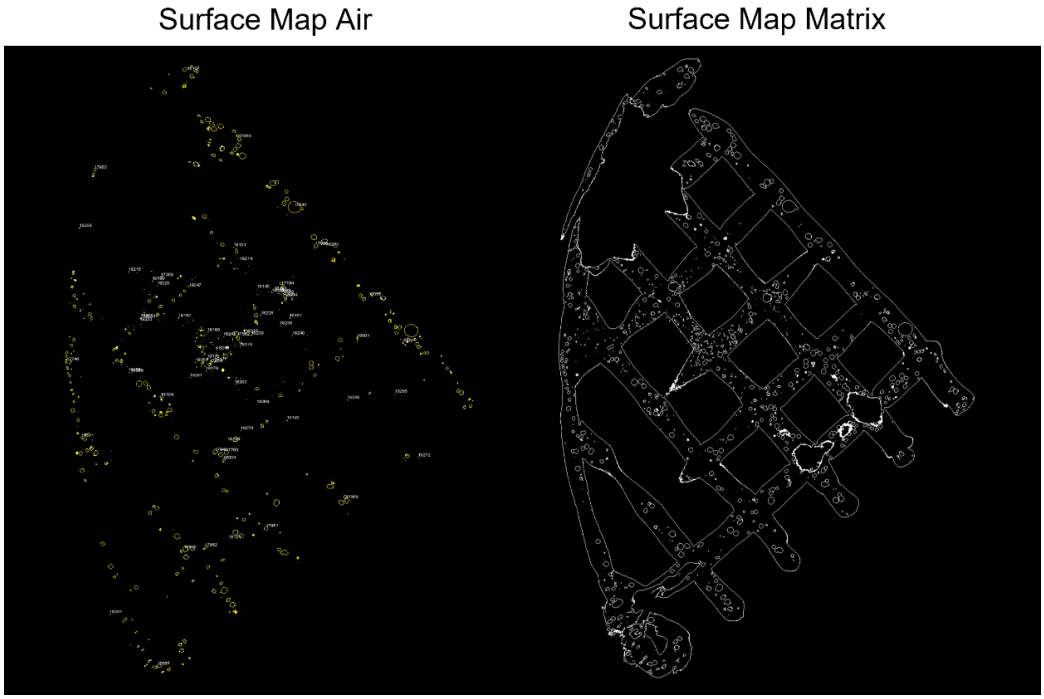

Figure 48. Exemplary images of surface maps of inserts obtained during image analysis of µCT images.

This enabled quantification of the porosity and gave additional valuable information of the surface areas during processing and analysis of the same image. This was of particular interest, since the absolute porosity of two inserts could potentially be the same, but the size of the pores and the corresponding surface area may still differ significantly.

The underlying release observed for the respective sample can therefore be explained more sensibly by considering multiple influencing factors.

3.2.8.3 Porosity caused by drying

As described in section 3.1.7, different drying conditions can greatly impact the porosity of the printed insert. To investigate this effect more thoroughly, 10 % LC-HCl loaded inserts were printed and dried at 25, 32.5 and 40 °C under atmospheric and reduced (500 mbar) pressure. The inserts were then analyzed in terms of porosity by µCT imaging and image analysis and subsequently subjected to dissolution studies for correlation.

As seen in Figure 49, the pores within the inserts seem to become larger when increasing the temperature or reducing the pressure during drying.

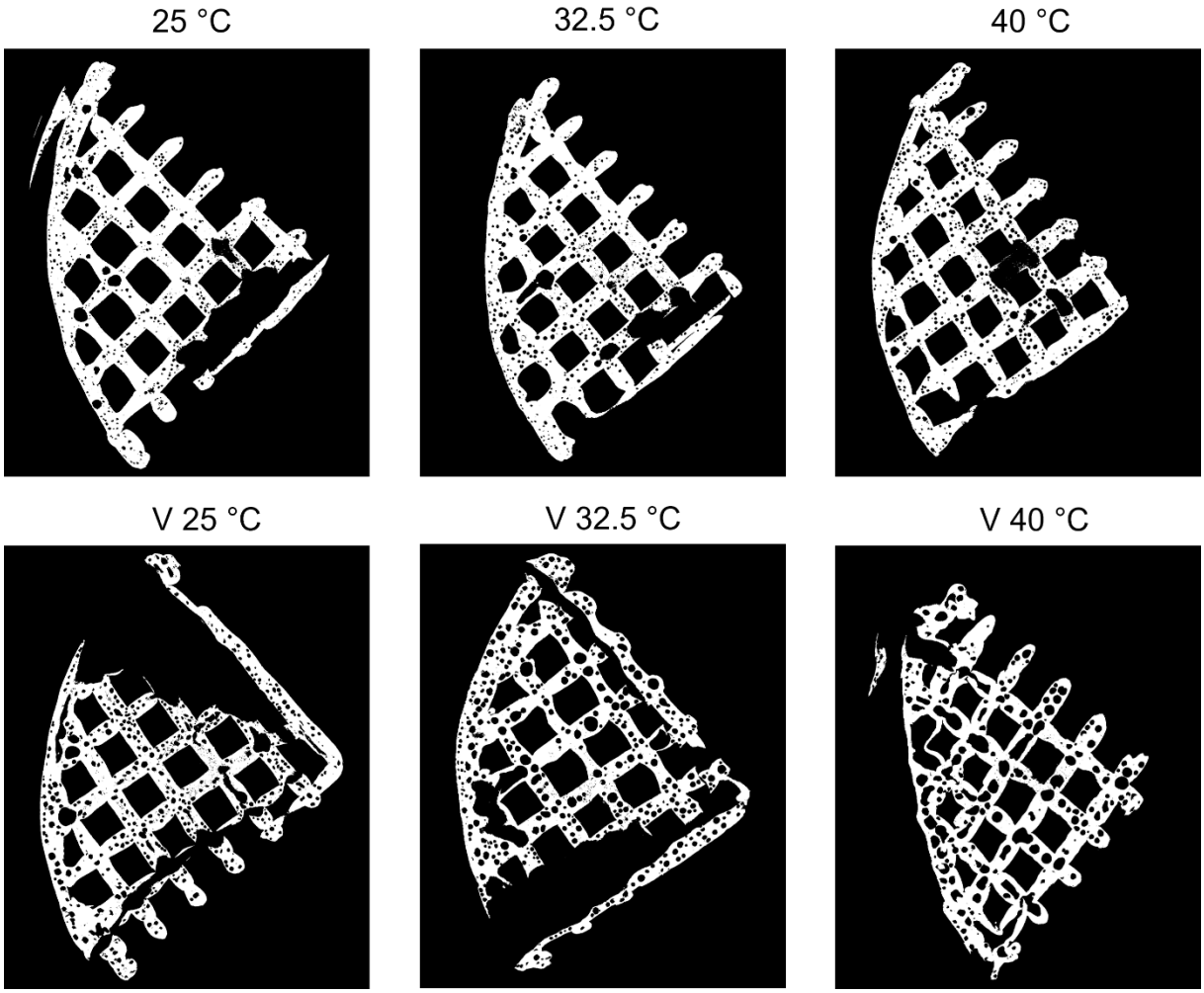

Figure 49. µCT images of inserts dried at different temperatures under atmospheric (top row) and reduced (bottom row, V: vacuum) pressure.

Apart from the visual evaluation, quantification of the porosity confirmed that within the same pressure condition, the porosity of the inserts before dissolution increased with increasing temperature (see Table 16).

Table 16. Characteristics of inserts dried under different conditions obtained via image analysis and dissolution studies (b: before dissolution, a: after dissolution); mean ± sd, n=3.

	25 °C	V 25 °C	32.5 °C	V 32.5 °C	40 °C	V 40 °C
Porosity b. [%]	3.49 ± 0.07	8.11 ± 0.36	5.06 ± 0.20	9.04 ± 2.21	6.69 ± 0.28	8.21 ± 3.54
Porosity a. [%]	3.39 ± 0.21	4.39 ± 0.21	3.36 ± 0.44	3.81 ± 0.41	2.82 ± 0.26	2.19 ± 0.08
SA/V b. [mm^{-1}]	6.88 ± 0.09	7.57 ± 0.33	6.84 ± 0.22	8.32 ± 0.48	7.14 ± 0.05	9.03 ± 0.54
SA/V a. [mm^{-1}]	8.58 ± 0.08	11.33 ± 0.15	9.21 ± 0.25	12.01 ± 0.21	9.88 ± 0.18	12.12 ± 0.51
$MDT_{80\%}$ [d]	1.62	0.55	1.19	0.59	0.92	0.72

Figure 50 shows a visual representation of the evaluation of pore volumes via image analysis. It revealed that the largest pore volumes expressed as the 99 % quantile were observed for the inserts dried under reduced pressure and with increased temperature. The mean pore volume expressed as the 50 % quantile revealed a larger pore volume under atmospheric pressure compared to reduced

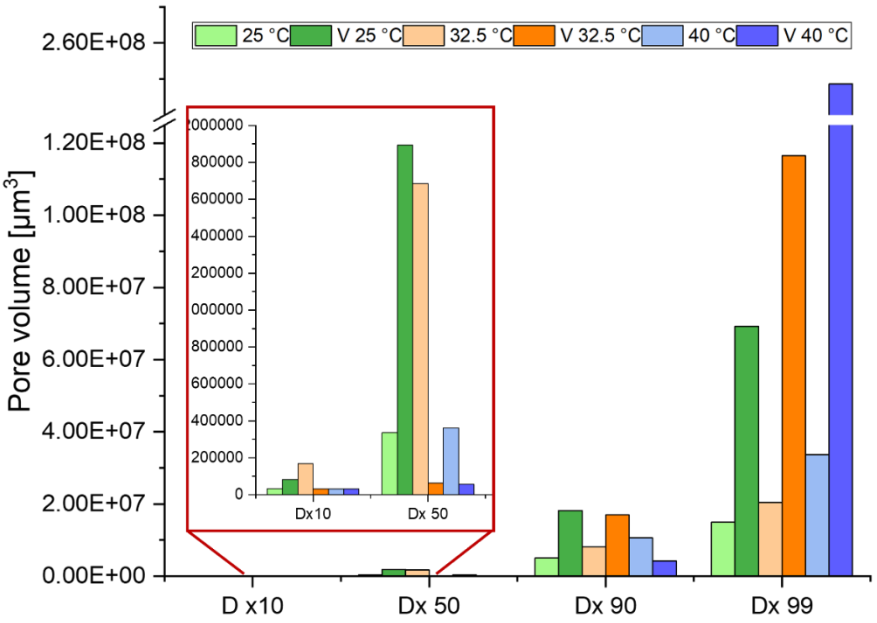

Figure 50. Pore volumes of inserts dried under atmospheric and reduced (V: vacuum) pressure at different temperatures.

pressure. This could suggest that the inserts dried under reduced pressure contained few very large pores and more smaller pores compared to those dried under atmospheric pressure. Possibly in this case, medium sized pores were combined to larger pores during sudden solvent evaporation and solidification of the polymeric matrix during drying. It must be stated, however, that the resolution of the images was limited to 20 µm, so that very small pores could not be detected and quantified adequately.

Under atmospheric pressure, porosity values between 3.49 (25 °C) and 6.69 (40 °C) % were obtained. For 25 °C and 32.5 °C these values nearly doubled when reducing the pressure to 500 mbar. For the

insert dried under reduced pressure at 40 °C the porosity did not significantly increase compared to 25 or 32.5 °C. However, for this drying condition a high variability was observed, which indicates that drying the inserts under this pressure/temperature condition did not lead to reproducible results possibly due to uncontrollable solvent evaporation and quick solidification of the matrix. After subjecting the inserts to dissolution studies, the porosity was decreased in all cases. This decrease was more pronounced for inserts dried under reduced pressure. A reduced porosity after dissolution was obtained because the pores that were formally only internal, have become accessible from outside and are therefore no longer counted towards the porosity. This may occur when API particles in close proximity to the pores are dissolved and leave behind new pores that now connect already existing pores. When this network eventually connects to the surface of the insert, the dissolution medium can readily enter the porous network and ingress into the matrix of the insert. This is also reflected in the SA/V ratios before and after dissolution.

The SA/V ratio of the inserts was determined via image analysis taking only surfaces into account that are directly accessible to the dissolution medium (excluding surfaces of internal pores). The SA/V ratios were lowest for inserts dried under atmospheric pressure and 25 or 32.5 °C (6.88 and 6.84 mm^{-1} respectively) and highest under reduced pressure at elevated temperature (9.03 mm^{-1} at 40 °C). Here, the SA/V ratio significantly increased after dissolution in all cases, which indicated that the surface area that is directly accessible from outside increased and was in accordance with the observations of the decreased porosity after dissolution.

The API release of the inserts was slowest for the inserts dried under atmospheric pressure and lowest investigated drying condition (see mean dissolution time for 80 % of API release ($MDT_{80\%}$) in Table 16). Under this condition the lowest porosity was found and one of the smallest SA/V ratios before and after dissolution. The internal porosity did not change significantly before and after dissolution and the increase in SA/V was comparably small. One explanation for this observation may be that in this case no continuous porous network was formed and water permeation into the matrix was therefore not accelerated substantially which led to a higher MDT. Possibly the expansion of the solvent gas bubbles inside the insert was only minimal during drying and the gentle drying condition allowed larger gas bubbles to escape the insert before solidification of the matrix took place. Therefore, the gas bubbles were spaced out within the insert and had enough distance between each other to avoid formation of a continuous network. For inserts dried under atmospheric pressure, the release was faster with increasing temperature and porosity. Within the same temperature, the release was faster with reduced pressure causing increased SA/V ratios and porosities.

For inserts dried under reduced pressure the release seemed to decrease with increased temperature which was in contrast to the inserts dries under atmospheric pressure and may have been caused by uncontrolled processes during drying and could be an interplay of various effects. While the porosity

slightly increased with increasing temperature and showed high variability, the slower release may have been attributed to the formed pores and their tortuosity but cannot be confirmed with certainty based on the obtained data.

It did however confirm that the optimal drying condition for sustained release included lower temperatures and atmospheric pressure and showed that drying under vacuum led to results with high variations.

3.2.8.4 Porosity caused by solvent content

The composition of the formulation can also have a significant impact on the resulting porosity of the inserts especially when solvents are used that may evaporate during drying and can leave behind pores within the insert's matrix. For this reason, formulations were prepared with varying solvent content and their porosity and release behavior investigated (see Table *36* for reference of composition and applied printing conditions).

As seen in the summarized results in Table 17, the porosity of the inserts with 7 % higher solvent content ("mS") was slightly higher than for the inserts prepared from the semi-solid formulation with less solvent ("regular").

Table 17. Characteristics of inserts with regular solvent content and more solvent (mS) obtained via image analysis and dissolution studies; mean ± sd, n=3.

	10 % mS	10 % regular
Porosity before [%]	3.86 ± 0.11	3.49 ± 0.07
Porosity after [%]	4.47 ± 0.17	3.39 ± 0.21
SA/V before [mm^{-1}]	8.12 ± 0.10	6.88 ± 0.09
SA/V after [mm^{-1}]	8.97 ± 0.02	8.58 ± 0.08
$MDT_{80\,\%}$ [d]	0.11	1.66

Additionally, the SA/V ratio of the inserts with higher solvent content in the printing ink was also higher (8.12 and 6.88 mm^{-1} respectively). As expected, this was reflected in the dissolution behavior of the inserts as well. In this case, the $MDT_{80\,\%}$ was much shorter. The higher solvent content in this case may have caused a rougher surface through evaporating solvent and could therefore be an explanation for the higher SA/V ratio before dissolution. This enabled easier penetration of the dissolution medium into the matrix of the insert and was possibly further facilitated by the higher porosity. This demonstrated that the solvent content of the starting formulation can have a high impact on the resulting inserts and should be kept minimal within the limits of obtaining printable formulations.

3.2.8.5 Porosity caused by suspended particles – drug load and particle size

Upon dissolution, the suspended API particles within the inserts will dissolve and leave behind pores that further accelerate the drug release by enabling medium penetration into the matrix of the insert (see section 3.2.6). The particle size of the API can thereby cause formation of smaller or larger pores. Depending on the particle size distribution of the particles within the insert, the pore size determination of the insert after dissolution may vary. Few large pores would thereby cause a smaller specific surface area than many smaller pores and potentially influence the drug release. Therefore, in the following experiment the API was sieved and particles below 160 µm were removed before incorporation into the printing ink.

Similarly, the drug load will also affect the porosity upon dissolution. Assuming the same particle size distribution, higher drug loads will cause higher porosity due to larger amounts of incorporated particles. After a certain drug load is achieved, it may even be the case that the percolation threshold is reached, forming large networks of pores and API particles. This would lead to fast and effective penetration of the dissolution medium into the core of the printed strands.

Table 18 summarizes the data obtained via image analysis and dissolution for the different inserts (see Table *36* for reference of composition).

Table 18. Characteristics of inserts with varying drug-load and sieved API (≥160 µm, 10% drug-load) obtained via image analysis and dissolution studies; mean ± sd, n=3.

	5 %	10 %	15 %	25 %	Sieve fraction
Porosity before [%]	3.01 ± 0.08	3.49 ± 0.07	5.7 ± 0.04	4.81 ± 0.04	3.79 ± 0.17
Porosity after [%]	3.89 ± 0.14	3.39 ± 0.21	1.8 ± 0.01	0.56 ± 0.03	3.75 ± 0.13
SA/V before [mm^{-1}]	6.72 ± 0.02	6.88 ± 0.09	5.8 ± 0.05	7.68 ± 0.17	7.31 ± 0.36
SA/V after [mm^{-1}]	8.01 ± 0.24	8.58 ± 0.08	15 ± 0.04	23.64 ± 0.66	9.70 ± 0.08
$MDT_{80\,\%}$ [d]	3.17	1.66	0.25	0.09	0.16

It can be seen that the porosity of the inserts also increased with increasing drug content. This is also visible in the exemplary µCT images in Figure 51, in which the inserts with 25 % LC-HCl (right) seem to contain more small pores than the 5 % drug-loaded insert (left). This may have occurred due to inclusion of air together with the API particles. In SEM images of the inserts, it could also be seen that the API particles are typically embedded in small pores within the matrix (see e.g. section 3.2.5.6 for reference). In case of more API particles, this would lead to more air being entrapped as well.

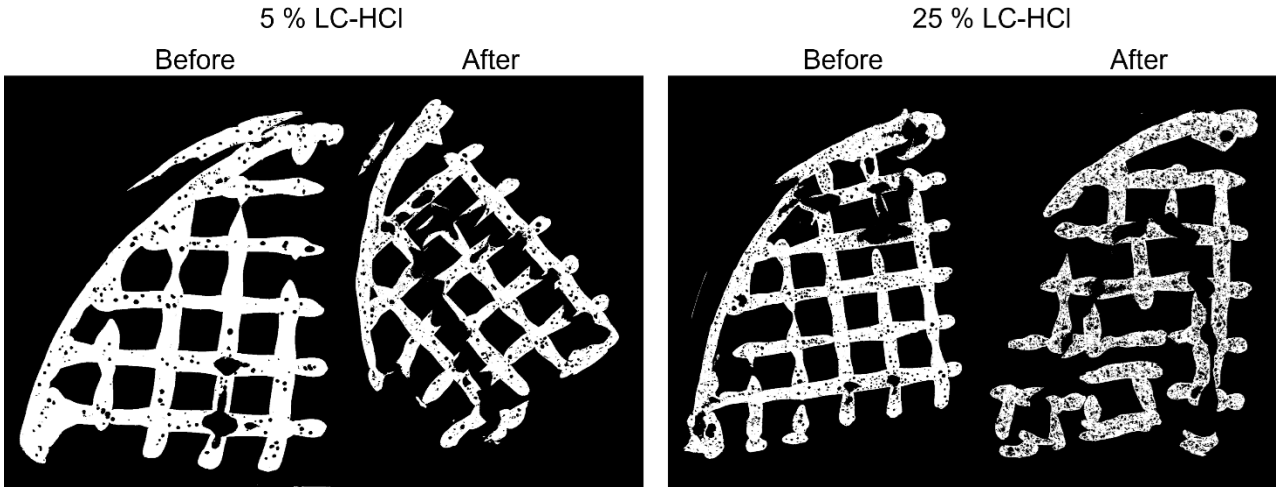

Figure 51. µCT images of 5 % (left) and 25 % (right) LC-HCl-loaded PCL inserts before and after dissolution studies.

The percolation threshold seemed to be reached around 15 % of drug load, which is visible in the high increase in SA/V ratios (5.80 and 7.68 mm^{-1} before and 15.0 and 23.64 mm^{-1} after dissolution for 15 and 25 % drug load respectively). This indicates that the surface area compared to its volume has largely increased due to the dissolution of the embedded API particles inside the matrix of the inserts. This seemingly caused the formation of continuous porous networks that are freely accessible to the dissolution medium and further enhance drug release (see respective $MDT_{80\%}$ values). While the SA/V ratio increased, the porosity after dissolution significantly decreased for these inserts, which is in accordance with the hypothesis that a continuous network was formed, since the porosity is determined by pores that are not accessible from outside.

The inserts prepared with the sieved API containing larger particles, exhibited a much faster drug release than the respective inserts prepared with non-sieved API ($MDT_{80\%}$ 0.16 and 1.66 respectively). In this case, the porosity and SA/V ratios before and after dissolution were a bit higher for the inserts containing larger API particles. One possible explanation for this may be that the larger API particles were able to entrap more air inside the matrix while the smaller particles could have been dissolved in the solvent and crystallized upon solvent evaporation without entrapping air inside the insert (c_s of LC-HCl in THF at 25 °C: 6 mg/mL).

The larger API particles could have also caused larger pores to be formed upon dissolution, which made penetration of the dissolution medium into the inserts easier. While in this case no indication is given for formation of large continuous pore-networks, it may have been the case that larger particles were found close to the surface of the insert and caused an enlarged surface area after dissolution that contributed to the faster overall release. Due to the high water solubility of LC-HCl, larger API particles did not cause a sustained release by slower dissolution of the particles. The effect on dissolution is therefore more likely to be based on the formation of pores and their geometry/ distribution within the matrix.

3.2.9 Optimization of biodegradable insert

3.2.9.1 Polymer selection and characterization

Sine the PCL inserts only showed degradation below 5 % under the investigated experimental conditions, the benefit of using this polymer as degradable system would be minimal. Considering an application time of 2-4 weeks, the insert would hardly be degraded by the time the next insert would be applied. This would imply that the first insert would also have to be removed cystoscopically or be broken down into small pieces that could be excreted during voiding.

Therefore, other polymers were screened that would be able to degrade faster than PCL. TrCl was chosen as model API for the optimization of the biodegradable DDD, since it was shown in previous studies to be the most challenging API for achieving a sustained release.

The biodegradable polymers poly(D,L-lactide-co-glycolide) (PLGA), poly(L-lactide-co-ε-caprolactone) (PLCL) and Poly(D,L-lactide) (PDLLA) were investigated regarding their degradability. Since only little polymer amounts were available for screening trials, small polymer rods were prepared with the same SA/V ratio by dissolving the polymers and pouring them into a mold. The resulting cylindrical rods had a diameter of 5 mm and length of 1 cm. During the degradation studies, the pH of the media in which the samples were stored throughout the experiments was initially 6.93 and dropped for all investigated polymers over time. After week 4 of the study the pH of the demineralized water containing the PLGA samples was 4.07, for PDLLA 5.60 and for PLCL 4.02. This suggested acidic degradation byproducts (lactic and/or glycolic acid) to have formed during the studies, which could accelerate further degradation processes in terms of acid catalyzed ester hydrolysis (Siepmann et al., 2005).

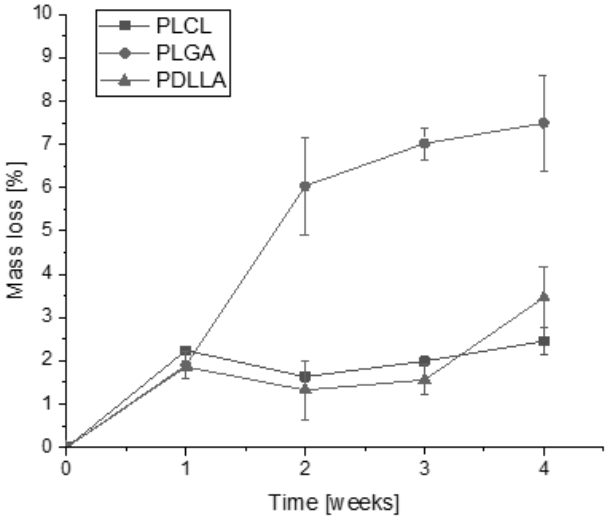

Figure 52. Mass loss of new biodegradable polymers in dem. water at 25 °C; mean ± sd, n=3.

The results show an overall slow degradation for all studied polymers that reached a mass loss of 2.5 % for PLCL and 3.5 % for PDLLA (see Figure 52). PLGA showed the highest mass loss of approximately 7.5 % and would be the most promising polymer to degrade within the desired time frame. However, it is assumed that the degradation rate of the inserts would likely be higher due to the enlarged surface area of the net-shaped inserts, the smaller strand diameter and degradation at 37 °C.

The results of the contact angle measurements are summarized in Table 19 and show similar wettability for all polymers.

Table 19. Results of contact angle measurements of dem. water on films of new biodegradable polymers and PCL after 1 and 60 s; mean ± sd, n=3.

Contact angle [°]	1 s	60 s
PLGA	68.5 ± 1.7	67.5 ± 1.5
PDLLA	68.0 ± 1.7	66.8 ± 1.3
PLCL	65.7 ± 0.7	65.0 ± 0.7
PCL	57.6 ± 1.9	57.6 ± 1.5

After 60 s of measurement, the most favorable wettability for a sustained drug delivery application was exhibited by PLGA with the largest contact angle of 67.5°. However, there was no significant difference observed to PDLLA. A larger contact angle suggests that water cannot permeate into the matrix easily and would therefore cause the drug crystals within the polymeric matrix to be dissolved later. Overall, it can be said that the wettability of the newly studied polymers was lower than the wettability of PCL, which was desired for the purpose of the new inserts. PLGA was therefore selected as the most promising candidate because of its favorable wettability and degradation.

Due to PLGA's brittle nature, it was essential to incorporate a plasticizer to obtain flexible inserts. For this purpose, various plasticizers were screened by manufacturing PLGA films and evaluating them according to feasibility of obtaining homogeneous films, stickiness of the obtained film and brittleness after exposure to water (Table 20). Some of the films were flexible at first but became brittle after storing them in dem. water due to the plasticizer being washed out of the film.

Table 20. Results of evaluation of plasticized PLGA films (+: favorable, -: non favorable).

Plasticizer	Incorporation feasible	Stickiness	Brittleness after exposure to water
PEG 400	+	-	-
PEG 1500	-	-	-
Triethyl citrate (TEC)	+	-	-
Acetyl-tributyl-citrate (ATBC)	+	+/-	+
Dibutyl sebacate (DBS)	+	-	-
Triacetin (TA)	+	-	-
Medium-chain triglycerides (MCT)	+	-	-
PLCL	+	+/-	+

ATBC and PLCL could successfully be incorporated into the PLGA-formulation and gave the dried films the sufficient flexibility to be rolled up without breakage. Incorporation of PLCL could potentially negatively influence the degradation behavior of the polymeric matrix, since it degraded slower than PLGA, but was considered a viable candidate due to the quality of the obtained film. Therefore, ATBC and PLCL were further considered for formulation development.

Additionally, a new PEG-terminated PCL copolymer (PCL-PEG) was selected for development of the new biodegradable inserts. The addition of the PEG-component may thereby enhance the degradation while having plasticizing effects on the polymer (Kwon et al., 2013). Film-casting trials showed that no additional plasticizer was required to obtain flexible films and showed no stickiness or brittleness after exposure to water. The PCL-PEG copolymer was further chosen because the hydrophilic PEG-unit could potentially better entrap the hydrophilic API TrCl and therefore prolong the drug release.

3.2.9.2 Dissolution testing

Dissolution studies revealed that PCL-PEG was favorable to prolong the release of TrCl while the PLGA-PLCL and PLGA-ATBC formulations were not able to retain the API for a prolonged time (see Figure 53).

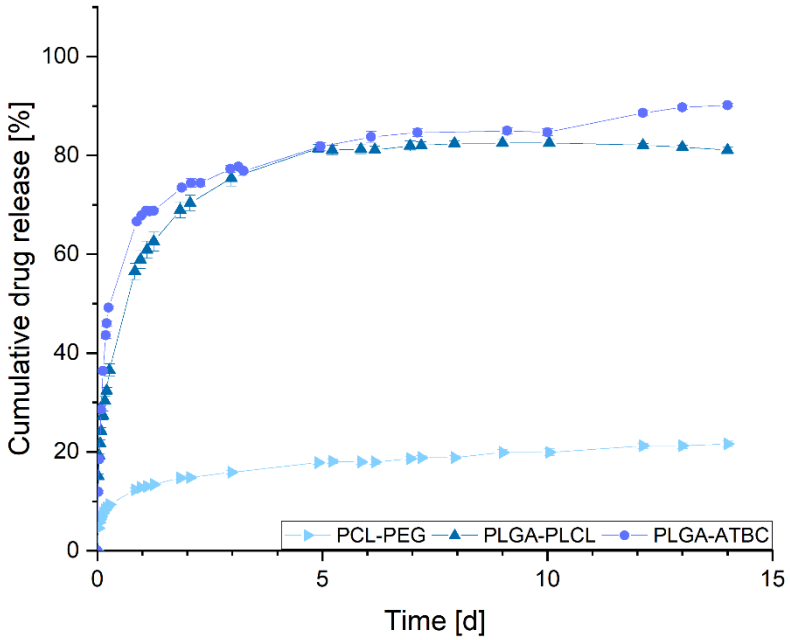

Figure 53. Dissolution profiles of TrCl-loaded biodegradable inserts in 900 mL dem. water at 100 rpm; mean ± sd, n=3.

Degradation of the matrix occurred much faster for the PLGA inserts, which was visible in the inserts being very brittle and falling apart after dissolution as well as a steep drop in pH of the dissolution medium (pH 3.22 measured after 2 weeks of dissolution). The low pH can then cause autocatalytic degradation of the remaining matrix and so accelerate overall degradation while enhancing drug release (Siepmann et al., 2005).

Based on the obtained release data, PCL-PEG seemed to be a suitable candidate for further development of the biodegradable inserts containing highly hydrophilic APIs. The degradation of the PCL-PEG insert was with approximately 9 % after two weeks doubled compared to the PCL inserts. Considering that until then only approximately 22 % of the API was released, the insert would be able to remain for several weeks or months within the bladder before the API reservoir would be completely depleted. This, however, would assume a constant release rate. The calculated release rate based on an average daily bladder filling of an adult was approx. 0.45 µg/mL and still too low for the targeted release of at least 1 µg/mL. Based on previous experiments to modify the release, the next step included modification of the insert's geometry.

3.2.9.3 Modification of drug release via geometry

As seen in chapter 3.2.9.2, the release of the new biodegradable insert was too low. Therefore, different numbers of layers were printed to enhance the release by increasing the SA/V ratio of the insert.

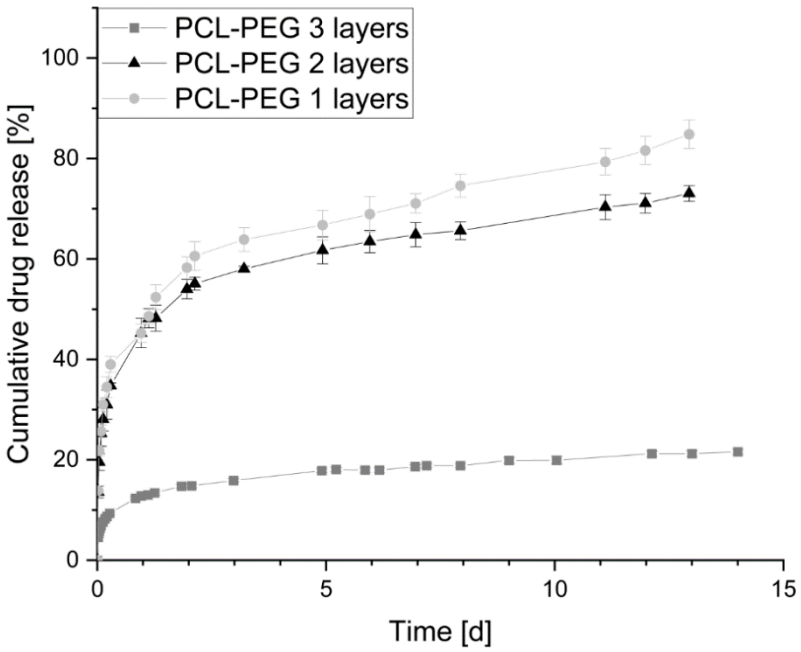

Figure 54. Dissolution curves of TrCl-loaded PCL-PEG inserts with different numbers of printed layers in 900 mL dem. water at 100 rpm; mean ± sd, n=3.

As seen in Figure 54, the release was significantly enhanced when 1 or 2 layers were printed compared to three layers. Fastest release was thereby achieved for the insert containing only 1 layer. In this case around 83 % of API was released after 13 days. However, since less formulation is printed for this geometry, the overall drug load of the insert was comparably low and the absolute amount of released API was still too low (see Table 21).

Table 21. Drug release rates and drug loads of TrCl-loaded PCL-PEG inserts printed with different numbers of layers.

Number of layers printed	Drug release [%/d]	Drug release [µg/mL]	Drug-load per insert [mg]
1 layer	2.25 (d 2-13)	0.69 (d 2-13)	45
2 layers	1.66 (d 2-13)	1.05 (d 2-13)	95
3 layers	0.52 (d 3-14)	0.45 (d 3-14)	130

The insert printed with 2 layers showed a slightly decreased release compared to the insert with 1 layer, but had a higher absolute drug release, since the overall drug load was higher here. In this case, it was feasible to achieve the targeted concentration of 1 µg/mL after 2 days of dissolution testing.

This indicated that the new biodegradable polymer PCL-PEG was suitable to release the hydrophilic API TrCl over a prolonged period while exhibiting an enhanced degradation. Extended studies would be necessary to determine the matrix erosion of the insert after all of the API is released.

3.2.10 Release rates of drug loaded inserts

The previous experiments have demonstrated the possibility of fine-tuning the release rates of the intravesical inserts based on polymer, API, geometry and drug load.

For a given API a wide range of release rates may be achieved depending on the desired application (see Table 22). After an initial phase of high release attributed to the large surface area of the inserts, a slower release is typically followed over the course of several days or weeks. In some cases, the insert released the API too fast and no sustained release could be achieved over the course of several weeks (e.g. for drug-loads above 15 %).

Table 22. Drug release phases of various inserts calculated from nearly linear regions ($R^2 \geq 0.98$) of cumulative release profiles for average bladder filling level of adult human. All inserts printed with 3 layers, unless stated otherwise.

Insert	Drug release phase 1 (µg/mL)	Drug release phase 2 (µg/mL)
PCL		
5 % LC-HCl	1.65 (d 3 - 7)	0.7 (d 7 - 16)
10 % LC-HCl	2.78 (d 3 - 6)	1.04 (d 6 - 14)
15 % LC-HCl	16.54 (d 0.8 - 2.25)	-
10 % LC-HCl 2 layers	1.3 (d 3 - 6)	0.33 (d 6 - 14)
10 % LC-HCl 1 layer	5.7 (d 0.5 - 1)	0.39 (d 2.75 - 6.75)
No infill	0.9 (d 2 - 8)	0.39 (d 8 - 14)
Double contour	1.1 (d 3 - 14)	-
10 % HCT	2.9 (d 3 - 14)	1.78 (d 14- 21)
10 % TrCl	27.27 (h 4.5 – 27.5)	-
PCL-PEG		
10 % TrCl 3 layers	0.45 (d 2 - 14)	-
10 % TrCl 2 layers	1.05 (d 2 - 13)	-
10 % TrCl 1 layers	0.69 (d 2 - 13)	-
EVA		
5 % LC-HCl	0.96 (d 4 - 28)	-
10 % LC-HCl	5.29 (d 1 - 5)	2.71 (d 5 - 15)
15 % LC-HCl	7.20 (d 1-5)	3.43 (d 6-12)
10 % TrCl	1.18 (d 3 - 30)	-
10 % HCT	0.55 (d 2 - 14)	-

For TrCl, the desired drug release was achieved for the 10 % drug-loaded PCL-PEG insert with 2 layers and the 10 % drug-loaded EVA insert with 3 layers. Although not clinically relevant, similar release rates could be achieved for LC-HCl for the 5 and 10 % drug loaded inserts for certain time periods. For the 10 % LC-HCl loaded PCL insert, this release was obtained for the insert with double contour and no

infill for an extended time between day 3 -14 of dissolution testing. As these values are only based on mathematical calculations, their verification would still have to take place in in-vivo models.
As reported in the literature, a release of approximately 130 – 400 mg of LC-HCl over the course of 2 weeks was proven to be efficient to relieve symptoms of bladder pain syndrome (Nickel et al., 2012). This could theoretically be realized by the 10 and 15 % drug loaded EVA insert and by the 10 % loaded PCL insert.
For the HCT inserts, no clinically relevant concentrations are known since the API is not intended for local application in the urinary bladder. Its incorporation into the inserts did however demonstrate that the release was significantly slower compared to the freely water-soluble APIs. The drug-release of such poorly soluble APIs could potentially be modified by printing different geometries with larger SA/V ratios or by introduction of pore-forming agents (see section 3.2.4).

3.2.11 Short-term stability study for TrCl-loaded inserts

3.2.11.1 Introduction

The targeted release of 1 µg/mL TrCl for effective therapy could be realized by the non-degradable EVA insert for a drug load of 10 % and 3 printed layers. For the degradable insert this was achieved by the PCL-PEG polymer matrix with a 10 % drug load and 2 layers.
The on-demand nature of 3D-printing allows drug delivery devices to be manufactured according to their need in small batches. In the future it could be an option to have compounding pharmacies or hospital pharmacies manufacture medicines as they are needed specifically for a designated patient. Nevertheless, it is of interest to understand how long a DDD remains stable and safe for administration in order to ensure a certain shelf-life and applicability. This opens up the possibility to manufacture medicines in advance and cut down on production times and material consumption.
Therefore, a short-term stability study was performed to investigate the inserts' stability over the course of one month under ambient conditions and stress conditions at 40 °C and 75 % relative humidity. Their mechanical properties, morphology and dissolution were investigated as some of the main critical quality attributes.

3.2.11.2 Evaluation of the morphology

The morphology of the samples was examined via SEM to determine whether any changes occurred during storage that may indicate modifications of the insert's structure and integrity. In Figure 55 and Figure 56 the cross-sections and surfaces of the TrCl-loaded inserts showed that no visible change had taken place during storage. For EVA, the surfaces of the inserts looked smooth with a few API particles visible for all samples. The cross-sections also revealed a smooth and homogeneous matrix with several pores containing API particles. The insert stored at 40 °C and 75 % relative humidity seemed slightly

rougher possibly due to presence of more small particles. It is unclear, however, if this could have been caused by re-crystallization of the API particles over time due to the elevated temperature and humidity that may have increased mobility of the API within the matrix.

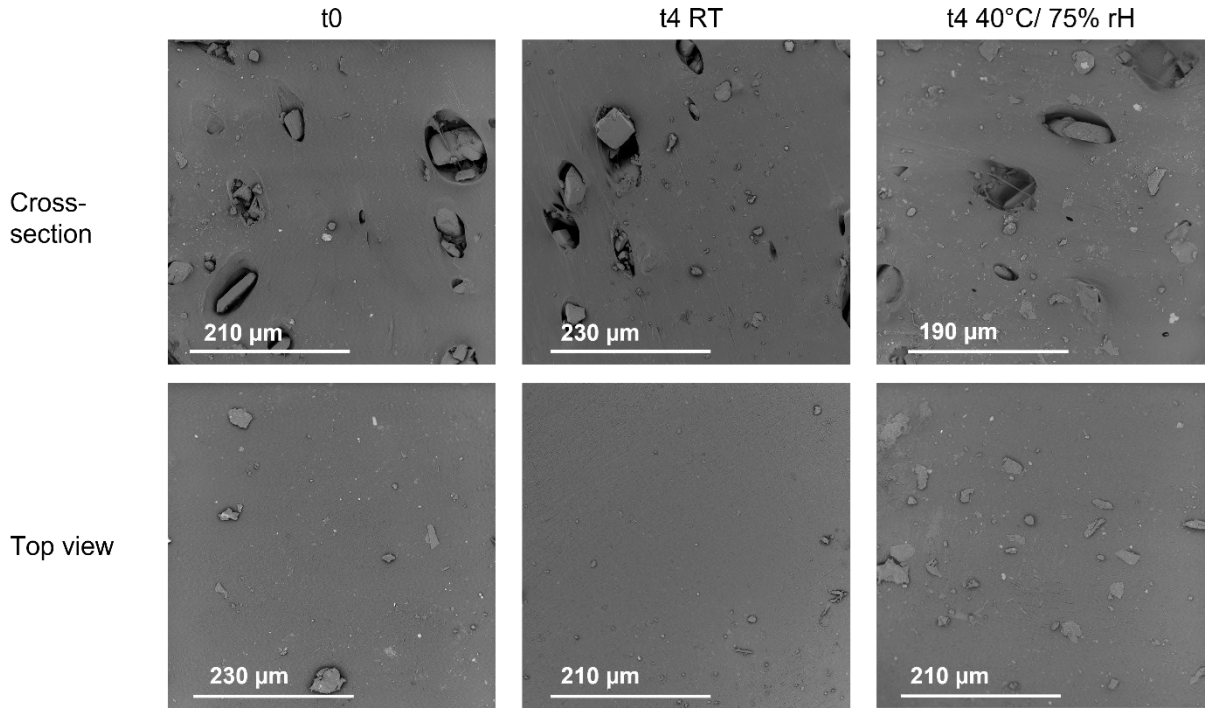

Figure 55. SEM images of cross-sections (top row) and top view (bottom row) of TrCl-loaded EVA inserts at the beginning of short-term stability studies (t0) and after 4 weeks (t4) of storage at ambient conditions (RT: room temperature) and at 40 °C/75 % relative humidity (rH).

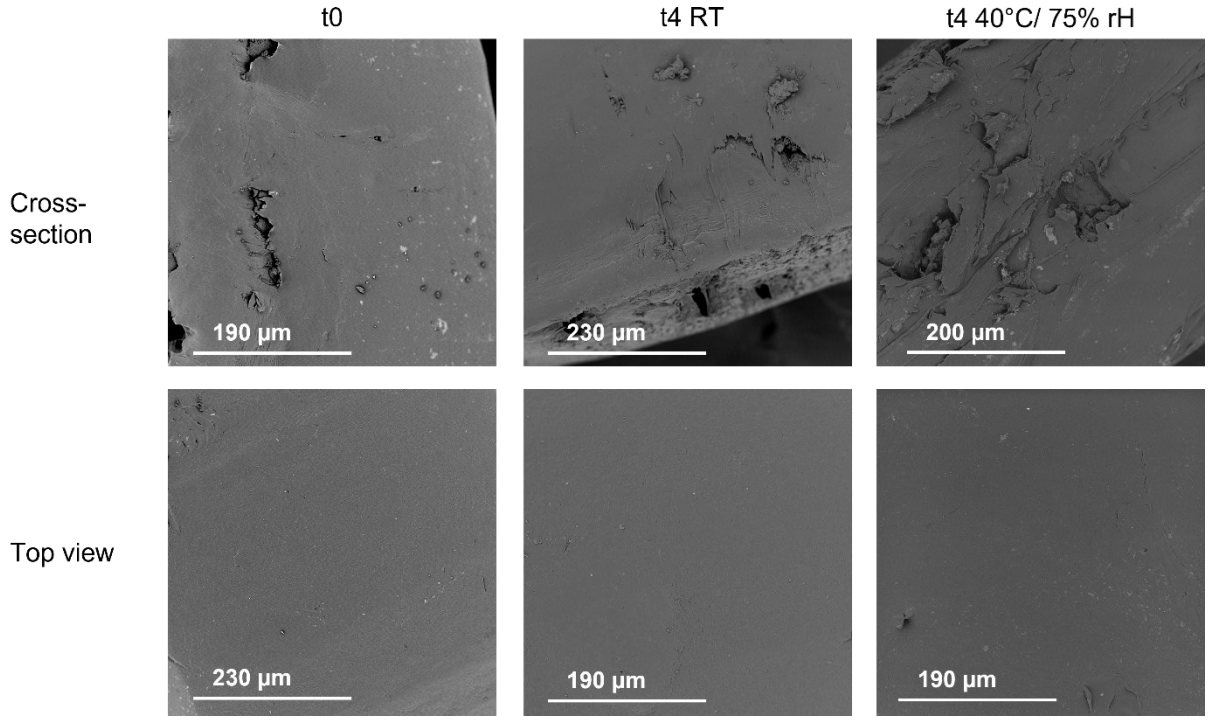

Figure 56. SEM images of cross-sections (top row) and top view (bottom row) of TrCl-loaded PCL-PEG inserts at the beginning of short-term stability studies (t0) and after 4 weeks (t4) of storage at ambient conditions (RT: room temperature) and at 40 °C/75 % relative humidity (rH).

For the PCL-PEG inserts, the surfaces of the inserts also seemed smooth without any pores or API particles visible. The cross-sections looked similar under all storage conditions and showed a smooth matrix with few small pores and API particles visible. No change in morphology was apparent for these samples during storage indicating that both inserts seem stable for one month and stress conditions did not have any macroscopic effects.

3.2.11.3 Mechanical properties

Mechanical properties were investigated by printing the semi-solid formulations into dumbbell-shaped specimen according to DIN EN ISO 527 and subjecting them to tensile tests. The test was used to compare the properties of the formulations during storage under different conditions. This was done to determine whether the flexibility of the final inserts could be ensured for a certain period of time since it was considered a critical quality attribute with regards to their applicability. A significant loss of elasticity could lead to inserts that no longer would be flexible enough to be coiled up for administration via urinary catheter.

The obtained force-distance diagrams were converted to stress-strain curves to determine the Young's modulus (YM) as the slope of the in the linear region of the curve.
During the tests, it became apparent that the EVA-samples were more flexible than the PCL-PEG samples by comparing the respective YM (see Figure 57).

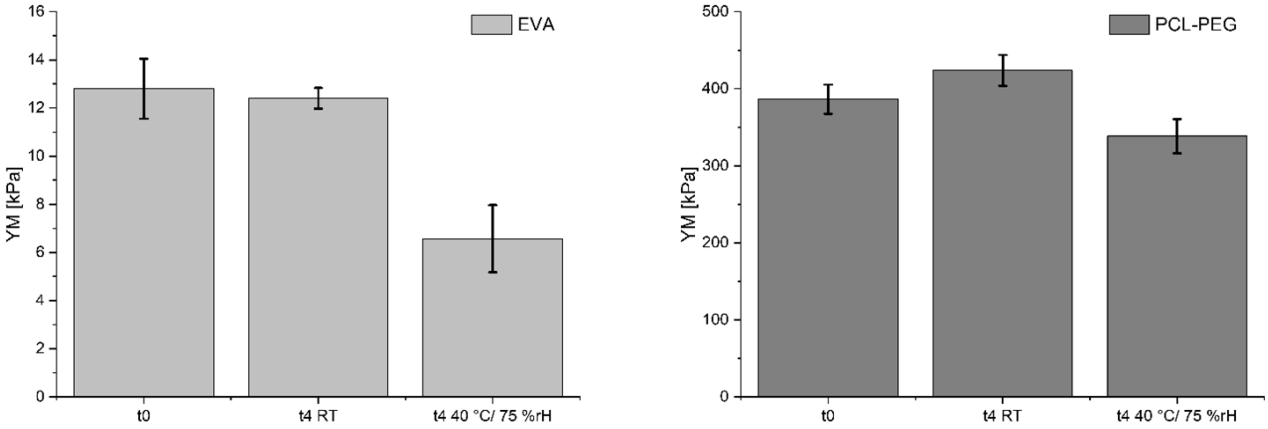

Figure 57. YM for TrCl-loaded EVA (left) and PCL-PEG (right) samples during short-term stability studies, mean ± sd, n=3.

Further, the EVA films did not rupture even at maximum displacement of the measurement probe, while the PCL-PEG films ruptured during the test.
For the EVA samples, no significant change in YM was observed during 4 weeks of storage at ambient conditions. However, after 4 weeks of storage at 45 °C and 75 % rH, the average value of the YM dropped from 12.8 to 6.6 kPa, indicating that the material became even more soft over time. This may

be related to the high moisture content of the atmosphere, that may have led to some water uptake and could have had a plasticizing effect.

For the PCL-PEG samples, the mean value of the YM slightly increased from 393.7 kPa to 423.7 kPa during storage at ambient conditions. However, due to some variability in the results, this difference was not significant. Also in this case, there was a decline in the YM after storing the samples under stress conditions (338.1 kPa after 4 weeks).

These results indicate that the formulations did not lose their flexibility over the course of 4 weeks under ambient conditions. In case of stress conditions, a decrease in YM was observed in both cases that could have been caused by water uptake, as the samples were stored in open Petri-dishes. Storage in a closed container or sealed packaging would be of interest to determine whether the stability would be given in this case also under stress conditions. Nevertheless, it can be said that integrity of both formulations did not seem compromised after prolonged storage under ambient conditions and their applicability would likely still be given.

3.2.11.4 Dissolution testing

Dissolution studies revealed no change in release behavior for the TrCl-loaded EVA inserts after 4 weeks of storage at ambient conditions. Storing the inserts under stress conditions, however, led to an enhanced release. In this case, after two weeks of dissolution testing, 53.5 % of API was released as opposed to 43.0 % for the sample tested at the start of storage (see Figure 58).

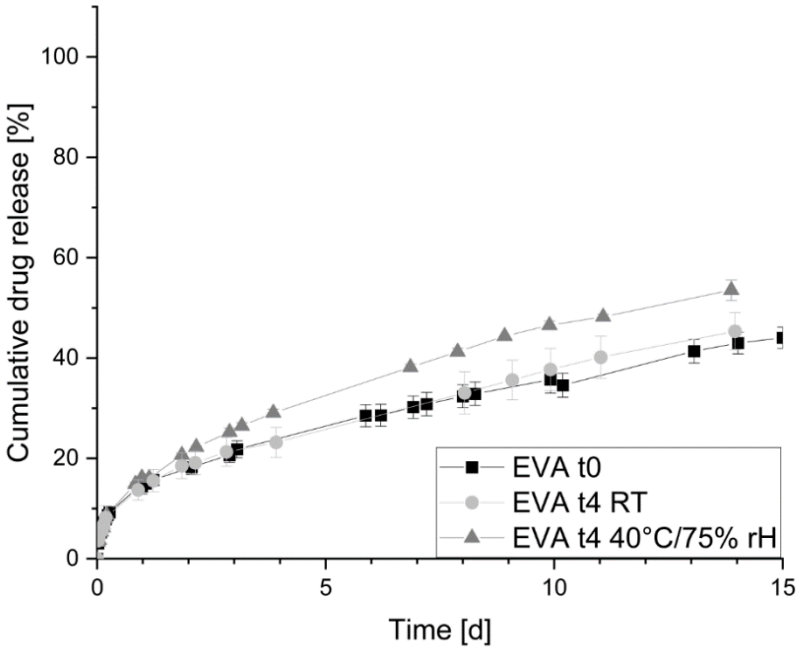

Figure 58. Dissolution profiles of TrCl-loaded EVA inserts at the start of short-term stability studies (t0) and after 4 weeks (t4) at ambient (RT: room temperature) and stress (40 °C/75 % rH) conditions; in 900 mL dem. water at 100 rpm; mean ± sd, n=3.

This may have occurred due to the high humidity and temperature leading to water uptake of the inserts. On the one hand side this may have had some plasticizing effects and increased the overall mobility on the API, on the other hand it may have led to partial dissolution of the embedded API crystals that were then faster released during dissolution studies.

To further compare the dissolution profiles, the similarity factor f_2 was calculated. A f_2 value of around 100 indicates identical curves, while a value of 50 or more indicates that the values differ by max. 10%. Values below 50 indicate that the curves can no longer be considered similar (Costa and Sousa Lobo, 2001; Shah et al., 1998). For the release curves obtained by inserts stored under stress conditions and those tested at the start of storage, a f_2 value of 66 was obtained, which indicates that the curves can still be considered similar. However, this value should be interpreted with caution, since the sample size used to determine the similarity factor was small (n=3).

The PCL-PEG insert showed a similar trend regarding the observed release at different storage conditions (see Figure 59). Also in this case, no relevant difference was seen for the inserts tested at the start of the stability study and after 4 weeks of storage under ambient conditions. The samples stored at increased temperature and humidity displayed an enhanced release, reaching approx. 85 % of drug release compared to 73 % at the start of storage. This was further demonstrated by determining the similarity factor f_2. For the curves obtained at the start of storage and after 4 weeks storage under stress conditions, a f_2 value of 47 was obtained, which indicates that the curves differed substantially.

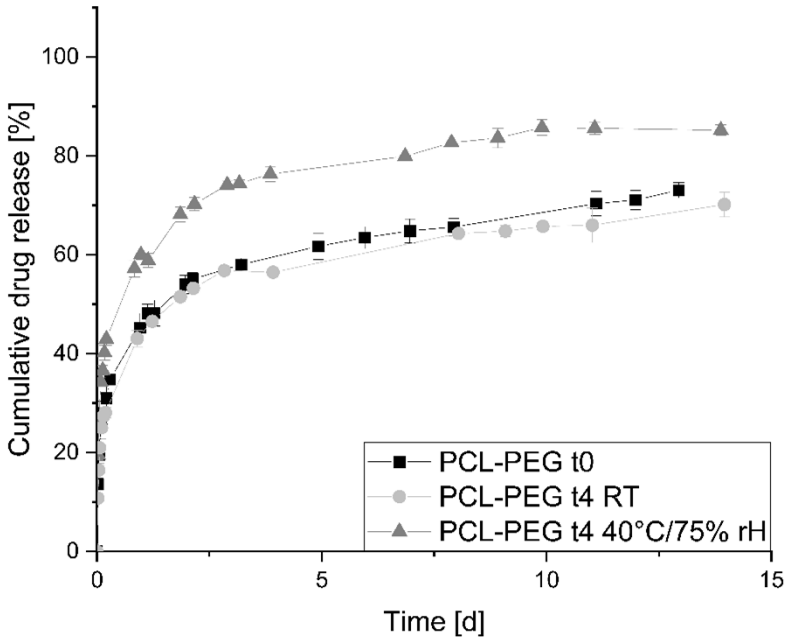

Figure 59. Dissolution profiles of TrCl-loaded PCL-PEG inserts at the start of short-term stability studies (t0) and after 4 weeks (t4) at ambient (RT: room temperature) and stress (40 °C/75 % rH) conditions; in 900 mL dem. water at 100 rpm; mean ± sd, n=3.

It may therefore be concluded, that the printed TrCl inserts seemed to be stable during 4 weeks of storage at ambient conditions. Longer storage and storage under accelerated conditions could possibly be acceptable in case water-impermeable packaging would be used and would have to be investigated in the future. Since the inserts were stored in open Petri-dishes the short-term stability studies only considered storage under worst case conditions that would not be applicable for a final dosage form or drug product. It did demonstrate, however, that the inserts would still be applicable after 4 weeks of storage at room temperature without alteration in morphology, mechanical properties, or dissolution profile. They would therefore not have to be administered directly after printing, which could save time and material consumption in real-life settings when batches could be manufactured that include more than just one applicable dose.

3.2.12 Summary

It was demonstrated in this chapter, that PAM-printing offers a viable method to develop flexible drug-loaded inserts for a long-term presence within the urinary bladder. It was feasible to incorporate freely soluble APIs such as LC-HCl or TrCl as well as the poorly soluble HCT and achieve sustained release properties over the course of up to several weeks depending on the used polymer-API combination. Raman measurements indicated that the release of the API was not only depending on the solubility in the dissolution medium but also on formation of larger API clusters/particles within the matrix of the printed inserts.

The degradation of the PCL inserts was found to be minimal under the investigated experimental conditions and could potentially pose a challenge for its applicability in case of frequently repeated administrations. In this case and in case of the non-degradable DDD, the inserts would likely have to be removed cystoscopically before inserting the next one. Therefore, further studies investigating polymers with a more rapid degradation were conducted that revealed PCL-PEG as suitable candidate.

Investigations regarding geometry and drug load indicated the possibility to tailor the drug release according to the required dose or intended application duration. Faster release rates were observed for high drug loads due to the formation of larger porous networks and slower release rates for inserts with more layers or double contour without infill due to the lower surface-area to volume ratio. It was feasible to develop intravesical inserts for a sustained release of the clinically relevant APIs TrCl and LC-HCl within release rates that were previously reported to be effective.

Evaluation of porosity and SA/V ratios of LC-HCl-loaded PCL inserts showed that drug release was widely influenced by drying conditions, drug load, particle size of the incorporated API and solvent content of the semi-solid printing formulations. It underlined that the release can be affected by

multiple factors such as porosity and its increase or decrease during dissolution together with changes in SA/V ratios as well as pore sizes and possibly tortuosity of the pores.

Short-term stability studies showed that the degradable PCL-PEG- and non-degradable EVA-inserts releasing TrCl in clinically relevant concentration ranges were suitable for storage up to one month under ambient conditions. However, longer storage in sealed containers that have a low permeability for water vapor could likely be possible. Although 3D-printing is commonly known as on-demand technology, storage of the developed DDD could be cost- and time-efficient during manufacturing and was therefore considered beneficial.

3.3 Development of a biopharmaceutical bladder model

3.3.1 Introduction and objectives

For determination of drug release from intravesical preparations so far only conventional pharmacopeia apparatuses are available, that are vastly different from the conditions within the urinary bladder and there is no standardized compendial method available yet (Brown et al., 2011; Ph. Eur. 10, 2020b, 2020c; Siewert et al., 2003). Steady production of urine, interindividual differences in patients, pathophysiological conditions and frequent voiding can change the current concentration of the API within the bladder throughout the course of treatment. This makes determination of drug concentrations at the target site particularly difficult with the conventional setups. Evaluation of the effectiveness of local drug therapy is therefore challenging and mostly based on assumptions or mathematical calculations when in-vivo tests have not been performed.

Hence, the aim of the following chapters was to develop a biopharmaceutically relevant bladder model to determine the release behaviours of the previously developed intravesical inserts under physiological conditions.

3.3.2 Concept

Figure 60 shows a sketch of the initial concept for the bladder model.

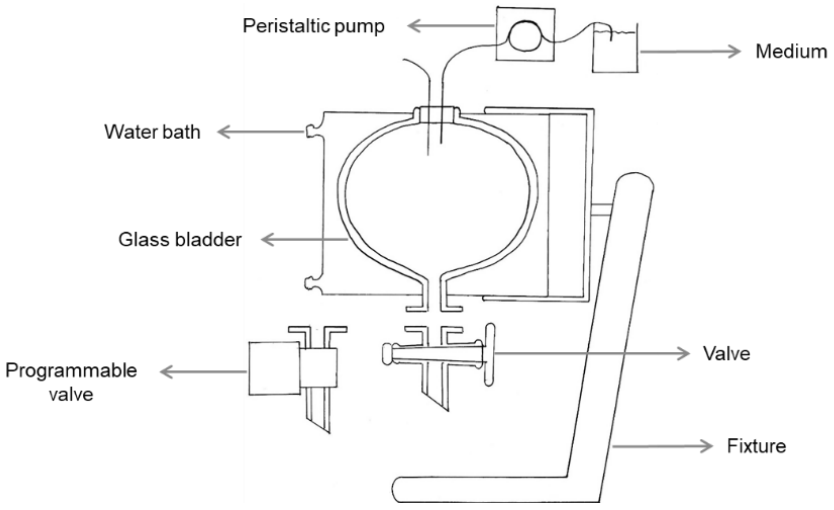

Figure 60. Sketch of bladder model designed for dissolution testing of intravesical inserts with desired components for mimicking physiological conditions.

The general concept was to develop a model that incorporates anatomical features of an adult human and is able to depict physiological conditions described in the literature. Further, it was desired that the model would be variable and allow dissolution conditions to be adapted and cover a wide range of possible conditions. It was important to include certain programmable components for the model to be operated automated and reproducible. Therefore, the valves were designed to be interchangeable,

so that they could be operated manually for initial trials and later to be programmed to open at pre-determined timepoints. This would enable the dissolution studies to be performed over the course of several days without the need for an operator to open the valves manually.

A pump was required to deliver the dissolution medium to the bladder with low flow rates according to the steady urine production in humans. As these flow rates are physiologically known to be under circadian control, the model should be able to account for this as well with different flow rates during day- and nighttime intervals. To mimic body temperature, the dissolution vessels would need to be connected to some kind of temperature controlling system. These vessels also needed to be customized according to anatomical features and include an outlet for drainage of the dissolution medium in analogy to the human urethra. This was important to allow the insertion process of the inserts to be mimicked as well. For this reason, it was also essential for the valves to be able to be dismounted for accessibility of the model urethra. All of these components needed to allow determination of local API concentrations at pre-defined time-points within variable operating conditions of the model.

3.3.3 Physiological considerations and model components

The model components of the bladder model were selected and designed carefully to match the conditions of an average adult (see Table 23).

Table 23. Components of the bladder model according to physiological conditions in human beings.

Biological aspect	Model component	Specification(s)
Urinal flow	Programmable peristaltic pump	1.0 mL/min flowrate during 16 h daytime interval 0.5 mL/min flowrate during 8 h nighttime interval
Urine	Purified water	Total volume of 1200 mL in 24 h
Bladder	Glass sphere	Volume: 1 L
Urethra	Defined outlet	Diameter: 8 mm, length: 5 cm
Voiding mechanism	Programmable valve	Voiding after 240 mL during daytime No voiding mechanism during nighttime
Body temperature	Water bath	37 ± 0.5 °C
Movement	Shaker-platform	40 – 45 rpm during daytime 0 rpm during nighttime

The selected dimensions of the model components mimicking the urinary bladder and urethra as well as flow rates and simulated voidings were derived from average values of healthy humans reported in the literature (Cima et al., 2014; Vaupel et al., 2015; Wyndaele, 1998).

The urinal flow was simulated by using a peristaltic pump with different flowrates according to the respective time-intervals that transfers the dissolution medium into the dissolution vessels.

These vessels were realized by glass bladders with urethra and were custom-made to match the physiology of an average adult (Lippert et al., 2010; Mahadevan, 2019). Magnetic valves were used to depict the voiding mechanism by draining the medium inside the bladder and could be freely adapted according to the desired frequency. They were attached via clamp connection below the outlet of the glass bladders at the end of the model urethra. To ensure constant temperature within the bladders, they were surrounded by customized water baths operated via thermostat. Movement of the patient was mimicked by placing the model onto a shaker-platform that could be programmed to move at different speeds during day- and nighttime intervals. The pump as well as the valves were controlled by a custom-built control unit.

3.3.4 Prototype and final construction

Based on the aforementioned components, a prototype was constructed for evaluation of the model's suitability for determining drug release (see Figure 61). Before the model could be operated automatically, manual drainage was performed by the interchangeable valves. The fixture holding the jacketed glass bladder was tiltable and could secure the bladder in different angles. This was designed to potentially investigate influences of bladder position (e.g. when a patient would be bedridden and therefore, the bladder would be in an 90° angle).

When connecting all the components, it was found that the model was suitable for dissolution studies and sufficiently mimicked the conditions that were defined initially.

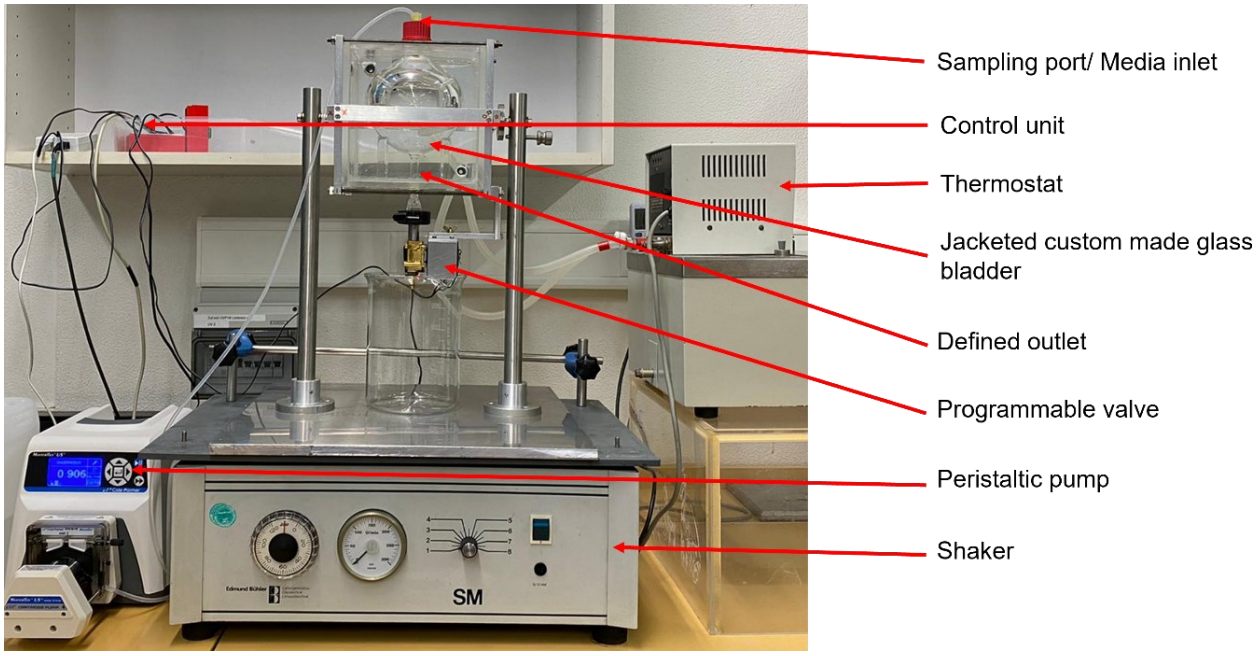

Figure 61. Prototype of bladder model for dissolution testing under physiological conditions.

After first successful dissolution trials, the model was extended to allow threefold determination of drug release simultaneously (see Figure 62).

The model was further expanded by implementing an autosampler that would be able to draw samples and inject them into HPLC vials at pre-determined timepoints. This enabled sampling also during nighttime intervals and contributed towards obtaining more comprehensive dissolution data.

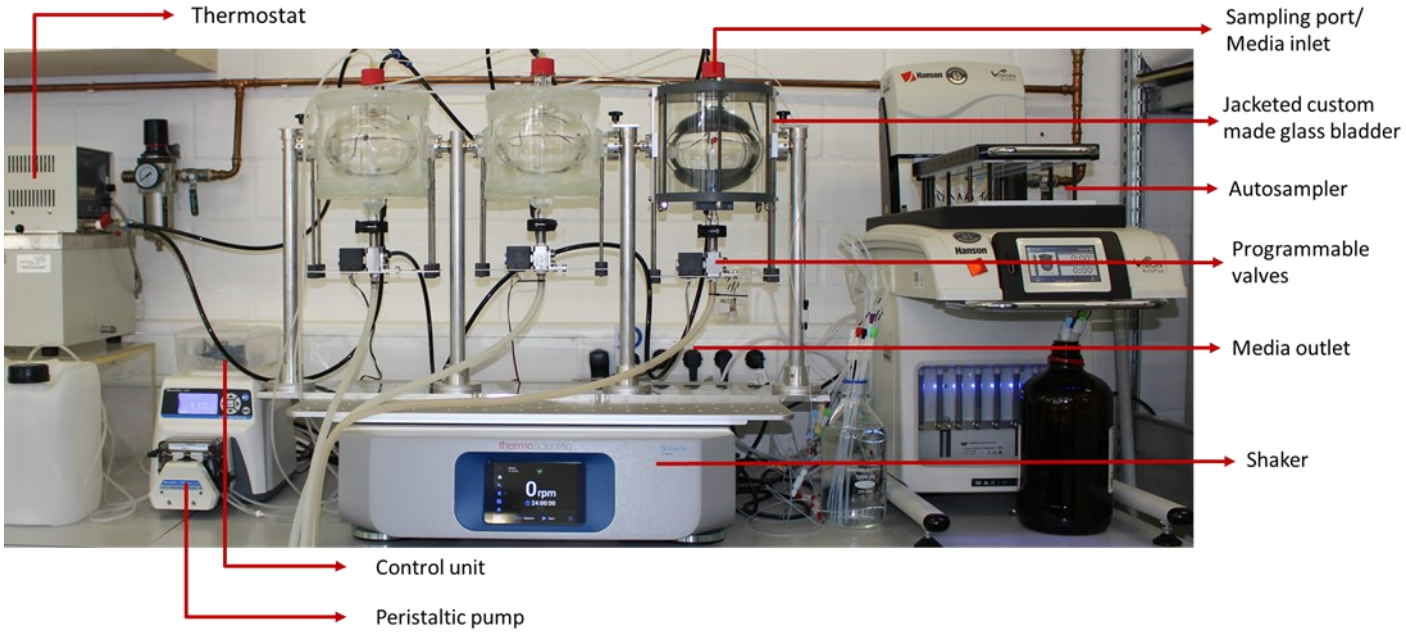

Figure 62. Newly developed extended bladder model with description of components for biorelevant drug release testing (used from (Rahman-Yildir et al., 2022b), by courtesy of Elsevier).

The media outlet was further connected via tubes to a drainage system to avoid overflow of the waste during extended dissolution testing. Since the weight of the additional models was too high for the initial shaker platform, it was replaced by a new shaker that was programmable as well. The extended model was therefore able to be operated fully automated.

3.3.5 Summary

After defining the physiological conditions that the bladder model should be able to mimic based on average values for healthy adults, a prototype bladder model was developed for dissolution testing of intravesical inserts under more biorelevant conditions.

Preliminary investigations with the model were successful and demonstrated its functionality. This led to extension of the bladder model to enable threefold determination of drug release simultaneously. It was feasible to operate the extended model fully automated to ensure continuous sampling throughout experimental runs. Flow rates, temperature, voiding and movement as well as angular positioning of the bladders can be freely modified for investigation of drug release under various experimental conditions. With the help of the newly developed model, it is therefore possible to determine the effect of different (patho-)physiological conditions on the respective drug release and determine the local API concentration that would be achieved at the target site.

3.4 Dissolution testing of intravesical inserts in a biopharmaceutical bladder model

3.4.1 Introduction and objectives

The aim of the following study was to use the new bladder model to determine the release behaviour of the previously developed intravesical inserts under physiological conditions and compare the release data to a compendial setup for release testing.

The release behaviours of the three APIs trospium chloride, lidocaine hydrochloride monohydrate and hydrochlorothiazide incorporated in a PCL matrix were studied for both dissolution models. One of these model intravesical inserts was chosen to study the influence of drug load. Lastly, different operating conditions to simulate varying physiological and pathophysiological conditions were applied to the newly developed bladder model to investigate their influence on drug release.

3.4.2 Mimicking the insertion process

One advantage of the developed model is that the insertion process of the intravesical preparation can be mimicked by passing it through the glass urethra that is connected to the bottom of the glass bladder and functions as media outlet. The inserts were therefore coiled up to fit into a glass tube of 6 mm diameter (corresponding to 18 Charrière) to demonstrate their applicability via conventional urinary catheter. After removing the coiled inserts from the glass tube, they unfolded within 5-10 seconds to resume their original shape (see Figure 63).

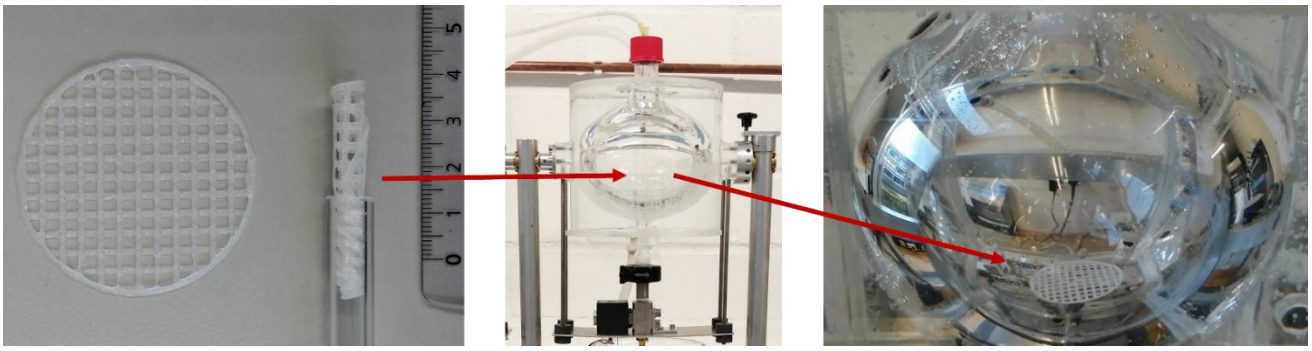

Figure 63. Insert unfolded and coiled up (left) for application and insertion into bladder model (middle) as well as unfolded insert after application inside glass bladder (right).

Administration was demonstrated by manually pushing the insert through the glass tube or glass urethra. For real-life administration, an application device would have to be developed to maneuver the insert through the catheter and into the bladder.

3.4.3 Comparative dissolution studies – bladder model vs compendial setup

3.4.3.1 Effect of API on drug release

To study the effect of the physiological environment on dissolution compared to the USP method, 10 % LC-HCl-, TrCl- or HCT-loaded PCL inserts were prepared and subjected to release studies in the conventional apparatus as well as the novel bladder model.

Figure 64 shows an overview of the obtained cumulative release curves (left) and corresponding concentration profiles (right).

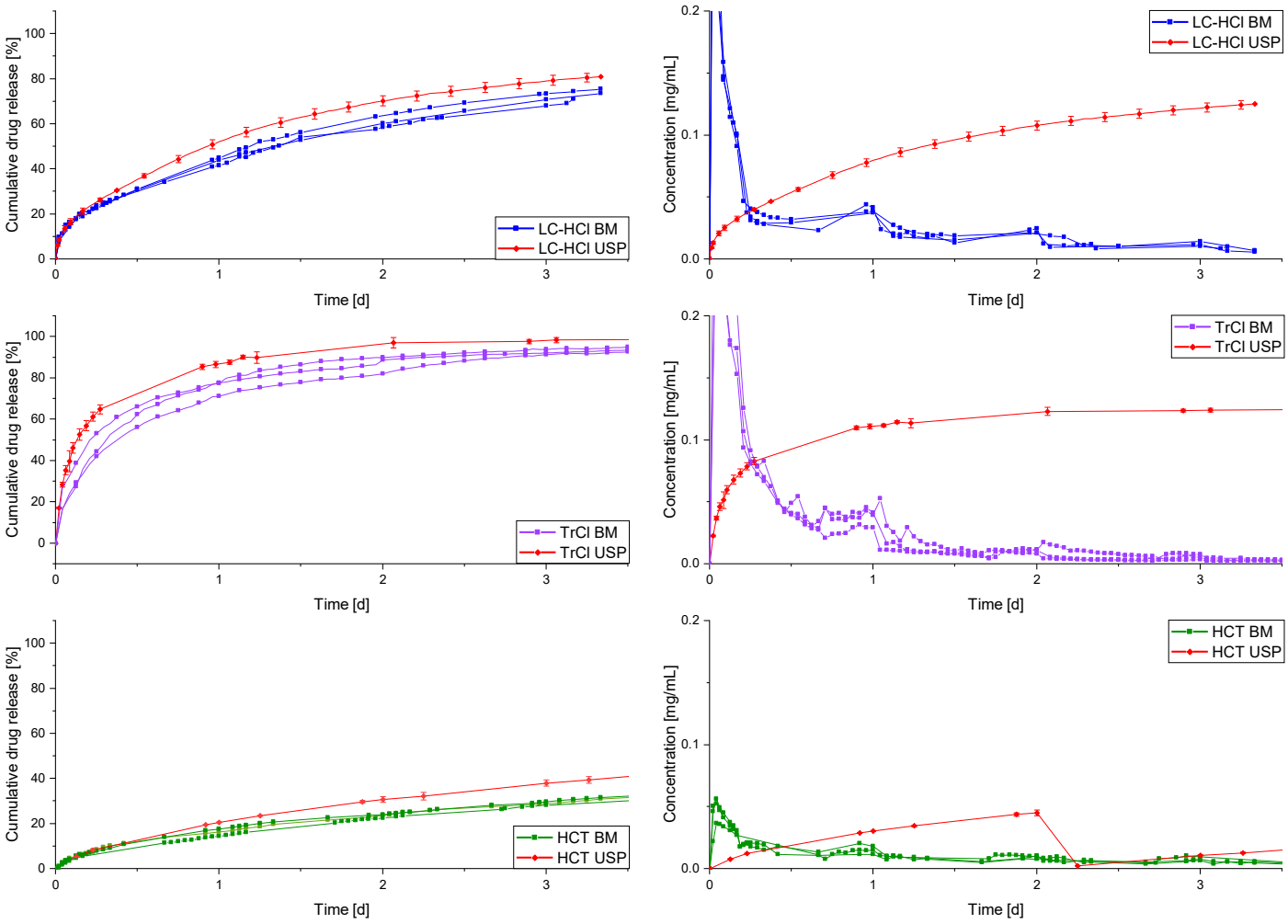

Figure 64. Cumulative release graphs (left) of the LC-HCl- (top row, blue), TrCl- (middle row, purple) and HCT- (bottom row, green) loaded PCL inserts in the custom-built bladder model (BM) and corresponding concentration profiles (right). USP 1 method (USP, red): mean ± s, n=3. Data obtained in bladder model displayed as single curves (according to (Rahman-Yildir et al., 2022b), by courtesy of Elsevier).

It could be seen for all printed inserts that the cumulative drug release of the different APIs was largely in accordance with the release observed while applying the USP method (red curves). However, in all cases the USP dissolution apparatus overestimated the drug release compared to the bladder model. These observed differences were expected since in case of the USP method, the printed inserts were

fully immersed into the dissolution medium and always wetted from all sides, while the inserts in the bladder model were floating on the surface of the medium and were therefore in contact from one side with the dissolution medium. This enables a more efficient exchange of medium in the compendial setup. Additionally, the agitation in the USP apparatus is different as well which may facilitate faster dissolving of the suspended API particles. In the bladder model the agitation is lower, giving likely a more realistic representation of how the release would occur within the human urinary bladder. When applying the dissolution data of the first 60 % of the cumulative drug release to the Higuchi equation, good correlations were found regardless of the dissolution apparatus. This is in accordance with the literature for matrix systems with suspended API particles (Higuchi, 1963a; Siepmann and Siepmann, 2012). A Higuchi release kinetic could further be confirmed by calculating the Korsmeyer-Peppas (KP) exponent n (see Table 24).

Table 24. Calculated R2 according to Higuchi and Korsmeyer-Peppas (KP) model and KP diffusional exponent n for dissolutions studies of drug-loaded inserts in USP apparatus and bladder model (BM); mean ± s, n=3.

	LC-HCl		TrCl	
Dissolution model	USP	BM	USP	BM
Higuchi R^2	0.9981	0.9962	0.9905	0.9935
KP R^2	0.9975	0.9948	0.9800	0.9923
KP exponent n	0.466 ± 0.028	0.433 ± 0.035	0.520 ± 0.007	0.476 ± 0.083

Values close to 0.45 indicate that the release is governed by Fickian diffusion for cylindrical geometries. Despite the complex structure of the inserts, it largely consists of cylindrical elements. Slightly higher values up to 0.89 indicate an intermediate behavior between Fickian diffusion and Case II transport, but may also occur due to geometry effects (Peppas and Sahlin, 1989; Ritger and Peppas, 1987; Siepmann and Peppas, 2011). In the USP apparatus the obtained values for the exponent n are slightly higher than observed in the bladder model and may have occurred due to higher agitation and immersion of the insert, leading to faster medium penetration into the center of the matrix of the insert, which can be characteristic for Case II transport. For the HCT-loaded samples the release kinetic could not be calculated reliably since only around 30 % of the API were released in the investigated time-period. Since polymer degradation under the investigated experimental conditions was only minimal, its contribution to the observed release behavior was considered negligible.

When looking at the concentration profiles that represent the actual drug concentration in the vessel or glass bladder at the respective sampling time, big differences become apparent (Figure 64, right). In the bladder model a periodic fluctuation of concentration could be seen that was not detectable within the setup according to the pharmacopeia. These fluctuations occurred within 24-hour intervals in which the concentration was initially high and then dropped until the nighttime interval began in which no movement or voiding was programmed for the bladder model (see exemplarily for LC-HCl-loaded insert in Figure 65). During this time the sleeping cycle is mimicked, in which a patient would not exhibit much movement and most likely would not get up to urinate.

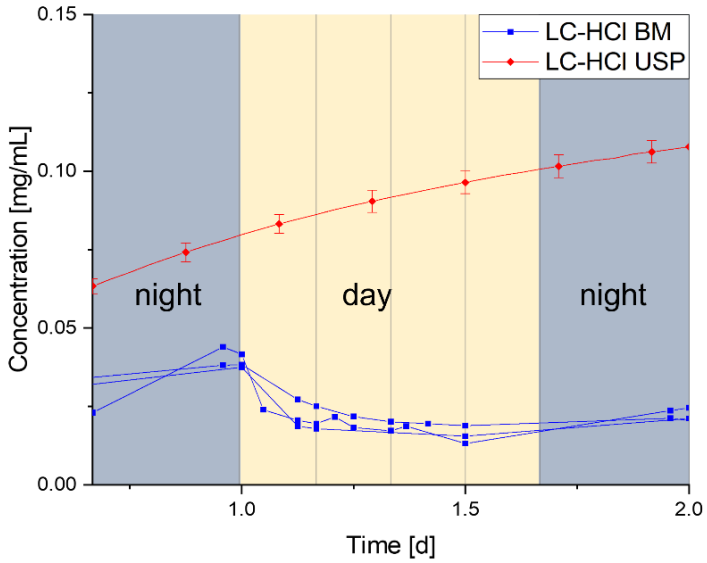

Figure 65. Highlighted section of concentration profiles obtained for LC-HCl-loaded inserts in bladder model (BM) and USP 1 method (USP). Vertical lines indicate voiding mechanism by opening of the magnetic valves. USP 1 method (red): mean ± s, n=3. Data obtained in bladder model displayed as single curves (blue). Grey areas represent nighttime intervals and the yellow area the daytime interval (used from (Rahman-Yildir et al., 2022b), by courtesy of Elsevier).

In this time, the pump that transferred fresh medium into the glass bladder operated at halved speed, as physiologically the urine production is also reduced then. Meanwhile, the API continued to dissolve in the medium that was now accumulating slower and was not being exchanged, so that the drug concentration in the bladder rose again. Once the next daytime interval began, the higher concentrated medium was removed from the model and fresh medium filled up the glass vessels again at the regular flowrate, so that the concentration was lower again. Since new medium was filled up faster than the API particles were dissolved and could diffuse into the surrounding medium, the concentration continued to drop until the next voiding occurred or the nighttime interval began. The concentration continued to decrease across the fluctuations as the reservoir inside the printed insert depleted over time.

From the concentration profiles obtained with the USP method, no fluctuations could be seen for the LC-HCl- or TrCl-loaded inserts (see Figure 64). As expected, the concentration inside the dissolution vessel rose continuously until the drug reservoir in the insert was exhausted (in the studied time-period

only observed for the TrCl-loaded insert). In the initial phase of the experiment, the concentrations measured in the bladder model were higher than those of the USP setup, since here the released API was dissolved and diluted in 900 mL of medium, as opposed to maximally 240 mL in the bladder model. After this initial phase of approximately 6 hours the concentrations measured in the USP apparatus exceeded those measured in the bladder model by up to 15 (LC-HCl) to 40 (TrCl) times towards the end of the study period. In case of HCT, after exchanging the medium in the USP apparatus to avoid aqueous degradation of the drug, a steep drop in the concentration profile was observed. However, this may not contribute toward the understanding of the actual concentration that would occur inside the bladder, since immediately 900 mL of fresh medium were added to the system and the fill level did not change anymore. Here, after around 12 hours of dissolution the concentration measured inside the vessel of the USP apparatus exceeded the concentration measured in the bladder model.

After the first 24 hours of dissolution in the bladder model, the TrCl-loaded inserts already released 75 % of the incorporated API, while in case of HCT only 16 % were dissolved due to its low solubility in the dissolution medium. Nevertheless, the TrCl and HCT inserts showed similar concentration profiles between 1 and 3 days, possibly because in case of TrCl already most of the API was dissolved from the porous network that had formed inside the matrix. The release of the remaining API that is not easily accessible through the pores will be governed by diffusion through the matrix of the polymer and may therefore be slower due to longer diffusion pathways. In case of HCT the release of the API was also generally slower possibly due to its lower solubility. Although these APIs have very different physicochemical properties, they have shown to generate similar concentration profiles in the bladder model. The concentration profiles also revealed for the TrCl-loaded inserts that the target concentration of ≥ 1 µg/mL that was reported in the literature to be effective (Von Walter, 2009) was achieved throughout the course of dissolution testing in the bladder model.

These experiments underline the importance of taking physiological considerations into account when determining whether a certain drug concentration can be reached to achieve efficient therapy. While the cumulative drug release seems to follow the same trend for both dissolution models, the concentration profiles vary significantly. This demonstrates the potential of in-vitro models to gain deeper understanding of drug release at the intended target site compared to the commonly applied compendial setups.

3.4.3.2 Effect of drug load on drug release

The LC-HCl-loaded inserts were chosen for further investigations regarding differences in drug loads since the periodic fluctuations were most pronounced here. It was investigated whether inserts with different drug loads show the same trend in the USP model and newly developed bladder model as

seen in section 3.4.3.1. Therefore, inserts were printed for which the incorporated API amount was doubled, while the amounts of the other excipients were kept constant.

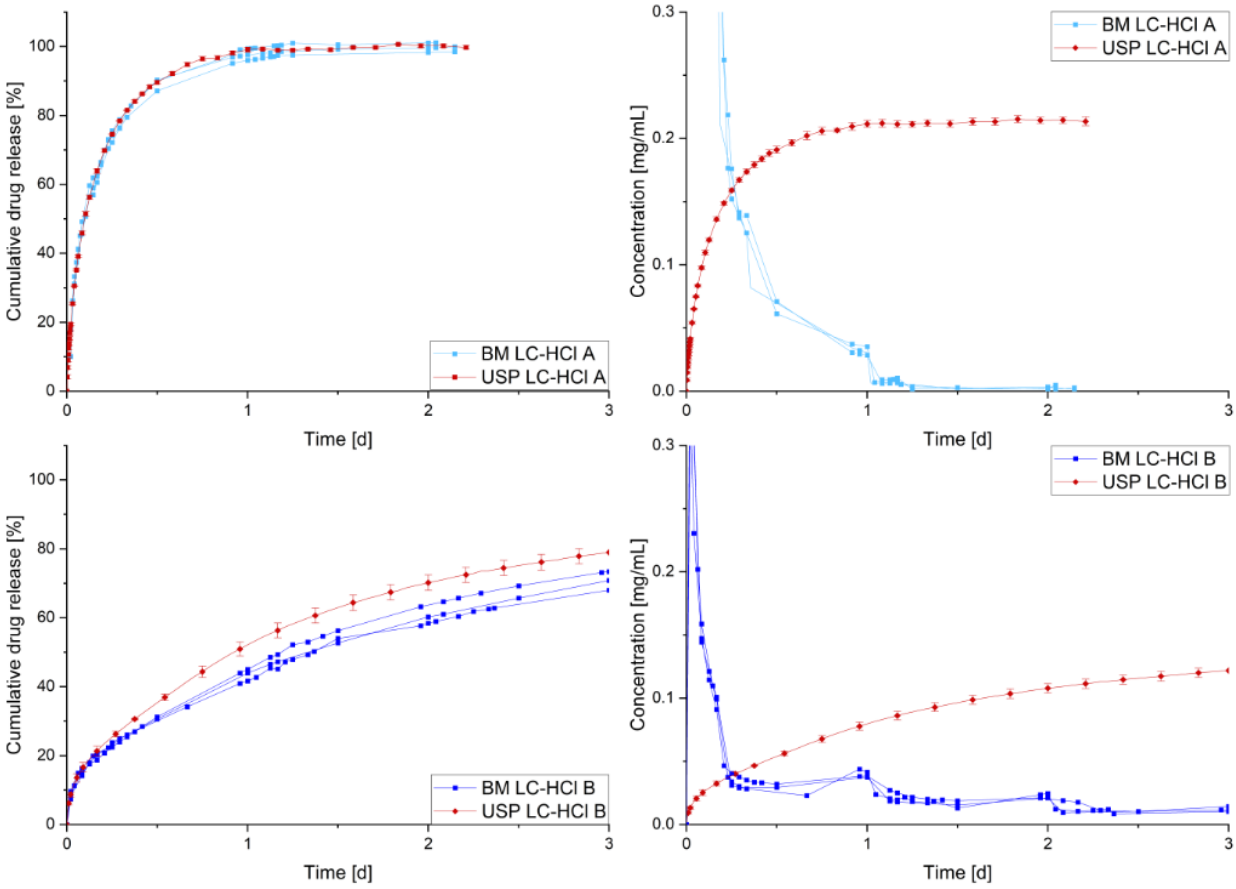

Figure 66. Cumulative drug release (left) and corresponding concentration profiles (right) for 19 % (A, high drug load, top row) and 10 % (B, low drug load, bottom row) LC-HCl-loaded PCL inserts. USP 1 method (USP, red): mean ± s, n=3. Data obtained in bladder model (BM) displayed as single curves (blue) (used from (Rahman-Yildir et al., 2022b), by courtesy of Elsevier).

For the inserts with higher drug load the bladder model showed a nearly identical release profile to the USP apparatus (Figure 66, left). This may be attributed to the high speed of dissolution of the suspended LC-HCl crystals, leaving behind pores that enhance water permeation into the matrix and subsequent dissolution of further API crystals. It seems that at the high drug load a coherent system of LC-HCl particles was formed so that a percolation threshold might have been reached. The so formed large porous network enabled a steady exchange of dissolution medium within the pores regardless of the dissolution conditions such as varying fill levels or degree of movement. Big differences could be observed also in this case when analyzing the corresponding concentration profiles (Figure 66, right). Periodic fluctuations could be seen here as well in 24 h intervals after the end of the nighttime interval in which no movement and a halved pump rate were applied to the bladder model.

The slower release observed for the inserts with the lower drug load could possibly be attributed to the porous network being formed here by less drug particles within the matrix. Therefore, higher

agitation will lead to a more efficient exchange of dissolution medium inside the network and enhance the overall drug release as seen in the USP apparatus. The periodical fluctuations after 24 h in the concentration profiles of the bladder model were more pronounced here. In this case the concentration inside the bladder model was higher compared to the concentration obtained for the inserts with the higher drug load, in which case most of the API was already released and voided again after the first 12 hours. Therefore, less API remained in the insert that could be released after this initial phase, causing the overall concentration to be lower than for the insert with lower drug load after the initial 12 hour phase.

3.4.4 Variation of operating conditions and their effect on drug release

3.4.4.1 Cumulative drug release

The bladder model could be operated fully automated with automatic sampling via autosampler for the TrCl-loaded PCL inserts. To be able to study the investigated timespan more closely and collect more samples throughout the entire experiment, this system was used to investigate changing certain components of the bladder model and their effect on dissolution as well as the sensitivity of the model to changed settings. Investigations were performed using physiological “standard” conditions as well as a number of experimental runs at modified conditions (see Table 25).Urinal flow and voiding frequency were enhanced in order to mimic interindividual differences and conditions such as polyuria due to diabetes insipidus (Robertson, 1995) and frequent voiding due to cystitis or overactive bladder (Marinkovic et al., 2012; Nirmal et al., 2012). The temperature of the water bath was elevated to 41 °C to depict fever symptoms.

Table 25. Standard conditions and modified parameters of dissolution studies in bladder model.

Parameter	Standard conditions	Modified conditions
Pump rate	1.0 mL/min during daytime 0.5 mL/min during nighttime	2.0 mL/min during daytime 1.0 mL/min during nighttime
Dissolution medium	Purified water	Artificial urine (pH 6) (Griffith et al., 1976)
Valve opening frequency	Daytime: voiding every 4 h (= 240 mL) Nighttime: no voiding	Daytime: voiding every 2 h (= 120 mL) Nighttime: voiding every 4 h
Water bath temperature	37 ± 0.5 °C	41 ± 0.5 °C

Figure 67 shows an overview of the cumulative drug release profiles for the respective experiments and will be discussed in more detail the following sections. It can be seen that the release profiles for all experimental runs were similar and showed partially overlapping regions with the curve of the standard conditions. The curve clearly deviating from this trend was the one obtained with artificial urine, in which case a much lower overall release was observed.

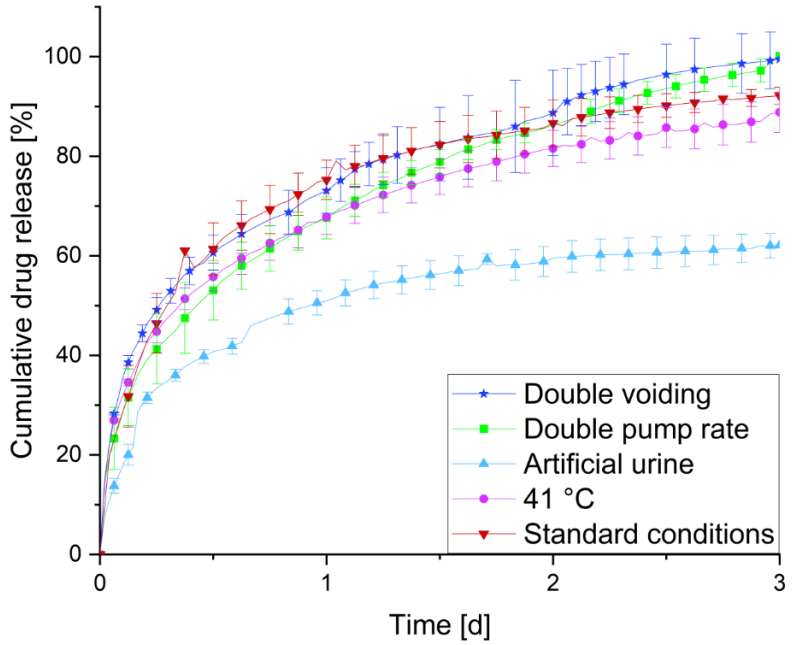

Figure 67. Cumulative drug release profiles for TrCl-loaded PCL inserts in the bladder model under different operating conditions; mean ± s, n=3 (used from (Rahman-Yildir et al., 2022b), by courtesy of Elsevier).

3.4.4.2 Voiding frequency

The concentration profiles showed an initial phase until approximately 14 hours of dissolution in which the concentration was lower than observed for the standard conditions (see Figure 68). After this initial phase, the concentration curves fluctuated around the same values as the standard conditions until they remained slightly higher after around 46 hours.

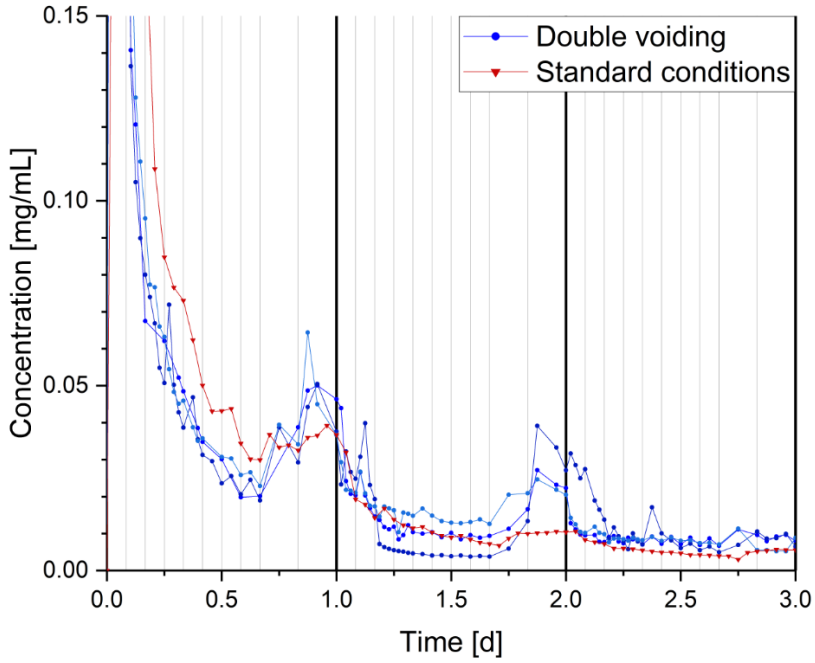

Figure 68. Concentration profiles of experimental run obtained in bladder model with doubled voiding frequency of magnetic valves. Standard conditions in red displayed as mean of triplicate measurement. Vertical lines indicate voiding mechanism by opening of the magnetic valves (used from (Rahman-Yildir et al., 2022b), by courtesy of Elsevier).

When the voiding frequency is doubled, shorter time periods will occur when the insert will be maximally wetted. It might therefore be assumed, that the drug release will be slower due to uneven exposure to the dissolution medium. This trend is visible in the dissolution studies in the first phase of release. Further, the insert will not be exposed to larger amounts of medium, since the maximum filling level in this case would be 120 as opposed to 240 mL of medium. Therefore, the dissolved API will not be diluted as much, if the fresh medium enters the bladder faster than the API can be dissolved and diffuse into the surrounding medium.

3.4.4.3 Urinary flow rate

The pump rate was doubled compared to the standard settings to simulate a condition in which a patient may have increased urine production e.g., when having diabetes insipidus. In this case, given that the voiding frequency remains the same, the insert will be exposed to more medium and, therefore, the dissolved drug will be diluted. In Figure 69 it can be seen that this was the case for the first 1.5 days. After this, the dissolution remains very close to the profile observed during application of standard conditions. Similarly to the case of the doubled voiding frequency (see Section 3.4.4.2) one explanation for this release behavior may be, that in the initial phase of drug release, the API cannot be released from the insert as fast as the new medium is entering the bladder. This results in the concentration being lower than observed for the standard conditions and occurs when the release rate is similar in both cases.

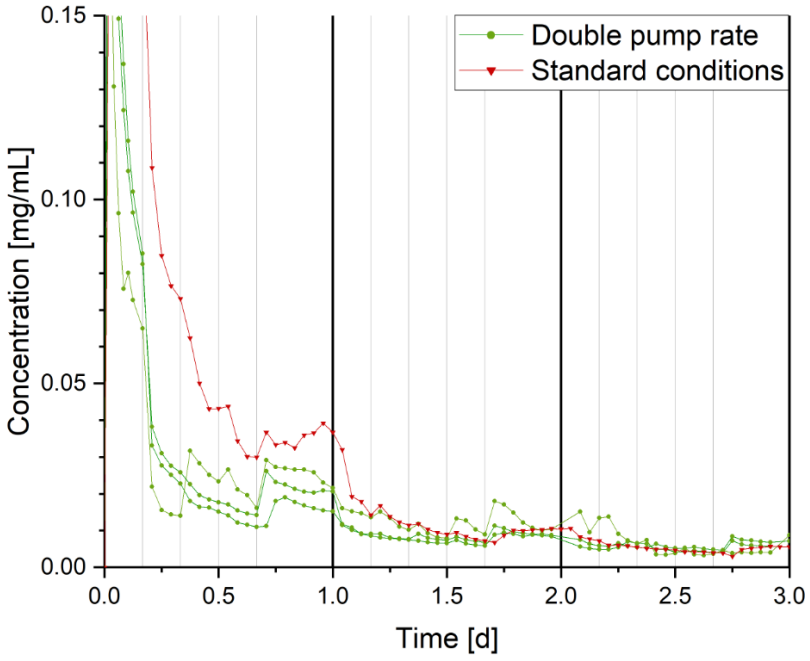

Figure 69. Concentration profiles of experimental run obtained in bladder model with doubled flow rate of peristaltic pump. Standard conditions in red displayed as mean of triplicate measurement. Vertical lines indicate voiding mechanism by opening of the magnetic valves (used from (Rahman-Yildir et al., 2022b), by courtesy of Elsevier).

In case of same release rates, the concentration inside the bladder will be half the concentration of the standard conditions, as seen in the first day of release. Once a certain porosity threshold within the matrix has been established by dissolved API particles, the release becomes more efficient. Here, after 1.5 days the concentration observed was in accordance with the standard conditions, which means that more API could be released since more medium was present to dilute it. This in turn means that the exchange was more efficient in this case and more total amount of API was released from the insert. In the cumulative release curves this could be observed as well when the curve of the standard condition slowly reached a plateau and the curve corresponding to the release of the doubled pump rate was still rising (see Figure 67).

3.4.4.4 Composition of dissolution medium

When changing the dissolution medium from demineralized water to artificial urine, it became apparent that the drug release was much lower. This could be observed for the cumulative drug release (Figure 67) as well as the concentration profiles which were below the curve of the standard conditions almost at all times (see Figure 70).

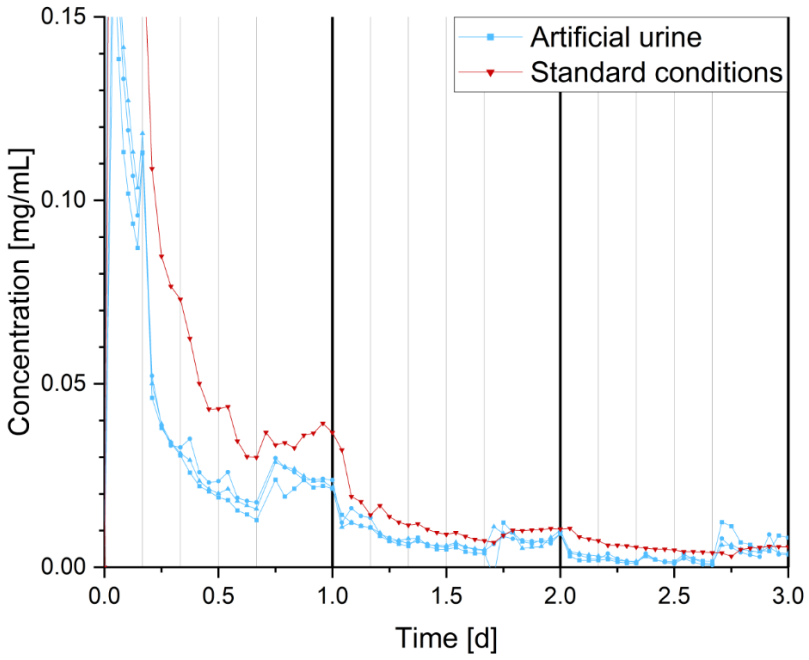

Figure 70. Concentration profiles of experimental run obtained in bladder model with artificial urine. Standard conditions in red displayed as mean of triplicate measurement. Vertical lines indicate voiding mechanism by opening of the magnetic valves (used from (Rahman-Yildir et al., 2022b), by courtesy of Elsevier).

Artificial urine is composed of a variety of different salts to mimic the human urine (Griffith et al., 1976). Haupt et al. found that the solubility of trospium chloride is even higher in artificial urine than in water and could therefore not serve as explanation for the slower observed release (Haupt, 2013).

One possible explanation for the observed release was discussed to be the lower thermodynamic activity of water due to hydration of the various electrolytes present in the artificial urine. This effect could result in less water molecules being available for solvation. The pH difference compared to water was only minimal and therefore considered to have a negligible effect on the dissolution. The curves nevertheless showed the typical periodic fluctuations after voiding and during the nighttime intervals that were observed for the standard conditions as well.

3.4.4.5 Temperature

Temperature differences due to fever conditions that may coincide with certain infectious diseases or illness can have a great impact on release behavior. Figure 71 shows the obtained concentration profiles when the temperature of the custom-made water bath was raised to 41 °C. The concentration curves obtained from the bladder model were initially slightly below the mean curve of the standard conditions. After 1.25 to 1.5 days, however, the concentrations became a bit higher than observed for the standard conditions.

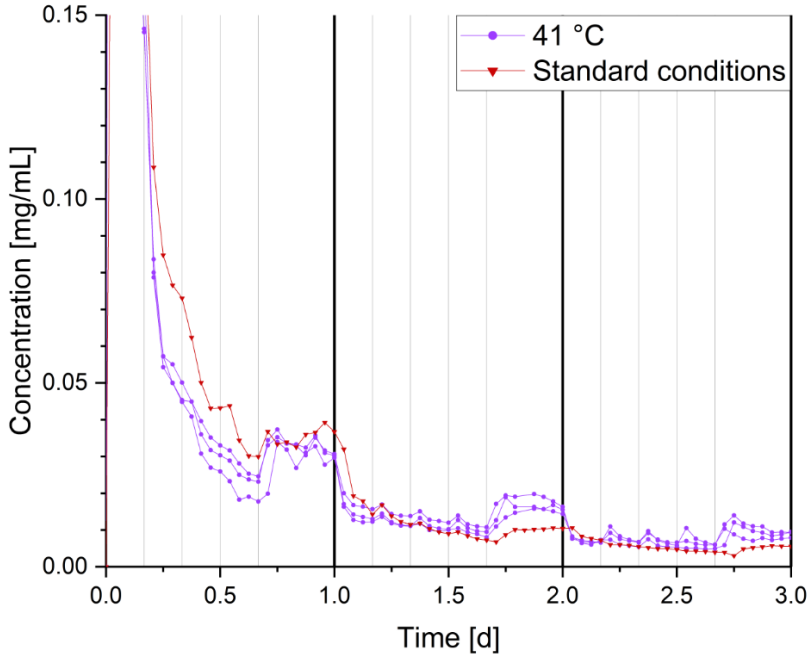

Figure 71. Concentration profiles of experimental run obtained in bladder model at 41 °C water bath temperature. Standard conditions in red displayed as mean of triplicate measurement. Vertical lines indicate voiding mechanism by opening of the magnetic valves (used from (Rahman-Yildir et al., 2022b), by courtesy of Elsevier).

Higher temperatures can increase the solubility of an API while also increasing its diffusion out of the polymeric matrix by decreasing the drug–polymer attraction (Lucero-Acuña et al., 2019). On the other hand, it is possible that increased temperature may cause swelling of the polymer and decrease release rates by decreasing the porous network and entrapping the drug molecules (Setiyorini et al., 2012). The observed concentration profiles may have occurred due to overlapping of the aforementioned

effects when initially some swelling may have slowed down the dissolution, but overall mobility of the API was increased and may have therefore resulted in a higher API release over time. Further, it could be observed that the fluctuation between voidings was more pronounced here and the curves scattered less around the mean value. This may also have been observed due to increased mobility of the API at elevated temperatures and allowed a more homogeneous release.

3.4.5 Summary

Dissolution studies with the novel biopharmaceutical bladder model gave valuable insights into the release profiles of 3D-printed intravesical inserts within a more physiological environment. Although the cumulative drug release profiles in the conventional USP apparatus and bladder model only differed slightly, the corresponding concentration profiles showed great differences due to the constantly changing volume of the dissolution medium and agitation differences in the new model. Periodic fluctuations were observed in the bladder model in all cases in 24 h intervals and between voidings that were differently pronounced depending on the investigated API, drug-load, and operating condition. Thus, the determination of therapeutically relevant API-concentrations from locally applied drug delivery systems for the treatment of bladder conditions might be misleading in the compendial dissolution setup. Determination of concentration profiles are especially important since neither a cumulative nor differential plot are able to serve as reliable indicator for the effectiveness of local drug therapy.

The investigated influence of voiding frequency, pump rate, temperature and dissolution medium on the dissolution profiles demonstrated the possibility of taking physiological conditions into consideration with the new setup. The observed differences in concentration profiles were comparably small but distinguishable from the standard operating conditions. The concentration profiles also revealed for the TrCl-loaded inserts that the target concentration of ≥ 1 µg/mL was achieved throughout the course of dissolution testing.

Although the release from the investigated DDD seems to be quite robust towards changing conditions, the new model showed to be suitable to study varying physiological and pathophysiological conditions by easily adapting its settings.

The new model therefore opens up the possibility to determine the local drug concentration at a given timepoint within the bladder. This can be beneficial during drug development to evaluate whether a target concentration may be reached and can omit the need for mathematical calculations and approximations based on release rates obtained in conventional setups. Due to the flexibility at which dissolution conditions may be varied in the new model, many different experimental runs can be conducted, and their effect on drug release studied.

4 Summary and outlook

Marketed drug products for the treatment of bladder conditions such as overactive bladder are currently still confined to their adverse effects that limit patient's compliance and adherence to therapy. Therefore, recent research has focused on manufacturing new drug delivery systems to overcome these problems and allow effective and safe therapy while using the intravesical route. The aim of the present work was to develop flexible drug-loaded intravesical inserts that have the potential to overcome the existing limitations and allow local application of various APIs.

3D-printing by pressure-assisted micro syringe system was thereby selected as suitable manufacturing method due to its many favourable attributes such as easy incorporation of various (pharmaceutical) polymers into semi-solid feedstock material for the 3D-printer, processability at low temperatures and the possibility to generate flexible DDD that could be applied via urinary catheter.

After thorough investigations regarding process understanding, semi-solid printable inks containing EVA as non-degradable polymer and PCL as degradable polymer were developed and characterized regarding their critical quality attributes such as rheological properties and recovery after printing. Suitable post-printing drying conditions were defined based on obtained porosity, geometry and dissolution of the inserts. The question of printability was addressed by assessing different quality defining attributes of the formulation and the printed structures. The printability score as a new parameter for objective evaluation of the quality of a printed object was developed and its suitability investigated in a design of experiments. It thereby showed good results for ranking different combinations of printing settings in regard to the resulting print quality.

After development of trial formulations, it was feasible to successfully incorporate the freely soluble APIs lidocaine hydrochloride monohydrate and trospium chloride and the poorly soluble hydrochlorothiazide into sustained release inserts that released the respective API over the course of at least two weeks. The success of sustaining the release was thereby dependent on the API's solubility in the dissolution medium, as well as the formation of larger API clusters within the matrix of the printed inserts. The release rate of the inserts could be flexibly tailored by adapting the geometry and the corresponding surface area to volume ratio or drug load.

The effect of porosity on release behaviour and its influencing factors were extensively investigated via µCT imaging and image analysis that allowed quantification of the porosity and gave valuable insights into pore sizes and surface areas before and after dissolution. It revealed that generally within the same pressure condition applied during drying, the porosity increased with increasing temperature while the mean dissolution time decreased. It further showed that higher drug loads above 10 % also led to higher porosity and eventually reached the percolation threshold. This led to formation of

continuous porous networks caused by initially contained pores and dissolved API particles leaving behind new pores upon dissolution and enhanced the overall drug release.

Since the degradation of the PCL inserts was found to be minimal under the investigated experimental conditions and could potentially pose a challenge for its applicability in case of frequently repeated administrations, refinement of the degradable DDD revealed a PCL-PEG copolymer as suitable candidate. This matrix polymer was further suitable to prolong the release of TrCl to achieve clinically relevant release rates. Overall, clinically relevant dissolution could be achieved for LC-HCl and TrCl over the course of at least two weeks for non-degradable and degradable inserts. The TrCl-loaded inserts were further investigated regarding their stability during storage and remained stable in terms of mechanical properties and dissolution profile over the course of four weeks when stored at room temperature and ambient conditions. One possible refinement for the application of these intravesical devices would be the development of an applicator system for administration via urinary catheter.

While compendial setups are commonly used during drug development for evaluation of the release behavior, they can rarely take physiological conditions into account and are not always a sensible choice for determining whether therapeutically relevant concentrations may be achieved at the target site.

Therefore, in the scope of this work, a biorelevant dissolution model has been developed and manufactured in order to investigate drug release of the newly developed inserts within a more physiological environment. The new bladder model could be operated fully automated and allowed determination of the local API concentration within the bladder at a given time-point. Media flow rates, temperature, voiding and movement as well as angular positioning of the bladders could be freely modified for investigation of drug release under various experimental conditions. It was therefore possible to determine the effect of different (patho-)physiological conditions on the respective drug release. Compared to the compendial setup, the cumulative release profiles only differed slightly, while the corresponding concentration profiles displayed great differences and revealed periodic fluctuations in 24 h intervals that were not detectable within the USP apparatus. While the developed inserts seemed to be relatively robust toward changes in operating conditions, the model was able to generate distinguishable results compared to the standard operating conditions. Its key advantage lies in the possibility of investigating various conditions and scenarios and their effect on drug release without the need for estimated release rates based on mathematical calculations. Nevertheless, further investigations regarding different (non-porous) matrix systems and operating conditions would be required in the future together with in-vivo experiments to further evaluate the relevance of the new model and validate the findings.

In conclusion, the present work demonstrated the ability of using PAM 3D-printing as manufacturing tool for sustained release, flexible drug-loaded inserts and allowed incorporation of various polymers and APIs. Process understanding was thereby essential to obtain reliable and reproducible results. The release of the inserts could be determined in a newly developed biopharmaceutically relevant bladder model that may serve as platform for investigating various (patho-)physiological conditions and may reduce the need for mathematical estimations of drug release at the target site.

5 Materials and methods

5.1 Materials

Table 26. Model drug substances used for the development of the intravesical inserts.

Substance	Batch number	Source
Hydrochlorothiazide (HCT)	RHCTP50236	Unichem, India
Lidocaine hydrochloride monohydrate (LC-HCl)	2005051808	Merckle; Germany
Trospium chloride (TrCl)	76995	Dr. Pfleger Arzneimittel GmbH, Germany

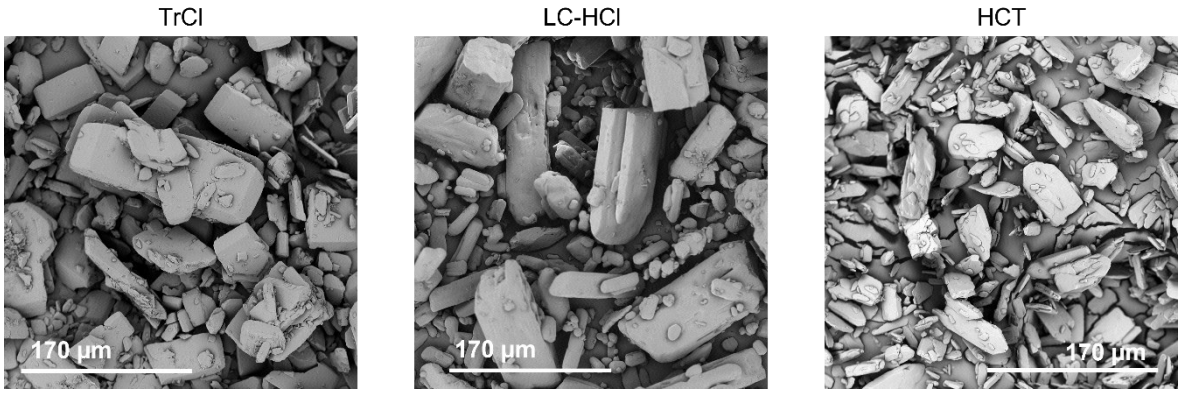

Figure 72. SEM-images of APIs TrCl (left), LC-HCl (center) and HCT (right).

Table 27. Particle sizes of APIs TrCl, LC-HCl and HCT expressed as x10, x50 and x90 quantiles; mean of triplicate measurements.

Dx [µm]	TrCl	LC-HCl	HCT
Dx10	6	11	8
Dx50	34	44	28
Dx90	106	215	62

Table 28. Matrix-polymers used for intravesical inserts.

Substance	Name/ grade	Source
Ethylene vinyl acetate copolymer	Elvax 40W	DuPont, Belgium
PEG-terminated PCL Copoylmer	Viatel™ C12 PEG	Ashland, United States
Polycaprolactone	Capa 6506	Perstorp, UK and Ingevity, UK
Poly(D,L-lactide-co-glycolide)	Viatel™ DLG 5003 A (50:50A)	Ashland, United States
Poly(D,L-lactide)	PDLLA E	Ashland, United States
Poly(L-lactide-co-ε-caprolactone)	Viatel™ LC 7010 E	Ashland, United States

Table 29. Plasticizers used for screening during development of inserts.

Substance	Name/ grade	Source
Acetyl tributyl citrate 98 %	-	Sigma-Aldrich, Germany
Cetylalcohol	Ph. Eur.	Caesar & Loretz, Germany
Dibutyl sebacate 97 %	-	Sigma-Aldrich, Germany
Glycerol 85 %	Ph. Eur.	Caesar & Loretz, Germany
Medium-chain triglycerides	Miglyol 812	Caesar & Loretz, Germany
Oleic acid	Ph. Eur.	Caesar & Loretz, Germany
Polyethylene glycol	PEG 400	Clariant, Germany
Sorbitol 70 %	Ph. Eur.	Caesar & Loretz, Germany
Stearic acid	Baerocid SMS-1 V	Baerlocher, Germany
Triacetin 99%	-	Sigma-Aldrich, Germany
Triethyl citrate	Citrofol®Al	Jungbunzlauer, Switzerland

Table 30. Additives used during formulation development of inserts.

Substance	Name/ grade	Source
Ammonium methacrylate copolymer	Eudragit® RS PO	Evonik, Germany
Hydroxypropyl methylcellulose	Tylopur SR 2208	Shin-Etsu Chemical, Japan

Table 31. Solvents used for preparation of semi-solid inks or analytics.

Solvent	Grade	Source
Acetonitrile	HPLC grade	VWR, France
Ethyl acetate	p.a.	VWR, France
Demineralized water	-	In-house production
Purified water	p.a.	In-house production
Tetrahydrofuran	p.a.	Fischer Scientific, UK

Table 32. Components of artificial urine according to (Griffith et al., 1976) for dissolution testing.

Substance	Amount (g/L)	Source
Ammonium chloride	1.0	Merck, Germany
Calcium chloride dihydrate	0.65	Carl Roth, Germany
Creatinine	1.1	Carl Roth, Germany
Di-sodium oxalate	0.02	Carl Roth, Germany
Magnesium chloride hexahydrate	0.65	Carl Roth, Germany
Sodium chloride	4.6	Carl Roth, Germany
Sodium sulfate	2.3	Carl Roth, Germany
Tri-sodium citrate dihydrate	0.65	Carl Roth, Germany
Potassium chloride	1.6	Merck, Germany
Potassium dihydrogen phosphate	2.8	Merck, Germany
Urea	25	Carl Roth, Germany

5.2 Methods

5.2.1 Preparation of semi-solid printing formulation

5.2.1.1 Drug-free semi-solid formulations

After selecting the most suitable plasticizer, placebo formulations were prepared with varying ratios of polymers, solvent and plasticizer. In order to minimize material waste and manufacturing time, small batches (10-15 g) of formulation were prepared by stirring the solutions overnight and manually extruding them through a 5 ml syringe into a net shaped geometry. Solutions with high polymer content required an additional heating step of 20 min at 100 °C. The resulting inserts were subsequently dried at ambient temperature and visually evaluated. The most promising placebo-formulations were then used for further printing studies with the 3D-Bioplotter.

5.2.1.2 Drug-loaded semi-solid formulations

Formulations for 3D-printing were prepared by mixing the components without the API on a heated mixing plate in a sealed container for 1 h at 100 °C until the polymer was completely dissolved. The mixture was cooled to approx. 50 °C, and the API suspended with an overhead stirrer at 700 rpm for 3 min. The semi-solid printing formulation was then transferred into a disposable 30 mL syringe with plunger and equilibrated for 10 min in the heated printhead of the 3D-printer prior to printing.

Table 33. Composition and printing conditions of semi-solid printing ink of trial formulation.

Formulation [%, w/w]	PCL	EVA	THF	DBS	LC-HCl	Printing speed [mm/s]	Printing pressure [bar]	Printing temp. [°C]
PCL start	31	-	46	15	8	20	1.2	35
EVA start	-	38	46	8	8	20	0.5	35

Table 34. Composition and printing conditions of semi-solid printing ink of 10 % drug-loaded inserts.

Formulation [%, w/w]	PCL	EVA	THF	DBS	API	Printing speed [mm/s]	Printing pressure [bar]	Printing temp. [°C]
PCL LC-HCl	37.5	-	37.5	19	6	20	1.3	35
PCL TrCL	37.5	-	37.5	19	6	20	1.3	35
PCL HCT	37.5	-	37.5	19	6	20	1.2	35
EVA LC-HCl	-	40	47	8	5	20	1.0	35
EVA TrCL	-	40	47	8	5	20	0.8	35
EVA HCT	-	44	41	9	6	18	2.3	35

Table 35. Composition and printing conditions of semi-solid printing ink containing additives as pore-blocking agents.

Formulation [%, w/w]	PCL/ EVA	Additive	THF	DBS	LC-HCl	Printing speed [mm/s]	Printing pressure [bar]	Printing temp. [°C]
PCL Eudragit	35	3 (Eudragit)	35	24	9	22	1.8	35
EVA Eudragit 3 %	42	3 (Eudragit)	39	8	8	20	2.4	35
EVA Eudragit 5 %	40	5 (Eudragit)	39	8	8	20	2.5	50
EVA HPMC	40	5 (HPMC)	39	8	8	28	2.5	60

Table 36. Composition and printing conditions of semi-solid printing ink of inserts with varying API or solvent content (mS: more solvent).

Formulation [%, w/w]	PCL	EVA	THF	DBS	LC-HCl	Printing speed [mm/s]	Printing pressure [bar]	Printing temp. [°C]
PCL 5 %	39	-	39	19	3	19	1.1	35
PCL 10 %	37.5	-	37.5	19	6	20	1.3	35
PCL 15 %	36	-	36	19	9	19	1.5	35
PCL 25 %	33	-	33	17	17	18	1.7	35
PCL 10 % mS	33	-	46	16	5	18	0.6	33
EVA 5 %	-	40	49	8	3	20	0.8	35
EVA 10 %	-	40	47	8	5	20	1.0	35
EVA 15 %	-	38	46	8	8	20	1.2	35

Table 37. Composition and printing conditions of semi-solid printing ink of biodegradable inserts.

Formulation [%, w/w]	PLGA	PLCL	PCL-PEG	EA	TrCl	Printing speed [mm/s]	Printing pressure [bar]	Printing temp. [°C]
PCL-PEG	-	-	53	41	6	15	2.0	38
PLGA/PLCL	46	5	-	43	6	14	3.2	42

5.2.2 Layer-stacking test

Initial screening of formulations was performed by filling the semi-solid formulations into 5 mL polypropylene syringes and manually extruding them into net-patterns along a template of the final insert design. Different needle tips in accordance with the needle tips used with the Bioplotter for 3D-printing were connected to the syringe to extrude the formulations. After extrusion and drying, the shape fidelity and degree of merging was assessed visually.

5.2.3 Pressure-assisted micro-syringe printing

The software package Inventor (Autodesk, USA) was used to create computer-aided design (CAD)-files of net-shaped circular model inserts with three layers, a layer thickness of 0.67 mm and diameter of 5 cm. Slicing of the model was performed with the slicing software Prefactory 3.0 (EnvisionTec, Germany). To study the effect of geometry, one, two and three layers were printed as well as three layers without infill and a three-layered ring with a double contour.

The printing process was carried out at 35 °C with a platform-temperature of 25 °C using the PAM-operated 3D-Bioplotter (EnvisionTec, Germany) unless stated otherwise. A rectilinear infill was printed with 4 mm distance between the strands and 0.2 mm distance from the contour. Pre- and post-flow were adapted to the printed formulation.

5.2.4 Post-processing/ drying

The printed inserts were dried at ambient conditions until constant mass was reached unless stated otherwise.

For the extended evaluation of the effects of drying temperature and conditions, model inserts were also dried at 25, 32.5 or 40 °C in drying ovens under atmospheric pressure and in vacuum driers at 500 mbar (refers to section 3.2.8.3).

5.2.5 Film casting

Films were produced to evaluate textural properties or contact angles of various formulations. The films were manufactured by solvent-casting method. Therefore, semi-solid formulations according to the compositions in Table 2 and Table 38 were prepared as described in section 5.2.1 and cast into films using the coating bench Coatmaster 510 with the coating knife Mulitcator 411 (Erichsen, Germany).

Films were produced with a wet-film thickness of 500 µm and dried at ambient temperature for 3 days prior to the measurements.

Table 38. Composition of film-formulations for analysis of contact angle.

Formulation [%, w/w]	Polymer	THF	EA	DBS
PCL	40	40	-	20
EVA	42	49	-	9
PLGA	40	-	60	-
PDLLA	50	-	50	-
PLCL	40	-	60	-

5.2.6 Design of Experiments (DoE)

The effects of process parameters during printing on the quality attributes of printed inserts was analyzed by applying a Central Composite Design (CCD) statistical design of experiments. The two factors printing speed and printing pressure were varied according to Table 39 and Table 40 for 10 % drug-loaded PCL and EVA formulations (composition can be seen in section 5.2.1). The experimental runs were performed in randomized order and contained four factorial points, four star points and one center point, which was replicated three times. The distance of the star points to the center point was chosen to be 1.414. Data evaluation was performed with Modde 13 (Umetrics, Sweden) on a 5 % significance level. Insignificant parameters were removed to obtain models with the highest goodness of prediction (Q^2). The investigated responses were strand thickness, relative standard deviation (RSD) of the strand thickness, printability index and printability score. Values obtained for strand thickness and printability index were given as mean of 20 measurements.

Table 39. Coded and uncoded factor-level combinations applied for the CCD of PCL-inserts. α -values indicating star points.

Pressure coded	Pressure uncoded [bar]	Speed coded	Speed uncoded [mm/s]
-1	0.8	-1	15
1	1.8	-1	15
-1	0.8	1	25
1	1.8	1	25
-α	0.6	0	20
+α	2	0	20
0	1.3	-α	13
0	1.3	+α	27
0	1.3	0	20
0	1.3	0	20
0	1.3	0	20

Table 40. Coded and uncoded factor-level combinations applied for the CCD of EVA-inserts. α -values indicating star points.

Pressure coded	Pressure uncoded [bar]	Speed coded	Speed uncoded [mm/s]
-1	0.5	-1	15
1	1.5	-1	15
-1	0.5	1	25
1	1.5	1	25
-α	0.3	0	20
+α	1.7	0	20
0	1.0	-α	13
0	1.0	+α	27
0	1.0	0	20
0	1.0	0	20
0	1.0	0	20

5.2.7 Data analysis and graphing

Arithmetic calculations during data evaluation were performed with Microsoft® Excel® 2019 (Microsoft Corporation, USA). Origin®Pro 9.0.0G (OriginLab Corporation, USA) was further used for graphic representation of the data. Statistical evaluation of the data was performed with Microsoft® Excel® 2019 (Microsoft Corporation, USA).

To determine statistical outliers, the Grubbs test was performed (CI of 95%) after performing the normality test via the Origin®Pro software. The Origin software was further used for performing the Hershel-Bulkley fit on rheological data.

Chemical structures of the APIs were drawn using the software ChemDraw Professional (version 21.0.0, PerkinElmer, USA).

5.2.8 Analytical methods

5.2.8.1 Differential scanning calorimetry (DSC)

Approximately 5 mg of each sample were heated in a pierced aluminum pan from -30 to +180 or +300 °C at a rate of 10 °C/min (DSC1, Mettler Toledo, Switzerland). A second heating cycle was performed after cooling the samples to -30 °C.

5.2.8.2 X-Ray powder diffraction (XRPD)

XRPD measurements were performed to characterize the crystalline or amorphous nature of the polymers. XRPD measurements were performed in transmission mode of the PANalytical X'Pert PRO (Malvern Panalytical, Germany) at 30 kV and 30 mA and scanned from 10-50° (2 theta) with a step width of 0.033°.

5.2.8.3 Confocal Raman microscopy

The confocal Raman microscope alpha 300 R (WITec, Germany) equipped with a single mode laser with an excitation-wavelength of 532 nm was used. The laser power on the samples was set to 20 mW applying a Zeiss EC Epiplan-Neofluar HD 20x/0.5 microscope objective. The Raman microscope was configured with a WITec UHTS 300 spectrometer and an Andor iDus Deep Depletion CCD camera, which was cooled down to -60 °C. By using a reflection grating with 600 lines/mm an average spectral resolution of 3.8 cm^{-1}/pixel was achieved. Raman images with an area of 1000 x 800 µm (LC-HCl), 1000 x 1000 µm (TrCl) and 900 x 1100 µm (HCT) were obtained from the cross-section of the printed strands using a spatial resolution of 10 µm. The exposure time was set to 0.05 s per spectrum. Light microscopic bright field images of the cross-section of the printed strands were obtained using a Zeiss EC Epiplan HD 10x/0.25 microscope objective. The processing of Raman spectra as well as the compilation of the Raman images were conducted using the software WITec FIVE 5.3.13.105 (WITec, Germany). The cosmic rays were first removed, followed by baseline correction and normalization of Raman intensities.

5.2.8.4 Optical light microscopy

Aspect ratio and strand thickness of the printed inserts were determined via optical light microscope equipped with a digital microscope camera (Leica Microsystems, Germany) after drying. Images were acquired via the software Leica Application Suite (version 4.6, Leica Microsystems, Germany). To determine the aspect ratio, strands were cut with a scalpel in random sections of the insert and the cross-sections were measured using the vertical and horizontal Feret-diameter.

5.2.8.5 Scanning electron microscopy (SEM)

The surface morphology and inner structure of the printed inserts or APIs was investigated via scanning electron microscopy (Phenom G2 pro, Thermo Fisher Scientific, USA) after applying 15 nm gold sputter coating.

5.2.8.6 X-ray micro-computed tomography (µCT) measurements

To determine the inner porosity of the inserts, µCT-images were taken with the CT Alpha (ProCon X-Ray, Germany). A 3D-printed customized sample holder was developed to hold the inserts in place in a 10 ° or 45° angle to avoid ring-artifacts in the images (Figure 73).

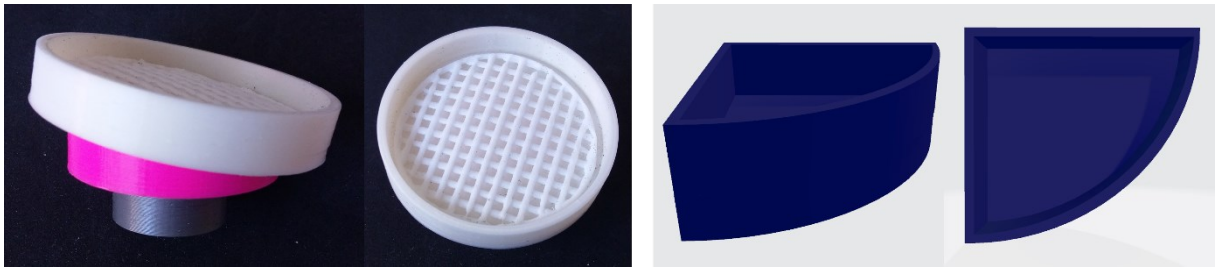

Figure 73. Sample holder for µCT measurements of intravesical inserts for unfolded (images, left) and folded (CAD models, right) inserts.

The sample holder at 10 ° was used for overview images of the inserts for which the sampled were fixed unfolded (Figure 73, left). The sample holder with an angle of 45 ° was used for all other inserts (Figure 73, right). In this case the inserts were folded over twice and secured within the sample holder. This allowed the resolution of the resulting images to be improved from 28 to 20 voxels.

A 0.5 mm aluminum filter was applied to improve image quality when necessary. The voltage was set to 80 kV and the current to 110 µA. The exposure time was 500 ms and one image was taken as average of 5. The number of projections was set to 1600. 16-bit measurements were carried out.

Image reconstruction of the raw images was performed with the software VG studio 3.0.1 (Volume Graphics GmbH, Germany)

5.2.8.7 Image analysis

For image analysis of µCT- and light microscopic images, the software package imageJ 1.53c (Wayne Rasband, USA (Schindelin et al., 2012)) with Java 1.8.0_66 was used.

For the reconstructed µCT images, the sample holder was manually removed from the images in imageJ to obtain images in which only the inserts were visible. Respective markings were saved to ensure reproducibility. The images were transformed to 8-bit images and the function “3D Objects Counter” applied during image analysis to obtain surface and volume information of the matrix and pores of the insert. Filtering of the detected objects was performed by excluding all objects smaller than 1 million voxels for the matrix. To quantify the air, the images were inverted before applying the 3D Objects Counter function in imageJ and pores only included from 4 to 1 million voxels.

5.2.8.8 Size determination - (strand-) thickness and aspect ratio

Aspect ratio and strand thickness of the printed inserts were determined via optical microscope (Leica Microsystems, Germany) after drying. To determine the aspect ratio, strands were cut with a scalpel in random sections of the insert and the cross-sections were measured using the vertical and horizontal Feret-diameter. 10 sections were analyzed per sample unless stated otherwise. Images were taken with the Leica software.

For determination of the printability score, 20 measurements were performed for strand thickness. The perimeter and surface are of the enclosed pores formed by a printed rectangular grid were also determined as mean value of 20 measurements. Three printed samples were used for the measurements of one printing condition.
In case of test specimen for the tensile tests during short-term stability studies, the thickness of the samples was determined via digital caliper.

5.2.8.9 Drop shape analysis

The Drop Shape Analyzer DSA 100 (Krüss, Germany) with a Hamilton syringe and syringe needle tip of 800 µm diameter was used to determine the contact angle between polymer-films and demineralized water. The films were manufactured as described in section 5.2.5.
To determine the contact angle, a drop volume of 15 µl was deposited onto the films and images were acquired for 70 s by the integrated CCD camera. Images after 1 and 60 s were used for analysis, which was performed by using the circular segment method provided by the DSA1 software (version 1.90.014, Krüss, Germany).

5.2.8.10 Characterization of drying process

In order to study the effect of drying conditions on porosity and dissolution behavior, LC-HCl loaded PCL-inserts were printed and dried at various drying conditions to create differently porous systems. The printed inserts were stored at 25, 35 and 45 °C in drying ovens (1013 mbar) as well as in vacuum dryers (500 mbar) directly after printing. Three inserts for each drying condition were analyzed via SEM and µCT and subsequently subjected to dissolution studies. Additionally, these inserts were weighed at predefined timepoints to investigate the drying kinetic and determine when constant mass was reached.

Mass reduction during drying was calculated according to Equation 6.

$$M_t = \frac{m_t - m_f}{m_f} \qquad \text{Equation 6}$$

M_t: solvent loss at timepoint t [g] ; m_t: mass of insert at timepoint t [g]; m_f: mass after drying [g]

5.2.8.11 Assessment of residual solvent

Residual solvent content was assessed gravimetrically by drying drug loaded samples additionally after the regular drying process for five days under reduced pressure (500 mbar) at 45 °C in vacuum dryers. Six samples per batch were weighed on an analytical balance before and after drying and the mass loss detected. The mass loss was evaluated in a worst-case scenario to be caused only by the used solvent.

5.2.8.12 Matrix erosion

For the degradation studies, polymer rods of degradable polymers PLGA, PDLLA and PLCL dissolved in ethyl acetate were cast into a mold to obtain defined shapes and same surface area to volume ratio (see composition in Table 41).

Table 41. Composition of semi-solid formulations used for degradation studies.

Formulation [%, w/w]	Polymer	EA
PLGA	40	60
PDLLA	50	50
PLCL	40	60

After drying, the rods were cut into smaller pieces with a length of 1 cm and diameter of 0.5 cm. For each polymer, three rods for each time point were placed into a flask with 150.0 mL demineralized water and placed on a shaker operating at 50 rpm. Samples were taken after 1, 2, 3 and 4 weeks and dried at 45°C for 7 days. After cooling the samples in a desiccator, they were weighed on an analytical balance. Temperature and pH were monitored for the duration of the degradation studies.

5.2.8.13 Analysis of mechanical properties

5.2.8.13.1 Puncture test of plasticized films

The Texture Analyser TA.XT plus (Stable Micro Systems, UK) with the puncture test was used to determine the flexibility of cast films and thus allow a characterization of the efficiency of the plasticizers. Additionally, a visual evaluation of the film properties regarding their morphology was performed. Characteristics such as a visible white turbidity or rough surface were of particular interest. Films were prepared as described in section 5.2.5.

For the execution of the puncture test, a 2 x 2 cm film was placed in a sample holder with a central orifice of 9.9 mm diameter. The used cylindrical probe to puncture the film had a diameter of 5 mm and was operated at a speed of 1 mm/s. Force and distance of the probe were recorded upon contact with the film. The test was stopped when the film ruptured, or the probe was maximally displaced. Measurements were performed in triplicate.

From the obtained force-distance diagrams, the linear region in the ascending part of the curve before plastic deformation was used to calculate the slope.

5.2.8.13.2 Tensile strength – stability studies

For the determination of mechanical properties, a tensile test was performed using the Texture Analyser (TA.XTplus, Stable Micro Systems, UK) according to standard DIN EN ISO 527-1 and -3.

For this purpose, semi-solid 10 % TrCl-loaded EVA and PCL-PEG formulations were printed into dumbbell shaped test specimen with the 3D-bioplotter. Samples were measured after drying or after storage for 4 weeks at ambient conditions and at 40 °C and 75 % relative humidity.

The test speed was set to 0.1 mm/s and the test lasted until the sample ruptured or the probes reached maximum displacement. The recorded force-distance diagrams were transformed into stress-strain diagrams considering the cross-section of the test specimen. From the linear region of the stress-strain curves between 0.05 and 0.5 % strain the slope was calculated for determination of the Young's modulus. Measurements were carried out in triplicate.

5.2.8.14 Drug content determination

5.2.8.14.1 UV measurements and HPLC analysis

Drug content was determined via UV-spectrophotometer Spekol-1800 (Shimadzu, Japan) at 230 nm for LC-HCl and 271 nm for HCT. TrCl samples were detected at 215 nm via HPLC using a modified method according to the monograph of trospium chloride of the European pharmacopoeia.

An Elite La Chrome HPLC (Hitachi-VWR, Germany) was used, equipped with an autosampler L-2200, an oven L-2300, a pump L-2130, an integrated degasser and a UV detector L-2400. The HPLC system was operated with an Eurospher II 100-5 125 x 4.6 mm nucleosil RP-18 column with integrated pre-column and a particle size of 5 µm (Knauer, Germany). As mobile phase a 5 mmol aqueous sodium dihydrogen phosphate monohydrate buffer (pH 4.9)/acetonitrile (70/30) mixture was selected. The flow rate was set to 1.0 mL/min and the oven temperature to 40 °C. All samples were filtered through a 0.45 µm poly propylene syringe filter. The autosampler injected 20 µl of each sample into the system.

The dead time of the system was determined with a thiourea solution prior to the analysis of the dissolution samples.

Since filtration of the dissolution samples was necessary, a filter adsorption test was carried out and the recovery rate determined. The tests were carried out with three filters and a drug concentration of 0.05 mg/mL. 9 ml of the respective sample were filled into a syringe. The first milliliter of the sample was injected into a HPLC vial unfiltered. Then the syringe was connected to the syringe filter and the next milliliter was injected into the HPLC vial through the filter. This procedure was repeated seven times, resulting in eight samples being filtered in total. After determining the resulting peak area, the recovery rate was calculated according to Equation 7. Filtered solution was discarded until 100% recovery rate was achieved.

$$\text{Recovery rate [\%]} = \frac{\text{Peak area (x mL filtered sample)[a.u.]}}{\text{Peak area (unfiltered sample)[a.u.]}} * 100\ \% \qquad \text{Equation 7}$$

Calibration curves were considered acceptable with an R^2 value of at least 0.999.

5.2.8.14.2 Determination of residual API content

To determine the residual amount of API within an insert after dissolution testing, the inserts were cut into small pieces of approx. 1 mm width and equilibrated under shaking for one week in 25 mL of dem. water. The supernatant was then used for quantification of the respective API. In case residual API amounts were detected, they were added to the previously released API amount from the respective sample and indicated as total drug load of the insert in the cumulative release curves.

5.2.8.15 Dissolution testing

5.2.8.15.1 USP setup

Dissolution studies were performed using the apparatus AT7 smart (Sotax, Switzerland) at 100 rpm with 900.0 mL demineralized water at 37 ± 0.5 °C under sink conditions. For the HCT insert, the dissolution medium was changed latest after 48 h to avoid aqueous degradation of the API (Deventer et al., 2009). The basket method (USP type 1) was utilized to ensure the position of the folded inserts. Drug release was determined via UV-spectrometry at 230 nm for LC-HCl and 271 nm for HCT. TrCl samples were detected at 215 nm via HPLC (see section 5.2.8.14.1).

5.2.8.15.2 Bladder model

The urinal flow of the bladder model was simulated by using a programmable peristaltic pump (Cole-Parmer, UK) with different flowrates according to the respective time-intervals that transfers the dissolution medium into the dissolution vessels. These vessels were realized by glass bladders with urethra and were custom-made to match the physiology of an average adult. Programmable magnetic valves were used to depict the voiding mechanism by draining the medium inside the bladder. They were attached via clamp connection below the outlet of the glass bladders at the end of the urethra. To ensure constant temperature within the bladders, they were surrounded by customized water baths operated via thermostat. Movement was realized by a shaker-platform (Thermo Fisher Scientific, USA) that could be programmed to move at different speeds during day- and nighttime intervals. The pump as well as the valves were controlled by a custom-built control unit. At the center of the control unit was an ESP32 microcontroller. An OLED screen was implemented to display the running time of the experiment as well the currently simulated day time (“day” or “night”).
Samples were drawn manually in case of LC-HCl and HCT or via autosampler (Hanson Vision Autoplus, USA) for TrCl at pre-determined time-points and injected into HPLC-vials. Measurement of the samples was performed as described in section 5.2.8.14.1.

5.2.8.15.3 Application of mathematical models

5.2.8.15.3.1 Release modeling

To investigate the release mechanism of the printed inserts, the dissolution data was analyzed using the Korsmeyer-Peppas equation (Equation 8):

$$\frac{M_t}{M_\infty} = k * t^n \qquad \text{Equation 8}$$

M_t describes the released amount of API at time t in relation to the total drug amount in the matrix M_∞. The constant k represents structural and geometrical properties of the dosage form and the diffusional constant n indicates the underlying release mechanism.

The first 60 % of the drug release curves were used for calculation. Equation 8 can be transformed to Equation 9 by applying the common logarithm:

$$log_{10}\left(\frac{M_t}{M_\infty}\right) = log_{10}k + n\, log_{10}t \qquad \text{Equation 9}$$

The drug release was further described by applying the Higuchi equation:

$$Q = \frac{M_t}{A} = \sqrt{D\,(2c_0 - c_s)c_s t} \qquad \text{Equation 10}$$

Q represents the amount of drug released at time t per unit area A. D stands for the diffusivity of the API in the polymeric matrix, c_0 for the initial drug concentration inside the dosage form and c_s for the saturation solubility of the API in the matrix.

5.2.8.15.3.2 Similarity factor for comparison of dissolution profiles

For comparison of dissolution profiles obtained during short-term stability studies, the f_2 value was used (Shah et al., 1998).

$$f_2 = 50\ x\ log\left\{\left[1 + \frac{1}{n}\sum_{t=1}^{n}(R_t - T_t)^2\right]^{-0.5} x\ 100\right\} \qquad \text{Equation 11}$$

R_t and T_t represent the % mean released amount of API of the reference (here: t0) and test sample (here: t4 under stress conditions). n stands for the number of time points, which needs to be at least 3. A minimum of 7 time points was used to determine the f_2 value.

5.2.8.15.3.3 Mean dissolution time

The mean dissolution time (MDT) was calculated according to Equation 12.

$$MDT = \frac{ABC}{c_\infty} = \frac{\sum_{i=0}^{\infty}\left[(c_{i+1} - c_i)\ x\ \frac{(t_i + t_{i+1})}{2}\right]}{c_\infty} \qquad \text{Equation 12}$$

ABC: area between the curves determined by trapezoidal rule with t as time and c as drug released over time and c_∞ as initial drug load of the inserts.

For determination of the MDT, the mean drug release of triplicate measurements for a maximum drug release of 80% was used.

5.2.8.16 Viscosity measurements

5.2.8.16.1 General procedure

Rheological measurements were performed with a rheometer (Kinexus pro, Malvern Instruments, UK) by using a plate (Ø 20 mm) and plate geometry (Ø 55 mm) with a solvent trap saturated with THF. The gap width was set according to the particle size of the incorporated API to 2 mm to avoid scratching of the applied geometries. To keep the measurement conditions constant and close to the applied printing conditions, the temperature was set to 35 °C. For data analysis, the software rSpace (version 1.61, Malvern Instruments, UK) was used.

5.2.8.16.2 Rotational rheometry

To investigate the rheological behavior of the semi-solid formulations, a shear ramp was recorded from 0.01 to 100 s^{-1} and 100 to 0.01 s^{-1} at logarithmic intervals.
The Hershel-Bulkley equation was used to fit the so obtained data.

Creep recovery was determined by applying a shear rate of 0.01 s^{-1} for 1-2 minutes, followed by 100 s^{-1} for 2 min to mimic one printing cycle and lastly 0.01 s^{-1} for 10 minutes of recovery time.

5.2.8.16.3 Oscillatory rheometry

Amplitude sweeps were carried out at a frequency of 1 Hz from 0.01 - 100 % shear strain to determine the limits of the linear viscoelastic region. Semi-solid formulations with EVA and PCL in varying solvent contents (30-70 % for EVA and 30-50 % for PCL) were used for measurements as well as the standard formulations with 10 % of added API (LC-HCl, TrCl and HCT). The formulations were prepared as described in section 5.2.1. The phase angle, the loss factor tan δ (see Equation 13), and complex shear viscosity were determined at 0.1 % complex shear strain to characterize the formulations in the linear viscoelastic region, unless stated otherwise.

$$\tan\delta = \frac{G'}{G''} \qquad \text{Equation 13}$$

$\tan\delta$ = loss factor, G' = storage modulus, G'' = loss modulus

G’ and G” were plotted against the complex shear strain.

5.2.8.17 Particle size measurements

Particle size distributions were determined via laser diffraction (Mastersizer 3000, Malvern Panalytical, UK) using a sample size of 5 g and pressurized air of 4 bar. The data was analyzed with the software Mastersizer 3000 (Malvern Panalytical, UK) and the x10, x50 and x90 were calculated. Measurements were carried out in triplicate.

5.2.8.18 Solubility determinations

Solubility of the APIs was determined in triplicate by applying the shake-flask method (Glomme et al., 2005) with purified water or THF. Therefore, 100 mL amber glass flasks equipped with magnetic stirrers were operated at ambient conditions or inside of a water bath at 37 ± 0.5 °C. The saturated solutions were stirred until equilibrium was reached. The dissolved amount of API was quantified via UV or HPLC measurements as described in section 5.2.8.14.

5.2.8.19 FT-IR measurements

A Tensor II Fourier-transformed infrared spectrometer (Bruker, USA), equipped with a Platinum ATR (Bruker, USA) single reflection diamond unit was used to investigate possible drug-polymer interactions. Data was evaluated with the Opus 7.5 software (Bruker, USA). 128 scans were averaged for each sample in the wavenumber region of 400-4000 cm^{-1} after subtracting the background. The resolution was set to 4 cm^{-1} and the scans were normalized to the peak maximum. Scans were made from pure API, excipients, and printed inserts.

5.2.9 Short-term stability study

10 % TrCl-loaded EVA and PCL-PEG inserts were subjected to stability testing for four weeks. The samples were stored at ambient conditions and at 40 °C and 75 % relative humidity in open Petri dishes. At the start of the study and after 4 weeks, dissolution studies and testing of the mechanical properties (see section 5.2.8.13.2) were performed. SEM images of cross-sections and the surface of the inserts were taken to investigate morphological changes.

6 Appendix

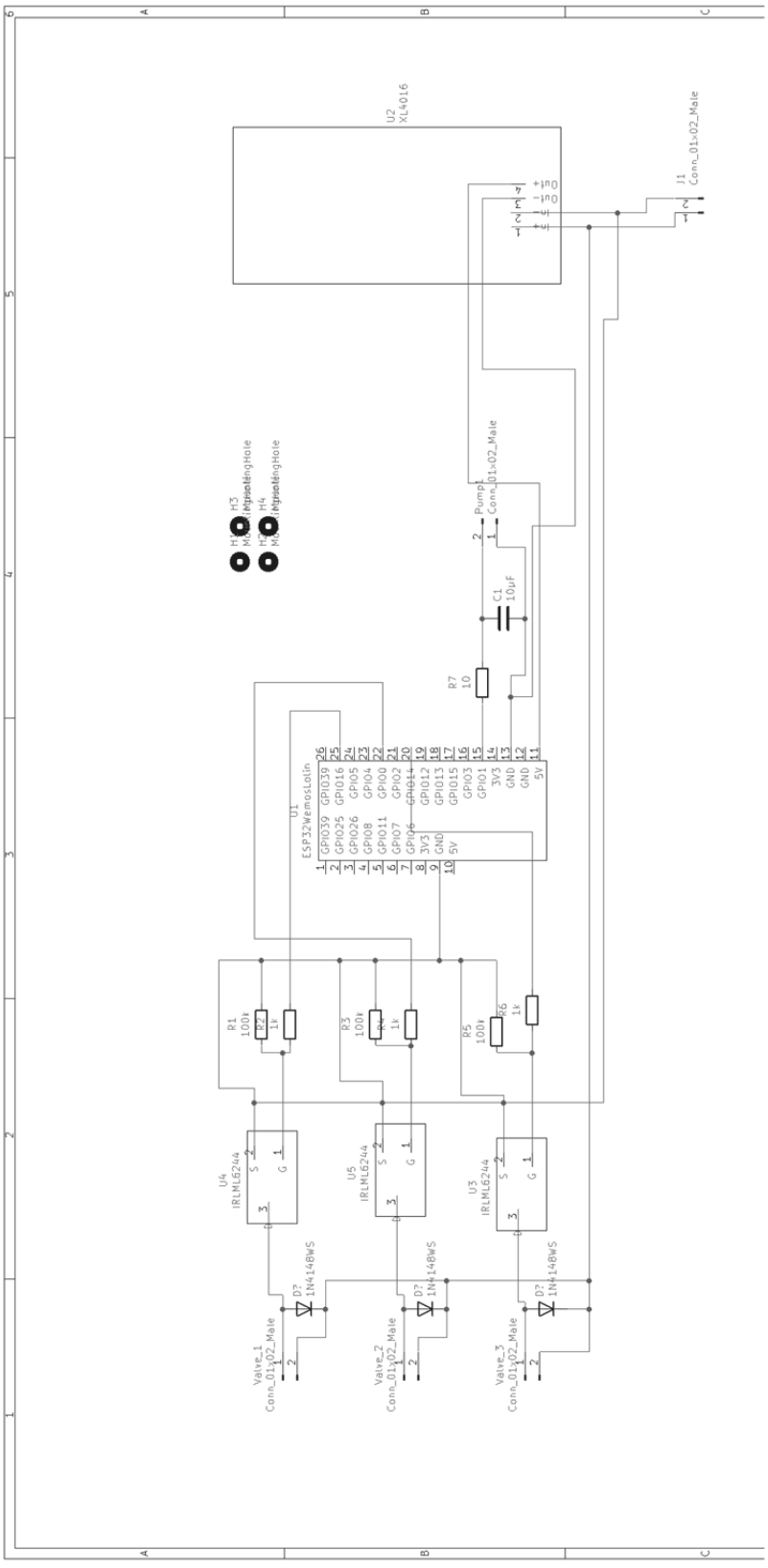

Figure 74. Circuit diagram of bladder model.

Code implemented for programming of the bladder model:

```
#include "SSD1306.h"
SSD1306  display(0x3c, 5, 4);

//setting PWM properties
const int freq = 20000;
const int ledChannel = 0;
const int resolution = 8;

// controling pump and valve for bladder dissolution model

long hours = 3600000;
long seconds = 1000;
long minutes = 60000;
String daytime = "day";

// First: set time interval and duration of valve opening
long day_length = 16 * hours; // enter length of night/sleep during which pump rate is increased and

// Second: set pump speed for day and night. Recommended: 255/127 and adjusting by calibration in the pump menu
const int pump_speed_day = 255; // pump speed during the day
const int pump_speed_night = 127; // pump speed for the night

int Valve1Pin = 16;
int Valve2Pin = 0;
int Valve3Pin = 14;
int valveState = LOW;
unsigned long currentMillis;
long previousMillis = 0;
long t;
const int PumpPin = 1;

void setup() {
  display.init();
  display.setFont(ArialMT_Plain_24);
  pinMode(PumpPin, OUTPUT);
  pinMode(Valve1Pin, OUTPUT);
  pinMode(Valve2Pin, OUTPUT);
  pinMode(Valve3Pin, OUTPUT);
  ledcSetup(ledChannel, freq, resolution);
  ledcAttachPin(PumpPin, ledChannel);
  ledcWrite(ledChannel, pump_speed_night);
}

void loop() {
  currentMillis = millis();
  t = currentMillis % 86400000;

  if (t < day_length)
  {
      daytime = "day";
```

```
 }

 if (t >= day_length)
 {
     daytime = "night";
 }

 if (daytime == "night")
 {
  ledcWrite(ledChannel, pump_speed_night);
 }

 if (daytime == "day")
 {
  ledcWrite(ledChannel, pump_speed_day);
 }

 if ((t < 2*minutes) or
    ((t > 240*minutes) and (t < 242*minutes)) or
    ((t > 480*minutes) and (t < 482*minutes)) or
    ((t > 720*minutes) and (t < 722*minutes)) or
    ((t > 960*minutes) and (t < 962*minutes))){

       valveState = HIGH;
       digitalWrite(Valve1Pin, HIGH);
       digitalWrite(Valve2Pin, HIGH);
       digitalWrite(Valve3Pin, HIGH);
     }

 else {
  valveState = LOW;
  digitalWrite(Valve1Pin, LOW);
  digitalWrite(Valve2Pin, LOW);
  digitalWrite(Valve3Pin, LOW);
 }

 if (daytime == "night")
  {
  ledcWrite(ledChannel, pump_speed_night);
  }

 if (daytime == "day")
  {
  ledcWrite(ledChannel, pump_speed_day);
  }

display.clear();
display.drawString(0,  0,  daytime+":  "+String(int(currentMillis/86400000))+"\n"+(t/3600000)+"h  "
+((t/60000)%60)+ "min");
display.display();
}
```

7 References

Abrams, P., Kelleher, C.J., Kerr, L.A., Rogers, R.G., 2000. Overactive bladder significantly affects quality of life. Am. J. Manag. Care 6.

Aho, J., Boetker, J.P., Baldursdottir, S., Rantanen, J., 2015. Rheology as a tool for evaluation of melt processability of innovative dosage forms. Int. J. Pharm. 494, 623–642.

Azad, M.A., Olawuni, D., Kimbell, G., Badruddoza, A.M., Hossain, M.S., Sultana, T., 2020. Polymers for extrusion-based 3D printing of pharmaceuticals: A holistic materials-process perspective. Pharmaceutics 12.

Babu, G., Babu, P., Sirisha, P., 2014. Conceptuation, formulation and evaluation of sustained release floating tablets of captopril compression coated with gastric dispersible hydrochlorothiazide using 2 3 factorial design . Int. J. Pharm. Investig. 4, 77.

Bassand, C., Verin, J., Lamatsch, M., Siepmann, F., Siepmann, J., 2022. How agarose gels surrounding PLGA implants limit swelling and slow down drug release. J. Control. Release 343, 255–266.

Benner, J.S., Nichol, M.B., Rovner, E.S., Jumadilova, Z., Alvir, J., Hussein, M., Fanning, K., Trocio, J.N., Brubaker, L., 2010. Patient-reported reasons for discontinuing overactive bladder medication. BJU Int 105, 1276–1282.

Bhise, N.S., Manoharan, V., Massa, S., Tamayol, A., Ghaderi, M., Miscuglio, M., Lang, Q., Zhang, Y.S., Shin, S.R., Calzone, G., Annabi, N., Shupe, T.D., Bishop, C.E., Atala, A., Dokmeci, M.R., Khademhosseini, A., 2016. A liver-on-a-chip platform with bioprinted hepatic spheroids. Biofabrication 8.

Brown, C.K., Friedel, H.D., Barker, A.R., Buhse, L.F., Keitel, S., Cecil, T.L., Kraemer, J., Morris, J.M., Reppas, C., Stickelmeyer, M.P., Yomota, C., Shah, V.P., 2011. FIP/AAPS joint workshop report: dissolution/in vitro release testing of novel/special dosage forms. AAPS PharmSciTech 12, 782–794.

Chae, S., Kim, J., Yi, H., 2022. 3D Bioprinting of an in vitro model of a biomimetic urinary bladder with a contract-release system.

Chancellor, M.B., 2001. Future trends in the treatment of urinary incontinence. Rev. Urol. 3, 27–34.

Chang, R., Emami, K., Wu, H., Sun, W., 2010. Biofabrication of a three-dimensional liver micro-organ as an in vitro drug metabolism model. Biofabrication 2.

Chen, D., Song, D., Wientjes, M.G., Au, J.L.S., 2003. Effect of dimethyl sulfoxide on bladder tissue penetration of intravesical paclitaxel. Clin. Cancer Res. 9, 363–369.

Cheng, Y., Qin, H., Acevedo, N.C., Shi, X., 2020. Development of methylcellulose-based sustained-release dosage by semisolid extrusion additive manufacturing in drug delivery system. J. Biomed. Mater. Res. - Part B Appl. Biomater.

Chess-Williams, R., 2002. Muscarinic receptors of the urinary bladder: Detrusor, urothelial and prejunctional. Auton. Autacoid Pharmacol. 22, 133–145.

Cho, C.-W., Choi, J.-S., Shin, S.-C., 2007. Controlled release of pranoprofen from the ethylene-vinyl

acetate matrix using plasticizer. Drug Dev. Ind. Pharm. 33, 747–753.

Chung, J.H.Y., Naficy, S., Yue, Z., Kapsa, R., Quigley, A., Moulton, S.E., Wallace, G.G., 2013. Bio-ink properties and printability for extrusion printing living cells. Biomater. Sci. 1, 763–773.

Cima, M.J., Lee, H., Daniel, K., Tanenbaum, L.M., Mantzavinou, A., Spencer, K.C., Ong, Q., Sy, J.C., Santini, J., Schoellhammer, C.M., Blankschtein, D., Langer, R.S., 2014. Single compartment drug delivery. J. Control. Release 190, 157–171.

Conceição, J., Farto-Vaamonde, X., Goyanes, A., Adeoye, O., Concheiro, A., Cabral-Marques, H., Sousa Lobo, J.M., Alvarez-Lorenzo, C., 2019. Hydroxypropyl-β-cyclodextrin-based fast dissolving carbamazepine printlets prepared by semisolid extrusion 3D printing. Carbohydr. Polym. 221, 55–62.

Costa, P., Sousa Lobo, J.M., 2001. Modeling and comparison of dissolution profiles. Eur. J. Pharm. Sci. 13, 123–133.

Coyne, K.S., Sexton, C.C., Irwin, D.E., Kopp, Z.S., Kelleher, C.J., Milsom, I., 2008. The impact of overactive bladder, incontinence and other lower urinary tract symptoms on quality of life, work productivity, sexuality and emotional well-being in men and women: Results from the EPIC study. BJU Int. 101, 1388–1395.

Crane, A., Isharwal, S., Zhu, H., 2018. Current therapeutic strategies in clinical urology. Mol. Pharm. 15, 3010–3019.

da Silva Anacleto, S., Borges, M.M.C., de Oliveira, H.L., Vicente, A.R., de Figueiredo, E.C., de Oliveira, M.A.L., Pinheiro Borges, B.J., de Oliveira, M.A., de Souza Borges, W., Bastos Borges, K., 2018. Evaluation of physicochemical properties as supporting information on quality control of raw materials and veterinary pharmaceutical formulations. J. Pharm. Anal. 8, 168–175.

Darney, P.D., Monroe, S.E., Klaisle, C.M., Alvarado, A., 1989. Clinical evaluation of the Capronor contraceptive implant: Preliminary report. Am. J. Obstet. Gynecol. 160, 1292–1295.

Deventer, K., Baele, G., Van Eenoo, P., Pozo, O.J., Delbeke, F.T., 2009. Stability of selected chlorinated thiazide diuretics. J. Pharm. Biomed. Anal. 49, 519–524.

Di Stasi, S.M., Giannantoni, A., Stephen, R.L., Capelli, G., Navarra, P., Massoud, R., Vespasiani, G., 2003. Intravesical electromotive mitomycin C versus passive transport mitomycin C for high risk superficial bladder cancer: A prospective randomized study. J. Urol. 170, 777–782.

Dores, F., Kuźmińska, M., Soares, C., Bohus, M., A Shervington, L., Habashy, R., Pereira, B.C., Peak, M., Isreb, A., Alhnan, M.A., 2020. Temperature and solvent facilitated extrusion based 3D printing for pharmaceuticals. Eur. J. Pharm. Sci. 152.

Doroshyenko, O., Jetter, A., Odenthal, K.P., Fuhr, U., 2005. Clinical pharmacokinetics of trospium chloride. Clin. Pharmacokinet. 44, 701–720.

Dressman, J.B., Amidon, G.L., Reppas, C., Shah, V.P., 1998. Dissolution testing as a prognostic tool for oral drug absorption: immediate release dosage forms. Pharm. Res. 15, 11–22.

Duan, B., Hockaday, L.A., Kang, K.H., Butcher, J.T., 2013. 3D Bioprinting of heterogeneous aortic valve conduits with alginate/gelatin hydrogels. J. Biomed. Mater. Res. - Part A 101 A, 1255–1264.

El Aita, I., Breitkreutz, J., Quodbach, J., 2019. On-demand manufacturing of immediate release levetiracetam tablets using pressure-assisted microsyringe printing. Eur. J. Pharm. Biopharm. 134, 29–36.

El Aita, I., Rahman, J., Breitkreutz, J., Quodbach, J., 2020. 3D-Printing with precise layer-wise dose adjustments for paediatric use via pressure-assisted microsyringe printing. Eur. J. Pharm. Biopharm. 157, 59–65.

Evans, R., Kohan, A., Moldwin, R., Radecki, D., Geib, T., Peters, K.M., 2021. Safety, tolerability, and efficacy of LiRIS 400 mg in women with interstitial cystitis/bladder pain syndrome with or without Hunner lesions. Neurourol. Urodyn. 40, 1730–1739.

Fraser, M.O., Lavelle, J.P., Sacks, M.S., Chancellor, M.B., 2002. The future of bladder control-intravesical drug delivery, a pinch of pepper, and gene therapy. Rev. Urol. 4, 1–11.

Fu, J., Yu, X., Jin, Y., 2018. 3D printing of vaginal rings with personalized shapes for controlled release of progesterone. Int. J. Pharm. 539, 75–82.

Genina, N., Holländer, J., Jukarainen, H., Mäkilä, E., Salonen, J., Sandler, N., 2016. Ethylene vinyl acetate (EVA) as a new drug carrier for 3D printed medical drug delivery devices. Eur. J. Pharm. Sci. 90, 53–63.

Giglio, D., Tobin, G., 2009. Muscarinic receptor subtypes in the lower urinary tract. Pharmacology 83, 259–269.

Gillispie, G., Prim, P., Copus, J., Fisher, J., Mikos, A.G., Yoo, J.J., Atala, A., Lee, S.J., 2020. Assessment methodologies for extrusion-based bioink printability. Biofabrication 12.

Glomme, A., März, J., Dressman, J.B., 2005. Comparison of a miniaturized shake-flask solubility method with automated potentiometric acid/base titrations and calculated solubilities. J. Pharm. Sci. 94, 1–16.

Gormley, E.A., Lightner, D.J., Burgio, K.L., Chai, T.C., Clemens, J.Q., Culkin, D.J., Das, A.K., Foster, H.E., Scarpero, H.M., Tessier, C.D., Vasavada, S.P., 2012. Diagnosis and treatment of overactive bladder (non-neurogenic) in adults: AUA/SUFU guideline. J. Urol. 188, 2455–2463.

Griffith, D.P., Musher, D.M., Itin, C., 1976. Urease. The primary cause of infection-induced urinary stones. Invest Urol 13, 346–350.

Guay, D.R., 2005. Trospium chloride: an update on a quaternary anticholinergic for treatment of urge urinary incontinence. Ther. Clin. Risk Manag. 1, 157–166.

Haupt, M., 2013. Entwicklung intravesikaler Systeme zur verlängerten Arzneistoffabgabe für die lokale Behandlung der überaktiven Harnblase. Dissertation, Heinrich-Heine-Universität Düsseldorf.

Haupt, M., Thommes, M., Heidenreich, A., Breitkreutz, J., 2013. Lipid-based intravesical drug delivery systems with controlled release of trospium chloride for the urinary bladder. J Control Release 170, 161–166.

Haylen, B.T., De Ridder, D., Freeman, R.M., Swift, S.E., Berghmans, B., Lee, J., Monga, A., Petri, E., Rizk, D.E., Sand, P.K., Schaer, G.N., 2010. An International Urogynecological Association (IUGA)/International Continence Society (ICS) joint report on the terminology for female pelvic floor dysfunction. Int. Urogynecol. J. 21, 5–26.

Heinen, C.A., Reuss, S., Amidon, G.L., Langguth, P., 2013. Ion pairing with bile salts modulates intestinal permeability and contributes to food-drug interaction of BCS class III compound trospium chloride. Mol. Pharm. 10, 3989–3996.

Higuchi, T., 1963a. Mechanism of sustained-action medication. Theoretical analysis of rate of release of solid drugs dispersed in solid matrices. J. Pharm. Sci. 52, 1145–1149.

Higuchi, T., 1963b. Mechanism of sustained-action medication. Theoretical analysis of rate of release of solid drugs dispersed in solid matrices. J. Pharm. Sci. 52, 1145–1149.

ICH Expert Working Group, 2021. ICH Harmonised Guideline - Impurities: Guideline for Residual Solvents Q3C(R8), International Council for Harmonisation of Technical Requirements for Pharmaceuticals for Human Use (ICH).

Jacob, S., Nair, A.B., Patel, V., Shah, J., 2020. 3D printing technologies: Recent development and emerging applications in various drug delivery systems. AAPS PharmSciTech 21, 220.

Januskaite, P., Xu, X., Ranmal, S.R., Gaisford, S., Basit, A.W., Tuleu, C., Goyanes, A., 2020. I spy with my little eye: A paediatric visual preferences survey of 3D printed tablets. Pharmaceutics 12, 1100.

Jayarajan, J., Radomski, S.B., 2013. Pharmacotherapy of overactive bladder in adults: A review of efficacy, tolerability, and quality of life. Res. Reports Urol. 6.

Kaldybekov, D.B., Tonglairoum, P., Opanasopit, P., Khutoryanskiy, V. V, 2018. Mucoadhesive maleimide-functionalised liposomes for drug delivery to urinary bladder. Eur. J. Pharm. Sci. 111, 83–90.

Kazmierska, K.A., Thompson, R., Morris, N., Long, A., Ciach, T., 2010. In vitro multicompartmental bladder model for assessing blockage of urinary catheters: Effect of hydrogel coating on dynamics of proteus mirabilis growth. Urology 76, 515.e15-515.e20.

Khaled, S.A., Alexander, M.R., Wildman, R.D., Wallace, M.J., Sharpe, S., Yoo, J., Roberts, C.J., 2018. 3D extrusion printing of high drug loading immediate release paracetamol tablets. Int. J. Pharm. 538, 223–230.

Khaled, S.A., Burley, J.C., Alexander, M.R., Roberts, C.J., 2014. Desktop 3D printing of controlled release pharmaceutical bilayer tablets. Int. J. Pharm. 461, 105–111.

Khaled, S.A., Burley, J.C., Alexander, M.R., Yang, J., Roberts, C.J., 2015. 3D printing of tablets containing multiple drugs with defined release profiles. Int. J. Pharm. 494, 643–650.

Kolawole, O.M., Lau, W.M., Mostafid, H., Khutoryanskiy, V. V., 2017. Advances in intravesical drug delivery systems to treat bladder cancer. Int. J. Pharm. 532, 105–117.

Konta, A.A., García-Piña, M., Serrano, D.R., 2017. Personalised 3D printed medicines: Which techniques and polymers are more successful? Bioengineering 4.

Korossis, S., Bolland, F., Ingham, E., Fisher, J., Kearney, J., Southgate, J., 2006. Tissue engineering of the urinary bladder: Considering structure-function relationships and the role of mechanotransduction. Tissue Eng. 12, 635–644.

Korte, C., Quodbach, J., 2018. 3D-Printed network structures as controlled-release drug delivery systems: dose adjustment, API release analysis and prediction. AAPS PharmSciTech.

Kwon, K., Mcmahon, S., Duffy, P., Wang, W., Cameron, R.E., 2013. PEG-functionalization of poly(L-lactide-co-caprolactone)copolymers : a method for tuning degradation rate, in: Poster Presentation.

Laar, N., 2009. Entwicklung und Validierung eines resorbierbaren Drug-Delivery-Systems für die Harnblase. Dissertation, Technische Universität München.

Landers, R., Mülhaupt, R., 2000. Desktop manufacturing of complex objects, prototypes and biomedical scaffolds by means of computer-assisted design combined with computer-guided 3D plotting of polymers and reactive oligomers. Macromol. Mater. Eng. 282, 17–21.

Lee, H., Cima, M.J., 2011. An intravesical device for the sustained delivery of lidocaine to the bladder. J. Control. Release 149, 133–139.

Lee, S.H., Choy, Y.B., 2016. Implantable devices for sustained, intravesical drug delivery. Int. Neurourol. J. 20, 101–106.

Liabeuf, S., Gras, V., Moragny, J., Durand-Maugard, C., Masmoudi, K., Andréjak, M., 2014. Trospium chloride for overactive bladder may induce central nervous system adverse events. Eur. Geriatr. Med. 5, 220–224.

Lightner, D.J., Gomelsky, A., Souter, L., Vasavada, S.P., 2019. Diagnosis and treatment of overactive bladder (non-neurogenic) in adults: AUA/SUFU guideline amendment 2019. J. Urol. 202, 558–563.

Ligon, S.C., Liska, R., Stampfl, J., Gurr, M., Mülhaupt, R., 2017. Polymers for 3D Printing and Customized Additive Manufacturing. Chem. Rev. 117, 10212–10290.

Linares, V., Casas, M., Caraballo, I., 2019. Printfills: 3D printed systems combining fused deposition modeling and injection volume filling. Application to colon-specific drug delivery. Eur J Pharm Biopharm 134, 138–143.

Lippert, H., Herbold, D., Lippert-Burmester, W., 2010. Anatomie: Text und Atlas, 9. Auflage. ed. Urban & Fischer Verlag/Elsevier GmbH.

Lucero-Acuña, A., Gutiérrez-Valenzuela, C.A., Esquivel, R., Guzmán-Zamudio, R., 2019. Mathematical modeling and parametrical analysis of the temperature dependency of control drug release from biodegradable nanoparticles. RSC Adv. 9, 8728–8739.

Madaus, 2014. Fachinformation Spasmolyt 10mg/20mg 1–3.

Madersbacher, H., Rovner, E., 2006. Trospium chloride: The European experience. Expert Opin. Pharmacother. 7, 1373–1380.

Mahadevan, V., 2019. Anatomy of the lower urinary tract. Surgery 37, 351–358.

Marinkovic, S.P., Rovner, E.S., Moldwin, R.M., Stanton, S.L., Gillen, L.M., Marinkovic, C.M., 2012. The management of overactive bladder syndrome. BMJ 344, 1–7.

Markl, D., Strobel, A., Schlossnikl, R., Bøtker, J., Bawuah, P., Ridgway, C., Rantanen, J., Rades, T., Gane, P., Peiponen, K.E., Zeitler, J.A., 2018. Characterisation of pore structures of pharmaceutical tablets: A review. Int. J. Pharm. 538, 188–214.

Marques, C.F., Olhero, S.M., Torres, P.M.C., Abrantes, J.C.C., Fateixa, S., Nogueira, H.I.S., Ribeiro, I.A.C., Bettencourt, A., Sousa, A., Granja, P.L., Ferreira, J.M.F., 2019. Novel sintering-free scaffolds obtained by additive manufacturing for concurrent bone regeneration and drug delivery: Proof of concept. Mater. Sci. Eng. C 94, 426–436.

Matai, I., Kaur, G., Seyedsalehi, A., McClinton, A., Laurencin, C.T., 2020. Progress in 3D bioprinting technology for tissue/organ regenerative engineering. Biomaterials 226.

Mckellar, K., Bellin, E., Schoenbaum, E., Abraham, N., 2019. Prevalence, risk factors, and treatment for overactive bladder in a racially diverse population. Urology 126, 70–75.

McKiernan, J.M., Barlow, L.J., Laudano, M.A., Mann, M.J., Petrylak, D.P., Benson, M.C., 2011. A phase I trial of intravesical nanoparticle albumin-bound paclitaxel in the treatment of bacillus Calmette-Guérin refractory nonmuscle invasive bladder cancer. J. Urol. 186, 448–451.

Melocchi, A., Inverardi, N., Uboldi, M., Baldi, F., Maroni, A., Pandini, S., Briatico-Vangosa, F., Zema, L., Gazzaniga, A., 2019. Retentive device for intravesical drug delivery based on water-induced shape memory response of poly(vinyl alcohol): design concept and 4D printing feasibility. Int. J. Pharm. 559, 299–311.

Michel, M.C., Barendrecht, M.M., 2008. Physiological and pathological regulation of the autonomic control of urinary bladder contractility. Pharmacol. Ther. 117, 297–312.

Michel, M.C., Oelke, M., Peters, S.L.M., 2005. The neuro-urological connection. Eur. Urol. Suppl. 4, 18–28.

Milsom, I., Abrams, P., Cardozo, L., Roberts, R.G., Thuroff, J., Wein, A.J., 2001. How widespread are the symptoms of an overactive bladder and how are they managed? A population-based prevalence study. BJU Int 87, 760–766.

Milsom, I., Gyhagen, M., 2019. The prevalence of urinary incontinence. Climacteric 22, 217–222.

Mouser, V.H.M., Melchels, F.P.W., Visser, J., Dhert, W.J.A., Gawlitta, D., Malda, J., 2016. Yield stress determines bioprintability of hydrogels based on gelatin-methacryloyl and gellan gum for cartilage bioprinting. Biofabrication 8.

Mülhaupt, R., Landers, R., John, H., 2001. Device and methods for the production of three-dimensional objects. WO 01/78968 A1.

Murphy, A.M., Krlin, R.M., Goldman, H.B., 2013. Treatment of overactive bladder: What is on the horizon? Int. Urogynecol. J. Pelvic Floor Dysfunct. 24, 5–13.

Nickel, J.C., Jain, P., Shore, N., Anderson, J., Giesing, D., Lee, H., Kim, G., Daniel, K., White, S., Larrivee-Elkins, C., Lekstrom-Himes, J., Cima, M., 2012. Continuous intravesical lidocaine treatment for interstitial cystitis/bladder pain syndrome: safety and efficacy of a new drug delivery device. Sci. Transl. Med. 4, 143ra100-143ra100.

Nicolson, P., Kopp, Z., Chapple, C.R., Kelleher, C., 2008. It's just the worry about not being able to control it! A qualitative study of living with overactive bladder. Br. J. Health Psychol. 13, 343–359.

Nirmal, J., Chuang, Y.-C., Tyagi, P., Chancellor, M.B., 2012. Intravesical therapy for lower urinary tract symptoms. Urol. Sci. 23, 70–77.

O'Connell, C., Ren, J., Pope, L., Li, Y., Mohandas, A., Blanchard, R., Duchi, S., Onofrillo, C., 2020. Characterizing bioinks for extrusion bioprinting: Printability and rheology. Methods Mol. Biol.

Organon, 2022. NuvaRing [WWW Document]. URL https://www.nuvaring.com/ (accessed 07.2022)

Ouslander, J.G., 2004. Management of overactive bladder. N. Engl. J. Med. 350, 786–799.

Ouyang, L., Yao, R., Zhao, Y., Sun, W., 2016. Effect of bioink properties on printability and cell viability for 3D bioplotting of embryonic stem cells. Biofabrication 8.

Ozbolat, I.T., 2016. 3D Bioprinting: Fundamentals, principles and applications. Elsevier Inc., San Diego, pp. 1–342.

Palugan, L., Cerea, M., Cirilli, M., Moutaharrik, S., Maroni, A., Zema, L., Melocchi, A., Uboldi, M., Filippin, I., Foppoli, A., Gazzaniga, A., 2021. Intravesical drug delivery approaches for improved therapy of urinary bladder diseases. Int. J. Pharm. X 3, 100100.

Paxton, N., Smolan, W., Böck, T., Melchels, F., Groll, J., Jungst, T., 2017. Proposal to assess printability of bioinks for extrusion-based bioprinting and evaluation of rheological properties governing bioprintability. Biofabrication 9.

Pedraza Sanchez, J.P., Mazuecos-Quiros, J., García-Sánchez, C., Barrero-Candau, R., Torrubia-Romero, F.J., Medina-López, R.A., 2019. Intra-urethral lidocaine gel versus intravesical alkalinized lidocaine as anaesthesia in the ambulatory intradetrusor injection of botulinum toxin (BoNTA): A prospective study. Eur. Urol. Suppl. 18, e165–e166.

Peppas, N.A., Sahlin, J.J., 1989. A simple equation for the description of solute release. III. Coupling of diffusion and relaxation. Int. J. Pharm. 57, 169–172.

Ph. Eur. 10, 2020a. Hydrochlorothiazide. European Directorate for the Quality of Medicines (EDQM), Strasbourg, France.

Ph. Eur. 10, 2020b. 2.9.3. Dissolution test for solid dosage forms. European Directorate for the Quality of Medicines (EDQM), Strasbourg, France.

Ph. Eur. 10, 2020c. Parenteral preparations. European Directorate for the Quality of Medicines (EDQM), Strasbourg, France.

Pietrzak, K., Isreb, A., Alhnan, M., 2015. A flexible-dose dispenser for immediate and extended release 3D printed tablets. Eur. J. Pharm. Biopharm. 96, 380–387.

Radomski, S.B., Barkin, J., 2012. Medical management of overactive bladder. Can. J. Urol. 19, 2–9.

Rahman-Yildir, J., Fischer, B., Breitkreutz, J., 2022a. Development of sustained-release drug-loaded intravesical inserts via semi-solid micro-extrusion 3D-printing for bladder targeting. Int. J. Pharm. 622, 121849.

Rahman-Yildir, J., Wiedey, R., Breitkreutz, J., 2022b. Comparative dissolution studies of 3D-printed inserts in a novel biopharmaceutical bladder model. Int. J. Pharm. 624.

Rahman, J., Quodbach, J., 2021. Versatility on demand – The case for semi-solid micro-extrusion in pharmaceutics. Adv. Drug Deliv. Rev. 172, 104–126.

Raju, P.N., Prakash, K., Rao, T.R., Reddy, B.C.S., Sreenivasulu, V., Narasu, M.L., 2014. Effect of tablet surface area and surface area / volume on drug release from lamivudine extended release matrix tablets.

Ritger, P.L., Peppas, N.A., 1987. A simple equation for description of solute release I. Fickian and non-fickian release from non-swellable devices in the form of slabs, spheres, cylinders or discs. J. Control. release 5, 23–36.

Robertson, G.L., 1995. Diabetes insipidus. Endocrinol. Metab. Clin. North Am. 24, 549–572.

Robinson, D., Giarenis, I., Cardozo, L., 2013. New developments in the medical management of overactive bladder. Maturitas 76, 225–229.

Rowe, C.W., Katstra, W.E., Palazzolo, R.D., Giritlioglu, B., Teung, P., Cima, M.J., 2000. Multimechanism oral dosage forms fabricated by three dimensional printing(TM). J. Control. Release 66, 11–17.

Ruffion, A., Castro-Diaz, D., Patel, H., Khalaf, K., Onyenwenyi, A., Globe, D., LeReun, C., Teneishvili, M., Edwards, M., 2013. Systematic review of the epidemiology of urinary incontinence and detrusor overactivity among patients with neurogenic overactive bladder. Neuroepidemiology 41, 146–155.

Sanphui, P., Rajput, L., 2014. Tuning solubility and stability of hydrochlorothiazide co-crystals. Acta Crystallogr B Struct Sci Cryst Eng Mater 70, 81–90.

Schindelin, J., Arganda-Carreras, I., Frise, E., Kaynig, V., Longair, M., Pietzsch, T., Preibisch, S., Rueden, C., Saalfeld, S., Schmid, B., Tinevez, J.Y., White, D.J., Hartenstein, V., Eliceiri, K., Tomancak, P., Cardona, A., 2012. Fiji: An open-source platform for biological-image analysis. Nat. Methods 9, 676–682.

Schneider, C., Langer, R., Loveday, D., Hair, D., 2017. Applications of ethylene vinyl acetate copolymers (EVA) in drug delivery systems. J. Control. Release 262, 284–295.

Schulz, A., Vestweber, A.M., Leis, W., Stark, D., Dressler, D., 2008. An improved model of a catheterised human bladder for screening bactericidal agents. Aktuelle Urol. 39, 53–57.

Schwab, A., Levato, R., D'Este, M., Piluso, S., Eglin, D., Malda, J., 2020. Printability and shape fidelity of bioinks in 3D bioprinting. Chem. Rev. 120, 11028–11055.

Setiyorini, Y., Lou, X., Pintowantoro, S., 2012. The influence of temperature and drug concentrations prednisolone in NIPAAm copolymer. Procedia Chem. 4, 336–342.

Shah, V.P., Tsong, Y., Sathe, P., Liu, J.-P., 1998. In vitro dissolution profile comparison—Statistics and analysis of the similarity factor, f2. Pharm. Res. 15, 889–896.

Sharma, S., Basu, B., 2022. Biomaterials assisted reconstructive urology: The pursuit of an implantable bioengineered neo-urinary bladder. Biomaterials 281, 121331.

Siepmann, J., Elkharraz, K., Siepmann, F., Klose, D., 2005. How autocatalysis accelerates drug release from PLGA-based microparticles: A quantitative treatment. Biomacromolecules 6, 2312–2319.

Siepmann, J., Peppas, N.A., 2011. Higuchi equation: Derivation, applications, use and misuse. Int. J. Pharm. 418, 6–12.

Siepmann, J., Siepmann, F., 2012. Modeling of diffusion controlled drug delivery. J. Control. Release 161, 351–362.

Siewert, M., Dressman, J., Brown, C.K., Shah, V.P., 2003. FIP/AAPS guidelines for dissolution/in vitro release testing of novel/special dosage forms. AAPS PharmSciTech 4, 43–52.

Sinha, P., Datar, A., Jeong, C., Deng, X., Chung, Y.G., Lin, L.C., 2019. Surface area determination of porous materials using the Brunauer-Emmett-Teller (BET) method: limitations and improvements. J. Phys. Chem. C 123, 20195–20209.

Sládková, V., Skalická, T., Skořepová, E., Čejka, J., Eigner, V., Kratochvíl, B., 2015. Systematic solvate screening of trospium chloride: discovering hydrates of a long-established pharmaceutical. CrystEngComm 17, 4712–4721.

Speer, I., Preis, M., Breitkreutz, J., 2019. Dissolution testing of oral film preparations: Experimental comparison of compendial and non-compendial methods. Int. J. Pharm. 561, 124–134.

Stewart, S.A., Domínguez-Robles, J., McIlorum, V.J., Mancuso, E., Lamprou, D.A., Donnelly, R.F., Larrañeta, E., 2020. Development of a biodegradable subcutaneous implant for prolonged drug delivery using 3D printing. Pharmaceutics 12.

Stickler, D.J., Morris, N.S., Winters, C., 1999. Simple physical model to study formation and physiology of biofilms on urethral catheters, in: Methods in Enzymology. Academic Press, pp. 494–501.

Tirella, A., Orsini, A., Vozzi, G., Ahluwalia, A., 2009. A phase diagram for microfabrication of geometrically controlled hydrogel scaffolds. Biofabrication 1.

Tubaro, A., 2004. Defining overactive bladder: Epidemiology and burden of disease. Urology 64, 2–6.

Tyagi, P., Kashyap, M., Hensley, H., Yoshimura, N., 2016. Advances in intravesical therapy for urinary tract disorders. Expert Opin. Drug Deliv. 13, 71–84.

Ulery, B.D., Nair, L.S., Laurencin, C.T., 2011. Biomedical applications of biodegradable polymers. J. Polym. Sci. B. Polym. Phys. 49, 832–864.

Urbanova, M., Sturcova, A., Brus, J., Benes, H., Skorepova, E., Kratochvil, B., Cejka, J., Sedenkova, I., Kobera, L., Policianova, O., Sturc, A., 2013. Characterizing crystal disorder of trospium chloride: A comprehensive,13C CP/MAS NMR, DSC, FTIR, and XRPD study. J. Pharm. Sci. 102, 1235–1248.

Vaupel, P., Schaible, H.-G., Mutschler, E., 2015. Anatomie, Physiologie, Pathophysiologie des Menschen, 7. Auflage. ed. Wiss. Verlagsges., Stuttgart.

Von Walter, M., 2009. Trospium chloride released from intravesically applied PLGA-based carriers decreases bladder contractility in an isolated whole pig bladder model. Eur. Urol. Suppl. 8.

Wang, B.L., Gao, X., Men, K., Qiu, J., Yang, B., Gou, M.L., Huang, M.J., Huang, N., Qian, Z.Y., Zhao, X., Wei, Y.Q., 2012. Treating acute cystitis with biodegradable micelle-encapsulated quercetin. Int. J. Nanomedicine 7, 2239–2247.

Wang, L.H., Shang, L., Shan, D.Y., Che, X., 2017. Long-term floating control-released intravesical preparation of 5-fluorouracil for the local treatment of bladder cancer. Drug Dev. Ind. Pharm. 43, 1343–1350.

Weaver, J.N., Alspaugh, J.C., Behkam, B., 2010. Toward a minimally invasive bladder pressure monitoring system: Model bladder for in vitro testing, in: 2010 3rd IEEE RAS & EMBS International Conference on Biomedical Robotics and Biomechatronics. pp. 638–643.

Wei, Y., Nedley, M.P., Bhaduri, S.B., Bredzinski, X., Boddu, S.H.S., 2014. Masking the Bitter Taste of Injectable Lidocaine HCl Formulation for Dental Procedures.

Welk, B., Richardson, K., Panicker, J.N., 2021. The cognitive effect of anticholinergics for patients with overactive bladder. Nat. Rev. Urol. 18, 686–700.

Windolf, H., Chamberlain, R., Quodbach, J., 2021. Predicting drug release from 3D printed oral medicines based on the surface area to volume ratio of tablet geometry. Pharmaceutics.

Wong, N.C., Hoogenes, J., Guo, Y., Quantz, M.A., Matsumoto, E.D., 2017. Techniques: Utility of a 3D printed bladder model for teaching minimally invasive urethrovesical anastomosis. Can. Urol. Assoc. J. 11, E321–E322.

Wu, B.M., Borland, S.W., Giordano, R.A., Cima, L.G., Sachs, E.M., Cima, M.J., 1996. Solid free-form fabrication of drug delivery devices. J. Control. Release 40, 77–87.

Wyndaele, J.J., 1998. The normal pattern of perception of bladder filling during cystometry studied in 38 young healthy volunteers. J. Urol. 160, 479–481.

Xiong, G.B., Xie, S.H., Liu, A.B., 2021. In vitro dynamic bladder models for studying urinary tract infections: a narrative review. Ann. Palliat. Med. 10, 4830–4839.

Xu, X., Goyanes, A., Trenfield, S.J., Diaz-Gomez, L., Alvarez-Lorenzo, C., Gaisford, S., Basit, A.W., 2021. Stereolithography (SLA) 3D printing of a bladder device for intravesical drug delivery. Mater. Sci. Eng. C 120, 111773.

Yang, Y., Wang, X., Lin, X., Xie, L., Ivone, R., Shen, J., Yang, G., 2020. A tunable extruded 3D printing platform using thermo-sensitive pastes. Int. J. Pharm. 583, 119360.

Yeong, W.Y., Sudarmadji, N., Yu, H.Y., Chua, C.K., Leong, K.F., Venkatraman, S.S., Boey, Y.C.F., Tan, L.P., 2010. Porous polycaprolactone scaffold for cardiac tissue engineering fabricated by selective laser sintering. Acta Biomater. 6, 2028–2034.

Yeowell, G., Smith, P., Nazir, J., Hakimi, Z., Siddiqui, E., Fatoye, F., 2018. Real-world persistence and adherence to oral antimuscarinics and mirabegron in patients with overactive bladder (OAB): A systematic literature review. BMJ Open 8.

Zacchè, M.M., Srikrishna, S., Cardozo, L., 2015. Novel targeted bladder drug-delivery systems: A review. Res. Reports Urol. 7, 169–178.

Zhang, Y.S., Aleman, J., Arneri, A., Bersini, S., Shin, S.R., Dokmeci, M.R., Khademhosseini, A., Arabia, S., 2016. Bioprinting 3D microfibrous scaffolds for engineering endothelialized myocardium and heart-on-a-chip. Biomaterials 110, 45–59.

Zheng, Z., Lv, J., Yang, W., Pi, X., Lin, W., Lin, Z., Zhang, W., Pang, J., Zeng, Y., Lv, Z., Lao, H., Chen, Y., Yang, F., 2020. Preparation and application of subdivided tablets using 3D printing for precise hospital dispensing. Eur. J. Pharm. Sci. 149, 105293.

Zidan, A., Alayoubi, A., Coburn, J., Asfari, S., Ghammraoui, B., Cruz, C.N., Ashraf, M., 2019. Extrudability

analysis of drug loaded pastes for 3D printing of modified release tablets. Int. J. Pharm. 554, 292–301.

Zinner, N.R., 2006. Trospium chloride: A different anticholinergic. Expert Rev. Obstet. Gynecol. 1, 29–39.

8 Danksagung

Die vorliegende Arbeit entstand unter Begleitung und Unterstützung zahlreicher Menschen, die auf unterschiedlichster Weise zu ihrem Gelingen beigetragen haben und bei denen ich mich bedanken möchte.

Zuallererst möchte ich meinem Doktorvater, Herrn Prof. Dr. Jörg Breitkreutz, für die Aufnahme in seinen Arbeitskreis danken, wodurch diese Promotion erst ermöglicht wurde. Vielen herzlichen Dank für das entgegengebrachte Vertrauen, die vielen Freiheiten bei der Ausführung des Promotionsthemas, die stete Ansprechbarkeit und die langen Diskussionen. Vor allem aber auch für Ihren nie endenden Optimismus, dass die Dinge am Ende gut werden. Besonderen Dank möchte ich auch aussprechen für Ihre Unterstützung dabei, während des Studiums nach Finnland zu gehen, um dort in die Welt des 3D-Drucks einzutauchen. Der Aufenthalt dort war sowohl fachlich als auch privat wegweisend.

Ich danke meinem Mentor, Herrn Prof. Dr. Dr. h.c. Peter Kleinebudde für die anregenden Kommentare und kritischen Rückfragen während diverser Fokusgruppen und Vorträgen, die mich mein Thema oft aus anderem Blickwinkel haben betrachten lassen und nicht selten zu wertvollen Erkenntnissen geführt haben.

Frau Prof. Dr. Anne Seidlitz danke ich herzlich für die spontane Übernahme des Koreferats.

Der INVITE GmbH möchte ich an dieser Stelle für meine Einstellung danken sowie für die vielen Gelegenheiten mit Partnern aus Industrie und Wissenschaft zusammenzukommen und sich auszutauschen. Meinem Vorgesetzten Herrn Dr. Werner Hoheisel gilt besonderer Dank für das offene Ohr bei unterschiedlichsten Fragestellungen und die tolle Betreuung im DDIC.

Herrn Jun.-Prof. Dr. Michael Hacker danke ich herzlich für die vielen anregenden Gespräche rund um das Thema Rheologie, die meinen Horizont in vielerlei Hinsicht erweitern konnten.

Herrn Dr. Julian Quodbach danke ich für die stete Diskussionsbereitschaft rund um das Thema Druckbarkeit und das tolle Review-Paper, welches gemeinsam entstanden ist. Ebenso danke ich Dr. Björn Fischer für die Raman-Messungen, die langersehnte Erklärungen geliefert haben sowie für die wertvollen fachlichen Diskussionen. Bei Herrn Dr. Raphael Wiedey möchte ich mich bedanken für die tolle Zusammenarbeit bei der Programmierung des Blasenmodells, ohne dessen Hilfe die Automatisierung des Modells undenkbar gewesen wäre und dessen fachlichen Rat ich sehr zu schätzen weiß.

An dieser Stelle bedanke ich mich sehr herzlich bei Herrn Stefan Stich, der durch seinen unermüdlichen Einsatz bei der Anfertigung des Blasenmodells eine tragende Rolle gespielt hat. Ohne die vielen Ideen, Ausflüge zu diversen Glasbläsern und in die Feinmechanik sowie Rettungsaktionen undichter Blasen, wäre ich wahrscheinlich an mehreren Stellen schon längst verzweifelt.

Vielen Dank auch an Herrn Dr. Sebastian Bollmann, der durch seine Expertise in der Welt des µCTs inklusive der Bildbearbeitung und -analyse zu wesentlichen Ergebnissen dieser Arbeit beigetragen hat und der für mich so Einiges aus seiner Welt in meine Sprache übersetzen konnte.

Des Weiteren danke ich meinen WPP-Studentinnen Sevda Demircan und Lena Franken für ihren motivierten und engagierten Einsatz, bei welchem sehr interessante Ergebnisse entstanden sind.

Frau Andrea Michel und Dorothee Eikeler danke ich für die vielen, vielen DSC-Messungen (mit wunderschönem Zettel!) und Bildbearbeitungen, die unerlässlich waren und wichtiger Bestandteil dieser Arbeit sind. Die Qualen waren nicht umsonst!

Unvergessen bleibt die Zeit der Promotion vor allem auch durch die vielen Menschen, die diese intensive Zeit nebst ihren fachlichen Kompetenzen geprägt haben.

Bei meinen lieben Bürokollegen Dr. Isabell Keser, Dr. Annika Wilms, Anja Göbel, Dr. Ard Lura und Hellen Mazur bedanke ich mich sehr herzlich für die unzähligen lustigen Momente, Käffchen, (fast) sterbenden Büropflanzen, real-talks und den steten Zuspruch, ohne welche die Promotion längst nicht so gut zu schaffen gewesen wäre.

Dr. Ard Lura danke ich herzlich für die mannigfaltigen Weisheiten (manche von Coach Boone, manche von der Straße), die einen geerdet haben, wenn es nötig war. #linke Seite

Dr. Ilias El Aita danke ich für die wertvolle Freundschaft, die in unserer kurzen gemeinsamen Zeit am Institut entstand.

Vielen Dank an Laura Falkenstein, dafür, dass Du in allen Lebenslagen für ein Käffchen zu haben bist und man immer auf Dich zählen kann. Unsere Freundschaft möchte ich nicht mehr missen #neue Ära!

Wenn von Käffchen die Rede ist, darf Marcel Kokott nicht unerwähnt bleiben. Den besten Kaffee (mit bester Unterhaltung) gab es stets im Büro Kokott/Klinken/Elezaj abzustauben. Ein wahrer Schlingelino weiß einfach, wie’s geht! Ebenso danke ich Rebecca Chamberlain und Hellen Mazur für die Freundschaft, die nach dem Studium noch gewachsen ist und die die Promotion so manches Mal erleichtert hat.

Christoph Nüboldt danke ich für seine ehrliche und positive Art, die ich seit Beginn der Promotion erleben konnte. Den Endspurt beim Schreiben der Dissertation hat es so viel erträglicher gemacht, dass wir zusammen gelitten und uns motiviert haben!

Dr. Annika Wilms danke ich für die vielen erheiternden Gespräche und Friends-Zitate, die nie ungewürdigt blieben. Unsere 20 Arten Kaffee zuzubereiten (vorausgesetzt die richtigen Pads waren vorhanden) halte ich in guter Erinnerung.

Auch bei Dr. Dina Maria Kottke, Bastian Hahn (der Pokal war sabotiert!), Dr. Vincent Lenhart (high-five!), Dres. Olga und Philipp Kiefer, Jerome Hansen und den anderen nicht namentlich genannten Institutsmitgliedern bedanke ich mich herzlich für die vielen schönen Momente in und außerhalb des Instituts!

Vielen Dank auch an meine lieben Freundinnen Laura Amato, Ariane Sojka und Caroline Herde, deren unerschütterliche Freundschaft ich schon seit mehr als zwei Jahrzehnten schätze und die nicht mehr wegzudenken sind.

Mein größter Dank gebührt meiner Familie.

Danke an meine Großeltern Walter Slachmuylders und Christiane Bleumers für die liebevolle Unterstützung während Studium und Promotion.

Vielen lieben Dank an meine beiden Brüder Rueben und Naim Rahman für die stete Versorgung mit allerlei Snacks (am besten zu guten Serien) und die Sicherheit in allen Lebenslagen ihren Rückhalt zu haben. Rueben Rahman gebührt auch außerordentlicher Dank für die Übersetzung meiner Kritzeleien und Gedanken in astreine CAD-Dateien, wenn ich an meine zeichnerischen Grenzen stieß.

Für die Dankbarkeit, welche ich für meine Eltern Saeedur und Chantal Zainab Rahman empfinde, gibt es nicht genug Worte. Ohne Eure grenzenlose Liebe und Fürsorge wäre das alles nicht denkbar gewesen.

Last but not least, möchte ich mich bei meinem Ehemann Dr. Emrah Yildir bedanken. Danke für Deinen liebevollen Rückhalt und die 1000e Kilometer, die Du viel zu oft zurückgelegt hast, um bei mir zu sein und mich auf dieser Reise mit Deiner geduldigen, wundervollen und lustigen Art zu unterstützen. You turned a lot of frowns upside down! Seni çok seviyorum.

9 Eidesstattliche Erklärung

Hiermit versichere ich an Eides Statt, dass die Dissertation von mir selbstständig und ohne unzulässige fremde Hilfe unter Beachtung der „Grundsätze zur Sicherung guter wissenschaftlicher Praxis an der Heinrich-Heine-Universität Düsseldorf“ erstellt worden ist und dass ich diese in der vorgelegten oder in ähnlicher Form noch bei keiner anderen Fakultät eingereicht habe.

_____

Jhinuk Rahman-Yildir